88@ Università degli Studi di Firenze – Faculty of Engineering
Via di Santa Marta, 3, 50139 Firenze, Italy.

ISBN XXX–XX–$XXXX$–XXX–X
D/$XXXX$/$XXXX$/XX

”Deep down you may still be that same great kid
you used to be.
But it’s not who you are underneath,
it’s what you do that defines you.”
Rachel Dawes

Abstract

The objective of the present thesis, which lies within a national research project, is the analysis of a "*cold bridge*" leading edge cooling system for a high pressure gas turbine blade, with the aim to study the combined effects of jet impingement and mass flow extraction on heat transfer phenomena. Both experimental and numerical investigations have been carried out, with the main aim to assess the effects of rotation on the heat transfer distribution in a realistic leading edge internal cooling system. The model is composed of a trapezoidal feeding channel which provides air to the cold bridge system by means of three large racetrack-shaped holes. Such holes generate coolant impingement on the internal concave leading edge surface, whereas four big fins assure the jets confinement. Air is then extracted through 4 rows of 6 holes reproducing the external cooling system composed of shower-head and film cooling holes. The effect of the pressure drop between pressure and suction side is reproduced by three plenum that allow variable coolant mass flow rate extraction from each cooling row, providing realistic flow conditions inside the leading edge cavity.

Experiments were performed in static and rotating conditions replicating the typical realistic range of jet Reynolds number (Re_j) from 10000 to 40000 and Rotation number (Ro_j) up to 0.05, for three cross-flow cases representative of the working condition that can be found at blade tip, midspan and hub, respectively (CR of 10%, 40% and 70%). The heat transfer coefficient distribution on the LE internal surface have been assessed by means of a rotating rig developed at University University of Florence, exploiting wide band Thermocromic Liquid Crystals (TLC) with a steady-state technique. An analogous rotating rig, developed at University of Udine which collaborates within the same national research project, has been exploited to analyze the internal flow field by means of Particle Image Velocimetry (PIV) technique.

First of all, an experimental campaign in stationary conditions has been performed, assessing the impact on the HTC distribution on the LE of several characteristic parameters: Re_j, CR and the pressure drop between pressure and suction side of FC. Results show a significant dependency of Nusselt number value on Reynolds jet number which does not appreciably affect its distribution on the LE. On the contrary a mild relation has been found with respect to cross-flow conditions, which does not remarkably affect the averaged Nu value but sensibly impact on its pattern. The dependency on extraction conditions has also been found to be weak. Concerning rotating conditions, the aero–thermal field turned out to be rather complex, but a good agreement between heat transfer coefficient and flow field measurement has been found. In particular, jet bending due to rotation strongly depends on cross-flow intensity, while *Ro* has a weak effect on both jet velocity core and area-averaged Nusselt number. Rotational effects increase for the lower cross-flow tests, while are almost negligible in hub condition. Heat transfer pattern shape has been found to be substantially Reynolds-independent.

A parallel computational analysis of the rig has also been performed, aimed at identifying a suitable numerical model to investigate such phenomenon in order to deepen its physical comprehension. Stationary tests with uniform extraction conditions have been simulated on a symmetric model by means of a RANS approach, using a k-ω SST turbulence model. Then, a benchmark of two hybrid RANS-LES models such as Scale Adaptive Simulation (SAS) and Detached Eddy Simulation (DES), has been performed on a stationary test with non uniform extraction conditions. RANS, but also SAS and DDES approaches, present a slightly underestimation of heat transfer experimental values, but the heat exchange distribution shape is accurately reproduced by the models. The most suitable numerical model at resolving the complex flow field associated with jet impingement is the DDES, thus, it has been exploited for the numerical investigation in rotating conditions. A fairly good agreement with experimental measurements is observed, which represent a further validation of the adopted computational model. As a consequence, the computed aerodynamic and thermal fields also allow an in-depth interpretation of the experimental results.

Contents

List of Figures

List of Tables

Nomenclature

Letters

a	thermal diffusivity
c	specific heat
D	diameter
h	convective heat exchange coefficient
k	turbulent kinetic energy
K	relative Nusselt difference
m	mass
M	Mach number
n	rotational speed
p	pressure
P	radial impingement pitch
q	heat flux
Q	heat
R	specific gas constant
S	radial spacing
T	temperature
$\vec{U}$	velocity vector
v	velocity
w	specific work
W	work
x	circumferential coordinate
y	radial coordinate

Greeks

β	compression ratio
γ	specific heat ratio
ϵ	turbulent kinetic energy dissipation
ζ	bulk viscosity
η	efficiency
λ	thermal conductivity
μ	dynamic viscosity
ρ	density
τ	ratio between extreme temperatures
ϕ	generic scalar quantity
Φ	viscous dissipation
ω	turbulent kinetic energy specific dissipation
Ω	rotation speed

Acronyms

Cr	crossflow
CFD	computational fluid dynamics
DES	detached eddy simulation
$DDES$	delayed detached eddy simulation
DNS	direct numerical simulation
EXP	experimental
FC	film cooling
GIS	grid induced separation
GT	gas turbine
HTC	heat transfer coefficient
LC	liquid crystal
LE	leading edge
LES	large eddy simulation
PS	pressure side
$RANS$	Reynolds averaged Navier Stokes

RHR	rotating heat transfer rig
SAS	scale adaptive simulation
SF	scale factor
SH	showerhead
SHR	static heat transfer rig
SRS	scale resolving simulations
SS	suction side
TIT	turbine inlet temperature
TLC	thermochromic liquid crystals

Subscripts

b	body
$down$	downstream
e, w, n, s	east, west, north, south cell face
E, W, N, S	east, west, north, south cell neighbor
EXP	experimental
h	hydraulic
j	jet
LE	leading edge
m	mean
max	maximum
mod	modeled
nb	neighbor
P	nodal point
r	real
res	resolved
s	surface
up	upstream
v	constant volume
w	wall
x	spanwise/circumferential direction
y	streamwise/radial direction

Introduction

In front of the ever increasing gas turbine performances demand, both in terms of specific power output and thermal efficiency, the turbine inlet temperature (TIT) represents a very key parameter to meet such needed. The TIT increasing has become one of the main target of engine development during the last decades and, thanks to highly effective cooling system, it has reached values far beyond the melting point of gas turbine components. Such levels have been achieved through both the development of materials capable to withstand high thermal stresses, and the introduction of internal and external cooling systems, needed to preserve the most critical components, such as combustor and turbine first stages. The efforts made to develop such technologies are justified by a significant performance increase due to the TIT enhancement, as depicted in figure 1 (and expected by the theoretical formulation of power, see [10]), represented as the full line called "Ideal performance" in the above cited figure.

Specific manufacturing techniques, like directionally-solidification and single-crystal castings, were developed appositely for increasing gas turbines parts' life and nowadays many airfoils use single crystal super-alloys guaranteeing satisfying thermo-physical properties [16, 17, 18, 19, 20]. Despite all the efforts performed by material's designers, it would not be possible to reach TIT values of 1800-1900 K without the presence of an adequate cooling system. In figure 2 it can be appreciated how the contemporary development of new materials and cooling techniques had allowed to reach TIT values higher than metal melting temperature.

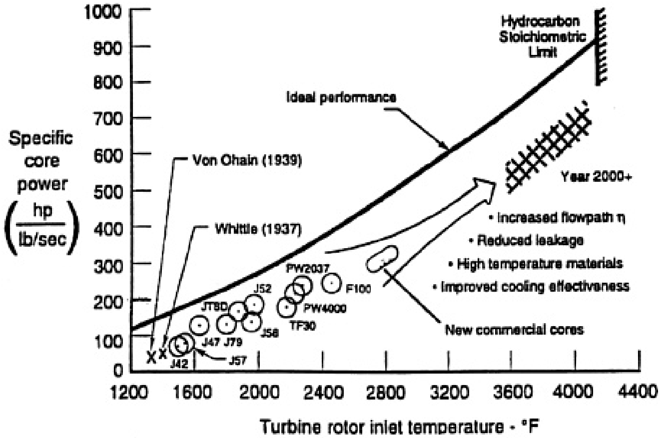

Figure 1: Power increase enabled by TIT increase [1].

Since cooling systems use air bled from the compressor, it has a cost on the performance of thermodynamic cycle: a progressive reduction of the global efficiency inevitably occurs increasing the amount of coolant. Gas turbine designers have the goal to maximize cooling system effectiveness, or in other terms to ensure required component lifespan using a minimal amount of coolant flow. However, the optimization of such systems is a particularly challenging task, given the strong constraints in terms of size and the many thermal and fluid dynamic phenomena which drive the performances of a particular system; moreover, the interaction between the various applied techniques also needs to be taken into account. Another fundamental aspect to be considered is that a significant part of the components needing cooling are the rotating ones, such as the first stages blades: this aspect implies not only a greater complexity in the cooling system, but also an additional influence on the heat removal performances, given by the arising fictitious forces.

The whole of these aspects implies that cooling system development needs to be supported by complete and detailed studies, which at the present day can only be achieved through the combination of direct

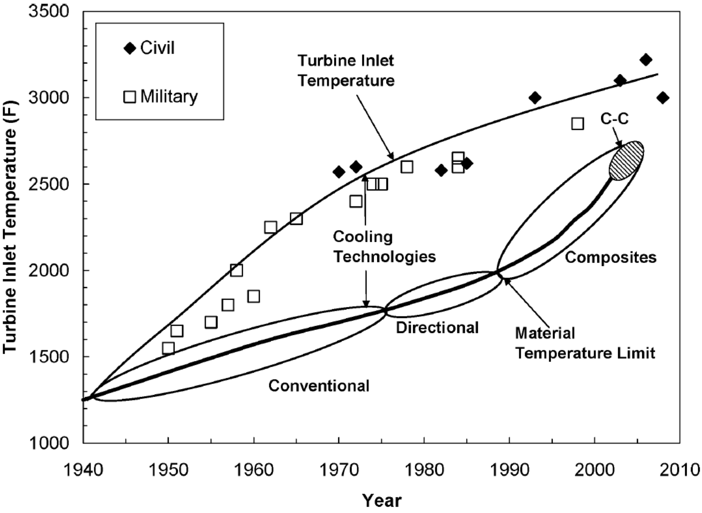

Figure 2: Comparison between TIT and blade material temperature limits highlighting the importance of cooling technology, [2].

measurement and computational analysis. The present research work falls within such context. The study is performed within the research program of national interest named *PRIN* 2010-2011 INSIDE project (*Programma di Ricerca di Interesse Nazionale*, 2010-2011 aerothermal INvestigation of cooled Stage turbIne: Design optimization and Experimental analysis). The main aim of such project is the investigation of the effects of rotations (in addition to several other characteristic fluid dynamic parameters) on the turbine blades internal cooling systems performances. In particular, the present activity focuses on the airfoil leading edge: this region is indeed one of the most critical in terms of cooling, given both its unfavorable geometry and the high thermal and mechanical stresses to which it is subject.

Literary overview

A great amount of studies have been dedicated to the impingement cooling technique, given its outstanding cooling potential and the complexity of involved thermal and fluid dynamic phenomena. The first significant ones on such matter were performed by Metzger et al. [21], Kercher and Tabakoff [22], Martin [23], Goldstein et al. [24] and Florschuetz et al. [25] [26], which studied impingement on a flat surface and highlighted the strong sensitivity of cooling performances to jet Reynolds number and jet-to-target plate spacing.

The research on flat plate impingement cooling was later enriched by the study of the effects of coolant extraction: Hollworth and Dagan [27] and more recently Ekkad et al. [28] reported a decrease in heat exchange performances in case of cooling flow removal, counterbalanced by a more uniform heat exchange distribution and by an attenuation of crossflow effects.

Considering the object of the present work, the studies involving impingement on concave surfaces are way more interesting, as such shape presents better similarity with a blade leading edge internal surface. Studies on this subject were performed by Chupp et al. [29], Metzger et al. [30] [31] and Hrycak [32]. In these papers, the effects of the target surface shape on heat transfer coefficient are investigated: in particular, Metzger et al. [31] suggested that for sharper surfaces the jet could impinge first on the side walls of the cavity, thus generating a heat transfer pattern significantly different from the one obtained for a flat surface.

Very interesting contributions were provided in more recent years by Metzger and Bunker [33] [34]: their work was expressly focused on the impingement cooling of turbine blade leading edge region, with or without cooling flow extraction. These authors performed detailed heat transfer measurements using temperature sensitive coatings and digital image acquisition, combining the variations of many parameters. They found that heat transfer appears to be mainly driven by the jet Reynolds number, with a weaker influence by the distribution of extracted flow. They also found an increase in heat transfer with coplanar jet holes and extraction holes arrangement, while staggered configurations led to a decrease in heat transfer.

The experimental approach to the impingement problem, represented by the aforementioned investigations, was followed by analytical and numerical researches on the same subject. A numerical study of impingement heat exchange was attempted using two-equation turbulence models by Polat et al. [35], Frost and Jambunathan [36] and Coussirat et al. [37], while Morris et al. [38] and Souris et al. [39] also used Reynolds stress models: as a general consideration derived from such studies, it can be stated that the accuracy of the numerical setup is strongly dependent on the geometry and fluid dynamic condition of the particular test case. However, a review performed by Zuckerman and Lior [8] showed that k-ω SST and v^2-f models embody the best compromise between accuracy and computational cost for the simulation of a jet impingement problem.

Considering the object of the present work, a study of Kumar and Prasad [40] is particularly significant: in such work, the authors performed a computational investigation on a row of circular jets impinging on a concave surface, thus modeling the case experimentally investigated by Metzger and Bunker [33]. Results showed k-ω SST to be a better predictive turbulence model for impingement studies on concave surfaces, with good agreement with the trend of experimental data and only a slight under prediction in values. The effect of coolant extraction was added by Kumar and Prasad in a more recent study [41] on a different impingement geometry. This numerical investigation indicated that heat transfer is greatly enhanced in staggered impingement and extraction holes arrangement, while a minor influence is attributed to the different exit configurations.

In more recent years, greatly significant results have been obtained by Taslim et al. [42] [43] [44] [45]. The authors performed experimental analyses of some complex leading edge cooling systems, involving impingement on concave surface, various kinds of turbulence promoters, coolant extraction from shower head and film cooling holes and different crossflow configurations. The most interesting findings of such works were that heat transfer rate is strongly enhanced by the presence of extraction holes and of turbulence promoters, even if in the latter case the increase in cooling performance is mainly due to the greater wetted area; moreover, it was found crossflow to have a strong influence on the mass flow distribution, even if its effect on the heat exchange are uncertain. Some of these studies also compare the experimental results with a CFD analysis, and demonstrate that the latter is a viable tool for the study of such phenomena. Two recent studies by Maiuolo et al. [46] [47] consisted in an experimental survey of a state of the art leading edge cooling scheme, involving film cooling and shower head coolant extraction and various leading edge cavity and impingement plate geometries. An interesting result of these investigations is that, for a single central row of circular impingement holes, a sharper leading edge wedge angle results in higher heat transfer rates along the side walls, as an effect of reduced jet-to-target surface distance and jet spreading. Furthermore, it was shown that shower head coolant extraction guarantees higher heat exchange in the curved central surface and a slight decrease on lateral surface, resulting in a negligible influence on averaged values.

All the aforementioned studies focused on impingement cooling in a static frame of reference, thus their results find a direct application in gas turbine vane cooling. However, such cooling technique is also greatly suitable for the blade leading edge, where intense rotational forces strongly influence jet flow behavior. The first significant studies on leading edge cooling with rotation were performed by Epstein et al, [48] and by Mattern and Hennecke [49], which investigated the effects of different Rotation numbers and stagger angles (i.e. angle between jet and rotation directions): both studies revealed a decrease in heat exchange with an increase in rotation speed and a noticeable influence of stagger angle. An experimental and numerical investigation of a row of jets impinging on a concave surface under static and rotating conditions was performed by Iacovides et al. [50] [51] [52]. Their results showed that rotation reduced heat transfer and increased the spreading rate of the jets. Hong et al. [53] [54] [55] investigated the effect of surface geometry (flat and concave), jet direction in respect of rotation axis, and rib turbulators on heat/mass transfer in rotating impingement/effusion cooling. They found that concave target surface enhanced heat exchange both in static and rotating conditions, and that the presence of the ribs increased the local heat transfer effect by reducing the rotation-induced crossflow. More recently, Zhu et al. [13] performed an experimental investigation of jet impingement applied to a simplified leading edge geometry, inquiring the effects of various Rotation numbers, Reynolds numbers and stagger angles. Their results confirmed the heat transfer reduction due to rotation, with a larger decrease on the pressure surface with respect to the suction surface. On the other hand, an experimental and numerical study performed by Jung et al. [14] on a rotating leading edge impingement cooling system demonstrated that rotation can enhance heat transfer, but only if jet-to-target surface distances are small and if crossflow and Coriolis force induce opposite jet deflections.

Finally, other experimental studies performed by Maiuolo et al. [56, 57] and Rolls-Royce UK [58] within the European Research Project named ERICKA (Engine Representative Internal Cooling and Knowledge Applications) are here mentioned, since the geometry investigated in the framework of PRIN 2010/2011 INSIDE project have been derived from the comparable ones already tested there. Maiuolo et al. performed an extensive experimental campaign, supported by CFD simulations, aimed to the assessment of heat transfer performances of a *cold bridge* impingement cooling system in static conditions. The main object was to investigate the effects of some fluid dynamic parameters, such as jet Reynolds number and cross-flow split, on the cooling system effectiveness involving a wide range of flow conditions and coolant extraction configurations. The studied geometry was a slightly modified geometry of a realistic leading edge internal cooling system of a high pressure gas turbine blade, named AVIO C3, scaled up with a scale factor (SF) of 43:1. The study reveals that the heat transfer coefficient distribution is slightly affected by the cross-flow, but a lower cross-flow lead to an enhancement of Nusselt number peak on the flat surfaces. At the same time Nu is strongly affected by the jet

Reynolds number as heat transfer remarkably increase with Re_j even if it does not affect the HTC pattern on the LE. Rolls-Royce UK performed instead the investigation of the effect of rotation on cooling performances on the same leading edge geometry. The main impingement cooling system features are identical to the above mentioned static campaign, but with a smaller scale factor ($SF = 4.3$). This allows to position the model on a rotating rig but also involves a lower level of details captured by the measurements. Such tests, performed in rotating conditions, confirmed the strong dependency upon the Re_j value, but also showed a mild relation between heat exchange and rotation conditions for this geometry. In particular, a higher rotational speed seems to lightly reduce local Nusselt (Nu) values on the pressure side, while increasing them on the suction side. With respect to the radial outer direction, rotation also appear to shift heat exchange peaks outwards for the pressure side and inwards for the suction side. All of these evidences lead to the supposition that rotation causes the impingement jet to bend towards the suction side: this fact has been attributed to an uneven pressure distribution in the feeding channel, and has been confirmed by other secondary effects, all induced by the Coriolis force action. Despite this, the high dispersion of experimental data reduces the confidence of these assumptions, and evidences the need of further investigation about the effects of rotation.

Research objectives

The present work fits in the research branch presented above. Its object is the experimental and numerical investigation of a cold bridge impingement cooling system, with the aim to assess the effects of rotational velocity on the heat transfer distribution, as well as its dependency from several characteristic parameters. As already mentioned, the investigated geometry has been derived from a realistic leading edge internal cooling system of a high pressure gas turbine blade, named AVIO C3, studied within the ERICKA European Research Project. Such geometry has been analyzed through an extensive experimental campaign: flow-field was investigated through Particle Image Velocimetry (PIV) measurements at the Department of Electrical, Management and Mechanical Engineering of the University of Udine; meanwhile, the distribution of heat transfer coefficient on the leading edge internal surface was evaluated by means of Thermochromic Liquid Crystal (TLC) measurements at the Industrial Engineering Department of the University of Florence. The tests have been performed with different rotational velocity, jet Reynolds numbers (Re_j) and crossflow settings, in order to suitably reproduce engine representative conditions, as well as to assess the impact of different flow parameters. In particular, the speed of rotation has been varied to match Rotation number from 0 up to 0.05, moreover, four Re_j values have been investigated, ranging from 10 000 to 40 000, and crossflow has been set to reproduce the cooling system conditions along the whole blade radial span. Uniform and non uniform mass flow extraction conditions have also been imposed, to evaluate and quantify the effects of pressure side and suction side external pressure gradients on the internal cooling system.

The experimental survey has been supported by an appropriate numerical analysis on the same test model, with the aim to deepen the knowledge of the involved phenomena as well as to determine the most suitable numerical configuration for this kind of flows. Uniform extraction tests in static conditions have been simulated through a RANS approach on a symmetric fluid domain, replicating a complete variation range of both Re_j and crossflow conditions. Then, a benchmark of two hybrid RANS-LES models such as Scale Adaptive Simulation (SAS) and Detached Eddy Simulation (DES), has been performed on a stationary test with non uniform extraction conditions. Then, the most suitable numerical model at resolving the complex flow field associated with jet impingement, the DDES approach, has been exploited for the numerical investigation in rotating conditions. Despite that, an analogous geometry has already been investigated in the framework of the ERICKA European Research Project, such investigation represent a fundamental step towards a better comprehension of the physical phenomena involved in the impingement cooling system and to the assessment of rotational effects on its thermal efficiency. Indeed, a higher scaling factor has been chosen for the model geometry (SF 30.1:1) during such work, allowing for a more and more detailed investigation of both flow field and heat transfer coefficient distribution in rotating conditions. Moreover, as performed in this work, such experimental measurements represent a very detailed database against which compare the results of computational analysis in order to assess the most suitable model for such kind of investigations. Indeed, the CFD analysis of this phenomena, especially in rotating conditions, represent a very challenging matter.

Thesis outline

The present thesis is structured as follows.

Chapter 1 presents an extensive survey on the theoretical aspects involved in gas turbine cooling techniques. Main features of cooling systems are presented, focusing on *impingement cooling* both in static and rotating conditions.

Chapter 2 reports the detailed description of experimental survey. An overview of the test rig, the model and the measurement apparatus is presented; given its importance for the present work, TLC thermography is also briefly introduced.

Chapter 3 focuses on the CFD computations, with a detailed introduction to numerical methods and turbulence modeling, focusing on hybrid RANS-LES models.

Chapter 4 presents both experimental and numerical outcomes achieved in stationary conditions. First of all, experimental results are discussed, describing the effects of jet Reynolds number, crossflow conditions and differentiated mass flow extraction. Then, numerical results obtained in uniform extraction conditions (with a RANS approach) are presented, showing a satisfactory agreement with experimental results. Finally the results of benchmark of two hybrid RANS-LES models are reported for non uniform extraction results.

Chapter 5 reports both experimental and numerical results obtained in rotating conditions. Firstly, experimental measurements are reported, followed by computational results. The satisfactory agreement between the two outcomes allows to further validate the numerical model and to exploit it to deepen the physical comprehension of the phenomena which affect the impingement cooling system behavior in rotating conditions.

Chapter 1

Gas turbine cooling

The present work deals with one of the most important topic concerning gas turbine development: the airfoil cooling system design. Despite the constant development concerning materials, as the TIT exceeds the values allowed by material's resistance, internal and external cooling systems are needed to preserve the most thermally stressed components. For such components, like the first stages blades and vanes which are exposed to the hot main gas, it is essential do not exceed the wall temperature limits since that is detrimental to their life time. Since the cooling system bled the air from the compressor, gas turbine designer have the goal to minimize the amount of coolant flow consumed, maximizing the cooling system effectiveness. Indeed, such working fluid extraction leads to a proportional reduction of the thermodynamic cycle performances, because of the work done to compress the air and the addition of coolant back into the hot gas stream which imposes further thermodynamic penalties. Before starting to describe the geometry of the internal cooling system investigated during the present work and to go into the details of this research project, it is necessary to give a brief overview about the state-of-the-art of internal and external gas turbines cooling systems. The basics of the airfoil cooling systems are introduced into this chapter, focusing on the effect of rotation on internal cooling systems and, in particular, on impingement cooling; finally, section 1.9 is concentrated on the effects of rotation on the leading edge cooling systems. Cooling system are usually classified in *internal* or *external* cooling depending on the side of the blade wall on which the cooling is performed. The former are refrigeration methods in which the removal of heat occurs inside the thermally loaded component. The latter allow coolant from inside the blade to eject out onto the hot-gas side surface aimed to the protection of the blade, like film cooling.

During the past years several cooling systems have been developed in order to increase their effectiveness, reducing the over mentioned engine performances decrease due to the bleed of working flow from the compressor. Gas turbine blades and vanes are cooled by means of a combination of such internal convection cooling, like impingement, turbulated multi-pass serpentine passages, flow through pin-fin arrays or simply smooth or turbulated radial channels. In such section the most common techniques are briefly reported.

1.1 Radial and multi-pass ducts

Among the several internal cooling system, radial ducts represent the main basic one, which, in its simplest form, consist of a series (single-pass or multi-pass) of straight smooth channels. The coolant flow, aimed to the heat removal, usually enters from the hub of the blade and it passes through such internal channels in radial direction; spent coolant is afterward normally discharged from the blade tip. Despite internal smooth ducts design and manufacture result pretty, they present poor cooling effectiveness; thus, an excessive air extraction is required to ensure an adequate heat exchange. In order to enhance the HTC, both total surface cooled by the flow and turbulence value can be increased; as shown in figure 1.1, going from a single pass to a multi-pass configuration, where total surface is widely increased, represent an effective way to increase the heat removal. To further increase HTC and the efficiency of such internal channel, several kind of "turbulence promoters" are exploited to increase

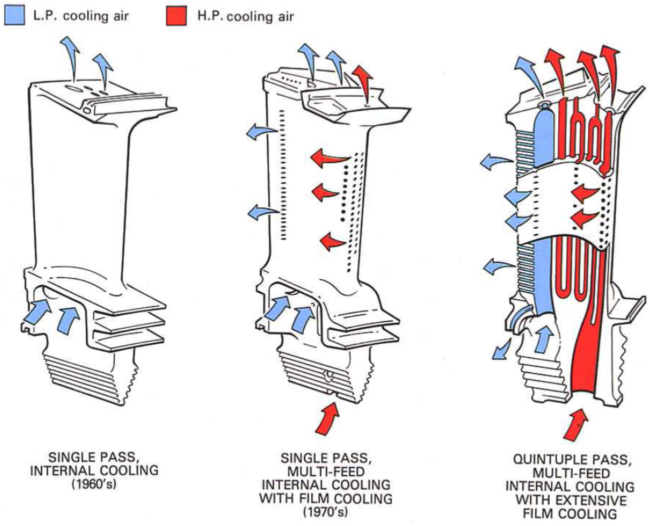

Figure 1.1: Radial single and multi-pass cooling channels, [3].

the turbulence level of the air passing through the ducts, like rectangular *ribs*, *pin fins* and *dimples*.

1.2 Rib turbulated cooling

Ribs are rectangular obstacles located into the radial internal channels, aimed to generate turbulence, enhancing the cooling effect. Indeed, internal smooth ducts present poor cooling effectiveness, because of the development of thick dynamic and thermal boundary layers. The role of such turbulence promoters is to simply trip and interrupt the boundary layer. As shown in figure 1.2, where a conceptual view of the effects of ribs on the mainstream flow is presented, after boundary layer is disturbed, redevelopment begins, and HTC increases because of the thinner boundary layer. The separation that occurs as the coolant passes over the rib, results in a lower HTC region downstream the rib, due to a relatively hot cell

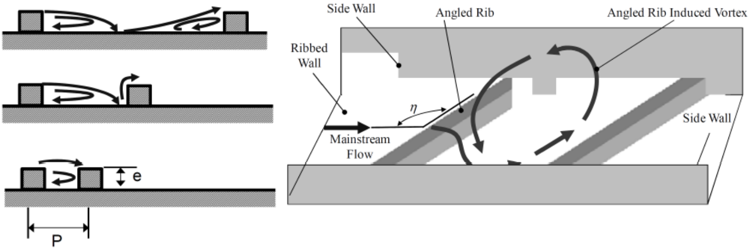

Figure 1.2: Rib effects on mainstream and secondary flows, [4].

being trapped into the recirculating area. Nevertheless, a higher heat transfer region takes place when the mainstream flow reattaches between two ribs, due to the air impingement on such surface.

This pattern of separation, recirculation, and reattachment continues throughout the channel along with the pattern of repeating ribs [4]. Unfortunately, not only the heat transfer increase due to the ribbed configuration of the channel, but also pressure losses enhance along it. Several geometrical and fluid-dynamic parameters affect both the heat transfer and the pressure losses enhancement and many correlations are available in literature for radial ducts, both in smooth and turbulated configurations. For more details, please refer to [10, 59].

1.3 Pin fins

An additional kind of turbulence promoters are pin fins, which consist of cylindrical or prismatic obstacles connecting two opposite channel walls, with their axes orthogonal to the coolant direction. Their main aim is to enhance HTC increasing the flow turbulence level thanks to the upstream horseshoe vortex and to the downstream wake shedding, which increase turbulence and mixing. Moreover, pins conduct thermal energy away from the heat transfer surface, and long pins can increase the effective heat transfer area and consequently the heat removal. Pin fins are widely adopted in gas turbine trailing edge cooling, as they allow a strengthening of the blade structure and to increase the heat exchange without thickening the airfoil blade.

A schematic view of a typical trailing edge pin-fin array is shown in figure 1.3. In the same way as rib, several parameters affect heat transfer performances of a pin fin array, like pin spacing (in both streamwise and spanwise direction), size and shape; thus, a lot of correlations are available in literature, [60, 61, 62]. For more details, please refer to [10, 63].

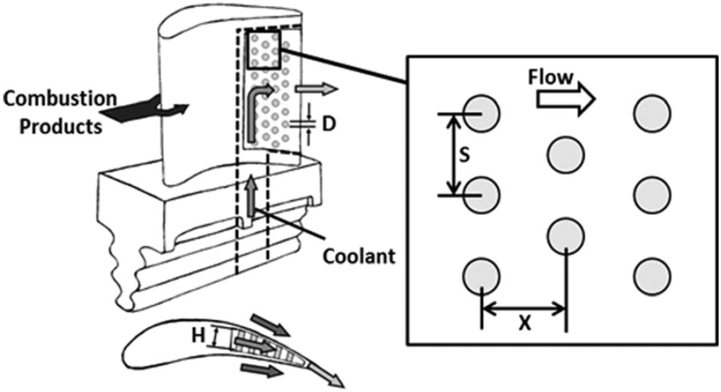

Figure 1.3: Schematic of a pin-fin array at the trailing edge of a gas turbine airfoil, [5].

1.4 Dimple cooling

Finally, dimples are another kind of turbulence promoters, which are arrays of indentations along internal channel, usually spherical in shape. As shown in figure 1.4, arrays of dimples improve the internal cooling by producing multiple vortex pairs which enhance the local HTC as they advect downstream. Since they do not protrude into the channel, the use of dimples do not produce significant amounts of form drag; this

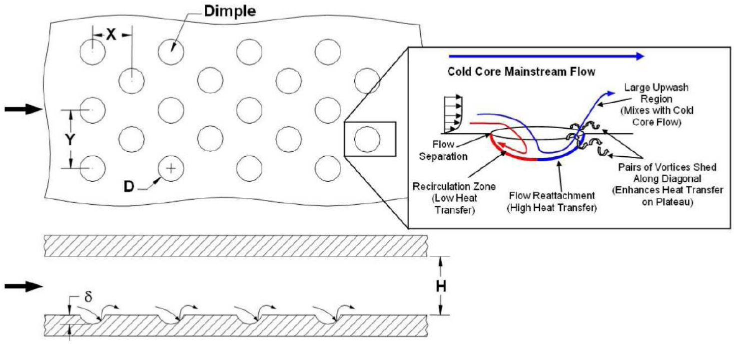

Figure 1.4: A typical test model for dimple cooling studies with a conceptual view of dimple induced secondary flow, [6].

is a valuable advantage since they produce lower pressure losses during their passage through an internal airfoil cooling duct respect to ribs and pin fins [10]. Thanks to this benefit, dimples are frequently applied for cooling later turbine stages, where lower pressure cooling air is employed, or in channel where a favorable pressure margins has to be maintained downstream the obstacles array[64, 65].

1.5 Impingement

Jet impingement are largely adopted in modern gas turbine internal cooling applications. Such systems exploit the impact of several coolant jets against the heat transfer target surface. These *impingements* lead both to enhance the flow turbulence level and to achieve a very thin thermal boundary layer in the surroundings of jet stagnation point; such phenomena allow to remarkably improve heat exchange. Usually the internal cooling air is guided by means of an impingement plate where, thanks to an array of driving holes, a series of high velocity jets are ejected towards the target surface.

Thanks to the direct impingement of the coolant on the interested internal surface, such cooling system ensures a local HTC augmentation that is higher than that offered by all the other cooling techniques described above. Thus, impingement cooling is largely used as gas turbine internal cooling technology, especially where high heat exchange requirements demand the application of a particularly effective cooling system. Despite these considerable advantages, its application is limited by the fact that the manufacturing of an impingement cooling system implies the realization of two cavities inside the blade, divided by a perforated wall. Such solution gives birth to problems in terms of both manufacturing and structural strength; as a consequence, impingement is mainly used to cool vanes, because of the absence of centrifugal loads. In this case, the system is realized by means of perforated liners inserted into the vane cavities, and can be applied both in the leading edge and in the midchord regions. On the contrary, rotating blades require material cross sections incompatible with the kind of system described above. In this latter case, impingement cooling is only applied to the most thermally loaded regions, such as the leading edge, and with different configurations. A typical setup used in rotating blades is called *cold bridge* and consists of radial impingement at the leading edge cavity. This configuration is usually applied along with shower head systems and occasionally with film cooling. Jets are generally arranged in regular arrays, to provide relatively uniform and controlled cooling on extended internal surfaces.

Since the aim of the present work is the detailed analysis of an impingement cooling system, an in-depth discussion of the fluid-dynamic phenomena involved by such cooling scheme is reported. A schematic view of a typical surface impingement caused by a single jet is represented in figure 1.5.

Flow conditions of impinging jets, are mainly characterized by the jet Reynolds number, defined as:

$$Re_j = \frac{\rho v_j D_j}{\mu} \tag{1.1}$$

where ρ is the fluid density, v_j is the initial average jet velocity, D_j is the nozzle or orifice hydraulic diameter and μ is the fluid dynamic viscosity.

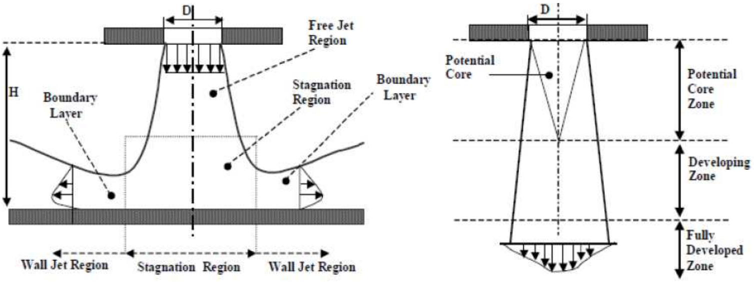

Figure 1.5: Schematic representation of flow field generated by a jet impinging on a solid surface [7].

Depending on the jet Reynolds number, four different jet regimes can be found [57]:

- dissipated laminar jet ($Re_j < 3 \cdot 10^2$);
- fully laminar jet ($3 \cdot 10^2 < Re_j < 1 \cdot 10^3$);
- transitional or semi-turbulent jet ($1 \cdot 10^3 < Re_j < 3 \cdot 10^3$);
- fully turbulent jet ($Re_j > 3 \cdot 10^3$).

If the jet is laminar it undergoes a turbulent transition that starts from the jet boundary, because of the instability of such region. However, in gas turbine internal cooling applications Re_j values are generally high, so only fully turbulent jets will be discussed.
As shown in figure 1.5, the flow field generated by an impinging jet can be divided into three zones:

- the free jet zone, located directly downstream the exit nozzle;
- the stagnation region, in which jet impacts the solid surface;
- the wall jet region, located all around the stagnation region.

The *free jet zone* is the first region encountered by the jet downstream the exit orifice. In such region, the jet behaves like a free submerged

jet, as it is not influenced by the presence of the target wall. Here, the velocity gradients between the jet and the surrounding fluid create a strong turbulent mixing zone, the *shear layer*. As a consequence, momentum is transferred laterally outward, entraining the surrounding fluid and raising the jet mass flow. During this process, the jet loses energy and the spanwise velocity profile is widened in extension and decreased in magnitude, thus spreading and slowing down the jet. The central jet region, unaffected by this momentum transfer and thus internal to the shear layer, is called *potential core* (see figure 1.5). This region retains a higher total pressure, though it may experience a drop in velocity and a pressure decay resulting from velocity gradients present at the nozzle exit. Moreover, the shear layer expands also towards the center of the jet, thus the potential core section is reduced along the jet direction: as a consequence, the *potential core* extension is limited downstream to four to eight nozzle diameters.
The dispersion of the potential core corresponds to the beginning of the jet decaying region: turbulence increases and axial velocity in the core decreases, while the jet continues to spread sideways (*developing zone*). Once the jet flow field is completely developed (*fully developed zone*), the axial velocity radial profile comes to resemble a Gaussian curve, with the maximum on jet axis and values gradually decreasing towards the sides [7]. In this region, the axial velocity and jet width vary linearly with axial position. However, in the majority of impingement applications the distance between the nozzle and the target surface distance is limited, thus the axial extension of the potential core is bounded by the solid surface itself, rather than by the jet turbulent development.

The free jet region is one of the main sources of turbulence and unstable flow structures for the whole impingement flow: the shear layer generates flow instability similar to the Kelvin-Helmholtz one, especially at higher Reynolds numbers. Directly after the nozzle exit, the position and velocity profile of the shear layer may develop oscillations in space that wander from side to side over time. Further downstream, the magnitude and spatial extent of these oscillations grow to form large-scale eddies along the sides of the jet, a scheme of whose is depicted in figure 1.6. The largest eddies have a length scale of the same order of magnitude as the jet diameter, and persist until they either break up into smaller eddies or meet and interact with other downstream flow structures.

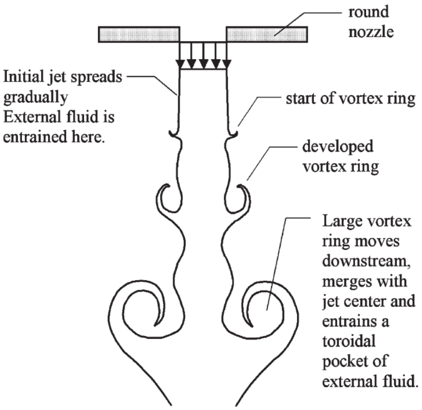

Figure 1.6: Instability in the turbulent free jet [8].

Even the decaying jet region promotes turbulence, but on smaller scales: the shear layer extends throughout the center of the jet, forming small eddies and turbulent pockets in the core region. If the distance from nozzle to target surface is sufficient, such turbulent jet can develop into a completely unstructured flow field, with little to no coherent structures in the entire jet core. Such jet dispersion greatly reduces impingement heat transfer performance, thus in the most applications nozzle-to-target distance is held low: for a typical gas turbine, such distance varies from 1 to 3 times jet nozzle diameter [66].

When the flow approaches the solid wall it interacts with the surface, thus defining the *stagnation zone*. In proximity of the target surface, the axial velocity component decreases and is transformed into an accelerated radial component: this leads to the generation of a favorable pressure gradient and thus of a laminar boundary layer surrounding the stagnation point. However, the increase in velocity along the wall keeps the boundary layer thin, thus creating high temperature gradients [67]. Therefore, stagnation zone shows high heat transfer rates, even if convective phenomena are negligible (velocity is null at the stagnation point) [66].

The stagnation zone is surrounded by a region in which the flow moves radially outward parallel to the wall (*wall jet zone*). In this region, the flow slows down because of both the interaction with the solid wall and the entrainment of the surrounding fluid; moreover, for a round jet flow passage area increases with the radial distance from the stagnation point, thus mass conservation results in additional deceleration. Such conditions create a decelerating region all around the stagnation zone, where the velocity profile presents a maximum in the proximity of the wall and zero values at the free boundary and at the wall itself [68] (see figure 1.5). As the wall jet progresses, it entrains flow and grows in thickness, and the location of highest tangential velocity shifts progressively farther from the wall [8]. The initially laminar boundary layer undergoes a turbulent transition that is induced by the impact of large-scale eddies [67]: this causes a local increase in heat exchange, which may result in a secondary peak in heat transfer distribution, but also a strong variation of heat exchange pattern over time, as the transition is determined by large scale unsteady structures.

The described flow structures cause the heat exchange distribution on the wall to present a peak directly at the jet stagnation point (due to the thin laminar boundary layer) or at a determined radial distance from it (due to the transitioning boundary layer), or even both peaks in certain flow conditions. As illustrated in figure 1.7, the trend of Nusselt number is mainly affected by the ratio between the nozzle diameter (D) and the distance between that and the target surface (H).

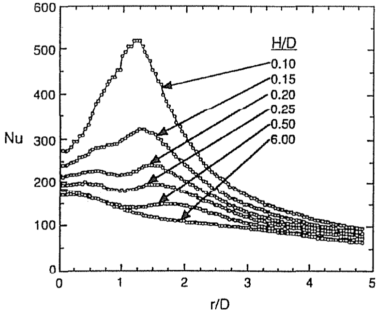

Figure 1.7: Examples of radial Nusselt number distributions for different jet-to-target plate distances [7].

1.6 Film cooling

Even the most effective internal cooling system usually does not allow to obtain satisfactory temperature distributions along the blade, in terms of both uniformity and maximum values. Thus, in order to achieve effective protection of the blade from the hot mainstream gas, a combined application of internal and external cooling techniques is required. An extremely effective way to protect blade surface can be obtained by means of an external cooling technique named film cooling. There is no better way to describe film cooling than using Goldstein's definition: "Film Cooling is the introduction of a secondary fluid (coolant or injected fluid) at one or more discrete locations along a surface exposed to a high temperature environment to protect that surface not only in the immediate region of injection but also in the downstream region"[24]. This definition underlines that film cooling is not a *cooling* method but a protection system aimed at generate a thin layer of coolant around hot surfaces: since coolant is at a lower temperature than the mainstream, heat transfer into the airfoil is reduced. Film cooling is widely used on blades, nozzles and endwalls; in figure 1.8 cooling flows in a nozzle guide vane can be appreciated.

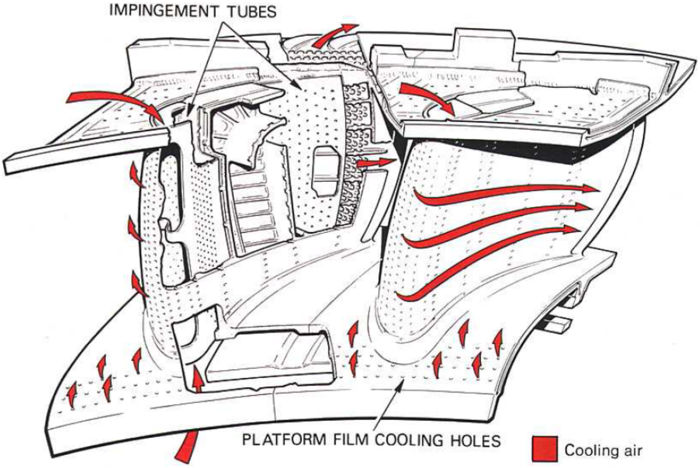

Figure 1.8: Schematic cooling flows in a Nozzle Guide Vane, [3].

One of the most important parameter used to characterize film cooling performance and having a predominant effect on airfoil design process is adiabatic effectiveness η_{aw}:

$$\eta_{aw} = \frac{T_g - T_{aw}}{T_g - T_c} \tag{1.2}$$

where T_g is gas temperature, T_c is coolant temperature and T_{aw} is the adiabatic wall temperature. When η_{aw} is equal to zero, it means that film cooling is not present and T_{aw} coincides with the hot gas temperature T_g. When η_{aw} is equal to 1.0, it means that the film generates a complete protection of the blade and T_{aw} coincides with coolant temperature T_c. Another parameter used for defining film cooling performance is $NHFR$ (Net Heat Flux Reduction), defining the ratio of reduction in the heat transfer to the blade with film cooling to the one without film cooling:

$$NHFR = 1 - \frac{\dot{q}}{\dot{q}_0} = 1 - \frac{HTC}{HTC_0}(1 - \eta_{aw}\Theta) \tag{1.3}$$

$$\Theta = \frac{T_g - T_w}{T_g - T_c} \tag{1.4}$$

where Θ is the non-dimensional temperature. Adiabatic effectiveness has to be high enough to compensate HTC enhancement due to film cooling, otherwise the overall heat load can not be reduced [69].

Ideally, a film of coolant had to be introduced using a slot with an angle almost tangential to the surface in order to provide a uniform coolant layer. However, long slots would seriously reduce the structural strength of the airfoil, and hence are not feasible. For that reason coolant is usually introduced using rows of cylindrical holes; a major advancement has been achieved in the past years due to the introduction of an exit shaping on the holes allowing a lower momentum coolant injection with a greater surface area [70].

Most important correlations for evaluating film cooling adiabatic effectiveness are dependent from geometrical and fluid dynamic conditions; non dimensional parameters like blowing ratio BR (Eq. 1.5), velocity ratio VR (Eq. 1.6), density ratio DR (Eq. 1.7) and momentum flux ratio I (Eq. 1.8) are defined in order to characterize film cooling behavior and the phenomena related to jet-crossflow interaction. Generally, the most influencing parameter is the blowing ratio, representing the jet momentum augmentation compared to the main flow momentum, for constant DR values.

$$BR = \frac{(\rho v)_c}{(\rho v)_g} \tag{1.5}$$

$$VR = \frac{v_c}{v_g} \tag{1.6}$$

$$DR = \frac{\rho_c}{\rho_g} \tag{1.7}$$

$$I = \frac{(\rho v^2)_c}{(\rho v^2)_g} \tag{1.8}$$

Film cooling holes shape can be different from cylindrical: many studies have been performed over the years for increasing coverage and adiabatic effectiveness values. Most used configurations are slot cooling, figure 1.9a, and shaped hole cooling, figure 1.9b; a detailed state of the art including innovative geometries and techniques is reported by Bunker [71].

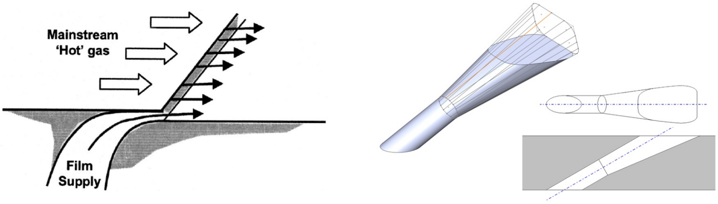

(a) Slot cooling geometry, [71].

(b) Public shaped hole geometry, developed by Penn State University [72].

Figure 1.9: Most used film cooling configurations in gas turbine components.

Most used adiabatic effectiveness correlation used in gas turbine cooling are developed by L'Ecuyer and Soechting [73] and Baldauf et al. [74] for cylindrical holes, while for slot cooling in gas turbines, the most famous is the one developed by Goldstein et al. [75]. Regarding shaped holes, Colban et al. developed a very useful correlation [76] considering outlet over inlet area ratio and the exit area modification when using trapezoidal shape instead of a cylindrical one. Technical literature does not offer open theoretical expressions or correlations to predict film effectiveness in the case of multi-rows configurations. Therefore, it is necessary to adopt theoretical approaches to take into account film cooling superposition effects. Among the few published works concerning film superposition, the most relevant is the model proposed by Seller [77] which is observed to be sufficiently accurate to predict the adiabatic effectiveness distribution at least for the first rows of holes (see for example the works by Harrington et al. [78], Ceccherini et al. [79]). An energy-based model for predicting the additive effect of multiple film cooling rows is recently proposed by Kirollos and Povey [80], comparing its predictions with CFD data and with the Sellers method: the proposed model is shown to be advantageous in situations where energy conservation is required to avoid under-prediction of adiabatic effectiveness.

1.7 Showerhead

Leading edge blade region is particularly troublesome for two main reasons:

- leading edge geometry is unfavorable for internal cooling, because curvature forces internal area to be smaller than external area; as a consequence, the surface available for cooling is less extended than the surface exposed to the hot gases;

- the mainstream stagnation point is located in such region, which implies the highest temperature and static pressure values of the whole blade profile.

Moreover, this region cannot be protected by means of film cooling (see section 1.6), because hot gases impact would flatten and disperse any cooling jet injected into the mainstream.

Therefore, showerhead technique has been developed with the aim to cool leading edge area. Such system consists in the manufacturing of several small holes in the blade wall, through which cooling flow is circulated: this allows to remove heat directly from the material thickness, thus achieving a heat sink effect. The relative small length of the holes increases this effect, preventing a complete development of the boundary layer and taking advantage of the high heat transfer typical of transitioning flow.

Shower head holes are usually realized with their axis inclined with respect to the profile normal direction, to prevent hot gas ingestion; moreover, this solution allows to increase holes length and consequently heat exchange surface. Despite that it ejects exhaust air into the main flow, it is classified as an internal cooling system, since its main aim is to remove heat from the material thickness instead of to protect the blade from the hot gas like film cooling.

1.8 Advanced cooling schemes

In a typical nozzle or blade used in gas turbine, previously cited cooling and protection systems are used together, increasing the geometry complexity: an example of a complete NGV cooling system can be seen in figure 1.8, where impingement, turbulated channels and film cooling are shown in the airfoil's section. Both industrial and academic *R&D* activities are focused on analyzing the effects of combining different cooling systems together, always in order to maximize thermal performances, like *Lamilloy* [9, 81], that consists of a mix of impingement holes, pin-fins and film cooling, figure 1.10.

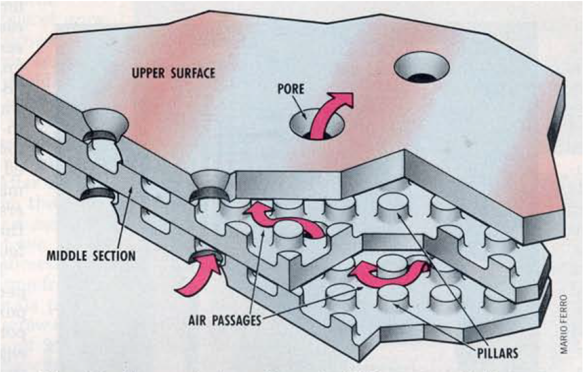

Figure 1.10: Allison's Lamilloy cooling method, [9].

This cooling systems is developed by Allison Advanced Development Company and it's composed by different metal sheets joined together in order to create a sort of transpiration cooling or micro-cooling [82]; impingement and film cooling holes are staggered and interrupted by pin-fins, with the goal of maximize the heat transfer surface and increase thermal performance. Other combined systems can be for example impingement with turbulators [83, 84, 85], impingement and dimples [86, 87] or pin-fins and dimples [88, 89]: geometrical schemes of these cooling systems are shown in figure 1.11.

Double wall solution is a cooling system developed with the goal of widely increase the heat transfer total area by creating a small gap between internal and external blade surfaces in which the cooling air can flow. Flow inside the double wall can move radially with a multi-pass geometry, axially going counterflow respect to hot gas or just in a small portion of the blade with the only goal to feed specific film cooling holes. It's not easy to find open literature works dealing with double wall geometries, since they have a strong impact on industrial design practices: for that reason many double wall geometries are patented and some of the most interesting configurations are reported in figure 1.12.

Innovative film cooling holes and cooling systems described before can be very interesting in terms of adiabatic effectiveness and heat transfer performance respectively, but difficult to be realized using casting, EDM (Electrical Discharge Machining), chip removal or in general subtractive manufacturing techniques. With an increasing complexity in gas turbine component's cooling system geometry, innovative strategies like using additive manufacturing techniques (3-D printing) can be mandatory. Recent developments in this field, like the possibility of using titanium or nickel alloys powder in DMLS, or the development of new thermal treatments for increasing component strength and resilience, allows to directly produce gas turbine nozzle or blade starting from a 3D CAD drawing. Many 3-D printed components are at this moment mounted on operative jet engines, after receiving the approval from United States FAA (Federal Aviation Administration) [90]. Some authors are working to find a way for evaluating the better build direction or surface roughness (and its effect on fluid flow and heat transfer) with the use of CT scan

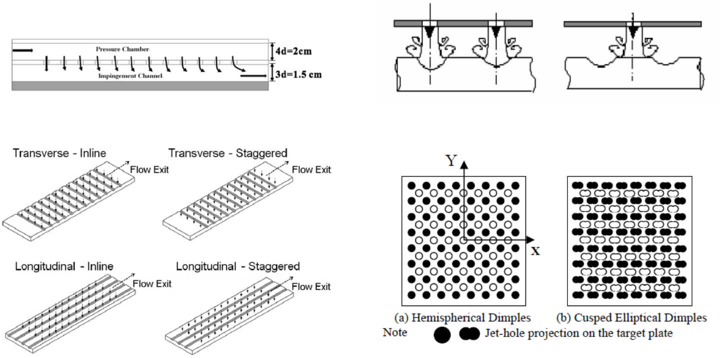

(a) Impingement on different grooved surfaces, [84].

(b) Impingement on dimpled surfaces, [86].

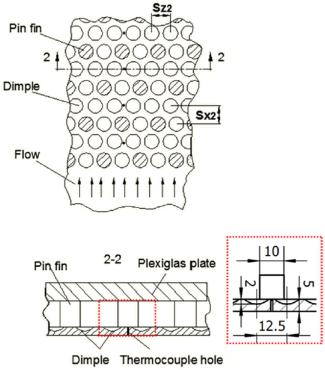

(c) Pin-fins with dimpled surfaces, [89].

Figure 1.11: Schematic representations of different combined cooling configurations.

[91, 92] and even if there are still many problems in predicting residual stresses accumulated during the build [90] and we are far from having design guidelines or best-practices, additive manufacturing techniques can totally rewrite the rules of how engineers design and realize the entire gas turbine component with its integrated cooling system.

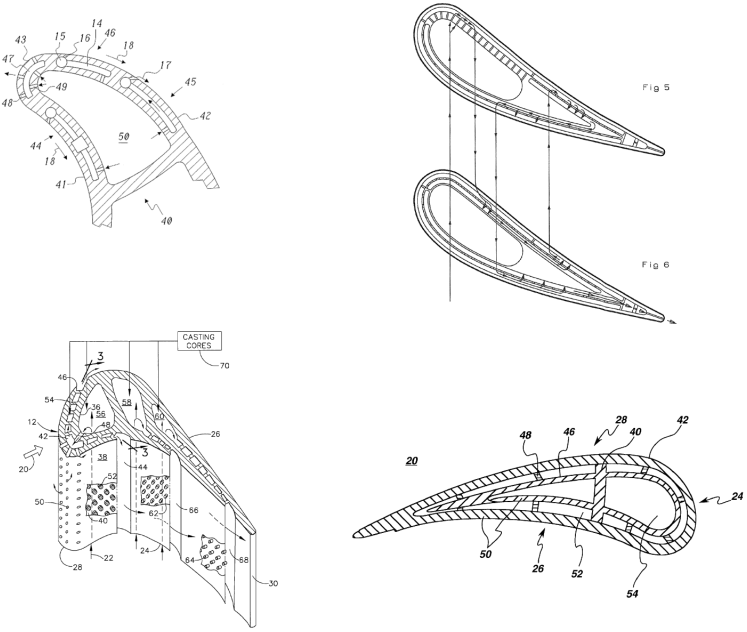

Figure 1.12: Different double wall configurations [10].

1.9 Effect of rotation on internal cooling systems

In gas turbine applications, cooling techniques are applied to both vanes and blades: in the latter case, the system is defined in a rotating frame of reference, thus internal and external flows are strongly influenced by the effects of fictitious forces arising. In particular, coolant passing through a rotor blade internal duct experiences strong Coriolis and rotational buoyancy forces. These forces generate secondary flows that significantly alter internal flow field, thus affecting mass flow distribution and heat transfer both in cooling channels and in all the connected downstream cooling systems. The influence of rotation on the flow field can be expressed as a function of the the Rotation number, a dimensionless parameter defined as:

$$Ro = \frac{\Omega D}{u} \tag{1.9}$$

where Ω is the rotation speed, D is the characteristic length (channel hydraulic diameter in the present case) and u is the average axial velocity. An intuitive interpretation of the origin and consequences of Coriolis force in rotating channels can be expressed as follows. Assuming a Lagrangian approach and following a particle of fluid as it moves radially outward in a cooling passage, it encounters an environment with a higher circumferential velocity than that from which it is moving out: so, the fluid particle tends to be overtaken by the channel 'trailing' surface (that in a turbine blade corresponds to the pressure side). As a consequence, an asymmetrical mass flow pattern can be expected, as the coolant tends to impinge and flow along the trailing surface, thus increasing the convective . The converse situation is obtained on the opposite 'leading' surface (which corresponds to the suction side), where a reduction of heat transfer can be expected. On the contrary, for a radially inward motion the fluid particle tends to have a larger circumferential velocity than the solid walls bounding the flow: thus, the fluid overtakes the 'leading' surface and the heat transfer enhancement is obtained on this surface rather than on the 'trailing' surface. These effects of rotation are illustrated in figure 1.13.

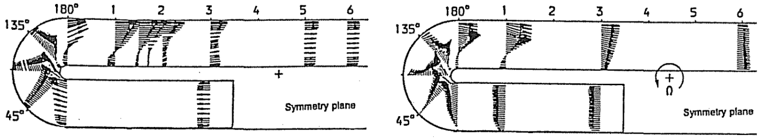

Figure 1.13: Velocity distribution in an U duct in static (left) and rotating (right) conditions [11].

The ideal bidimensional behavior described above becomes way more complex in a real three-dimensional channel geometry. In such case, the different radial velocities present in a channel cross-section profile cause the fluid to behave differently to the Coriolis force in different zones of the section. As a result, two counter rotating vortices are formed inside the passage, which shape and size depends upon the channel section, and which orientation is defined by the radial outward or radial inward direction of the flow, as it is illustrated in figure 1.14.

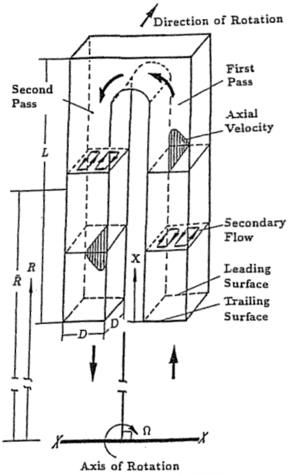

Figure 1.14: Secondary flows in a rotating U duct [12].

In a rotating frame of reference, the whole system is subject to a centripetal acceleration field, which can interact with fluid density gradients, thus generating buoyancy forces. Such centrifugal effect is particularly strong in gas turbine blades cooling systems, given the high rotational speed of such machines. Moreover, in these systems the coolant flow heats up along the cooling channels, as it removes heat from the blade material: this causes its density to decrease, thus generating a density gradient along the radial channel, i.e. along the centrifugal field. As a result, rotational buoyancy forces arise, whose effects add to the Coriolis-induced distortion and further modify the flow field, as presented in figure 1.15

The phenomena briefly described above have an influence not only for

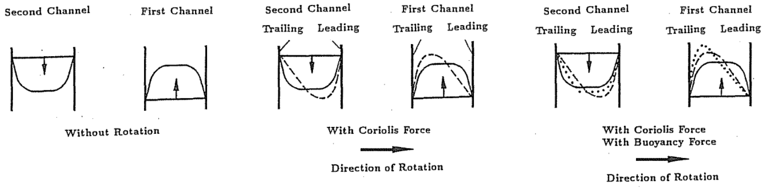

Figure 1.15: Conceptual view of effects of inertia, Coriolis, and rotational buoyancy on radially outward and inward flows [12].

the cooling channels internal flow, but also for the other cooling systems that draw coolant from such channels. Fore a more complete analysis on rotation effects, please refer to [66].

1.9.1 Impingement with rotation

In the case of an impingement jet, rotation effects strongly depend upon the relative position of impinging direction and rotation axis. If such directions are parallel, the jet flow is not directly affected by the Coriolis force before arriving at the target surface, but the flow field is significantly altered in the wall jet region. As illustrated in figure 1.16, the fluid spreading around the stagnation region acquires a turning motion contrary to the domain rotation, thus generating a swirling secondary flow which enhances the jet mixing with the surrounding fluid. This causes a decrease of jet momentum reaching the target surface and a thickening of the wall boundary layer, thus reducing jet heat exchange performance.

If the jet direction and the rotation axis are not parallel, the jet itself is deflected by the action of Coriolis force. For an impingement jet lying in a tangential plane, the deflection is outwards the axis if the jet has a leading orientation (i.e. if jet and tangential velocity form a angle lesser than 90°), towards the axis if the jet has a trailing orientation, as illustrated in figure 1.17. The combination of Coriolis and centrifugal force can enhance or reduce this effect, but in any case jet velocity component perpendicular to the target surface diminishes and impingement heat exchange decreases.

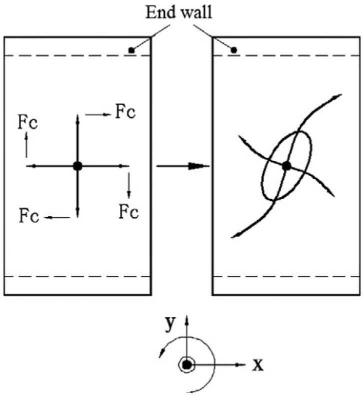

Figure 1.16: Effect of Coriolis force on wall jet flow for a jet parallel to rotation axis [13].

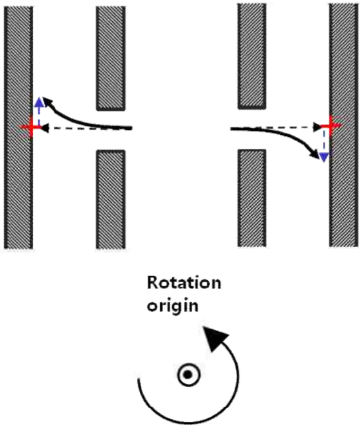

Figure 1.17: Effect of Coriolis force on jet direction for leading (left) and trailing (right) orientations [14].

These simple theoretical effects can be further modified by the interactions of rotation with other thermal and fluid-dynamic features of the impingement system, like the influence of Coriolis force on feeding channel and the buoyancy effect of density gradients under the centrifugal flow field.

Chapter 2

Experimental test-rig

The complex nature of fluid and thermal phenomena involved in impingement technique requires direct measurements on the system to be performed, in order to interpret the real flow field, to control boundary conditions and to isolate the various dependencies and influences. An experimental test campaign of the investigated cooling system has been carried out, allowing to analyze flow field and heat exchange phenomena in imposed and controlled conditions, with the aim to observe the actual behavior of the system.

Since the experimental survey was aimed to assess, inter alia, the effects of rotation on both the flow-field and the heat transfer, the rig has been designed to perform measurements in both static and rotating conditions. As mentioned above, these analysis were performed separately in two analogous test rigs. The flow-field was investigated through Particle Image Velocimetry (PIV) measurements at the Department of Electrical, Management and Mechanical Engineering of the University of Udine. Meanwhile, the distribution of heat transfer coefficient on the leading edge internal surface was evaluated by means of Thermochromic Liquid Crystal (TLC) measurements at the Industrial Engineering Department of the University of Florence. Both the two test rigs were set up in order to impose the required flow conditions in the test section and to record all the variables requested for the analysis of the phenomena. In the present chapter, the experimental apparatus exploited for such measurement campaign is reported, including the test rig, the ”cold bridge” model, the measurement techniques and the post processing procedure.

2.1 General layout

As the experimental work done by the author mainly regards the campaign on the heat transfer coefficient distribution, in the present section the test rig exploited at the University of Florence is described. Regarding the test rig designed for the flow field investigation, just a brief description of the differences with the one here reported will be presented at the end of the paragraph.

The main components of the test rig, a scheme of which is represented in figure 2.1, are essentially:

- rotating frame, which hosts the heat exchange section as well as part of the flow measurement and control apparatus;
- aeraulic rotating joint, which supports the rotating frame and allows the mass flow extraction;
- slip ring electrical interface, which ensures data transfer and power supply to the on board instrumentation devices;
- electric motor, whose task is to spin the rotating assembly in dynamic tests;
- model, which represents the investigated geometry and on which the main measurements are performed;
- aeraulic system, which deals with the mass flow distribution, measurement and control and includes the central plenum, three extraction plenums, valves (v), orifices (o) and a set of connection ducts;

- two couples of vacuum pumps, one with lower capacity (p) and one with higher capacity (P), which allow air circulation inside the test rig;
- video acquisition system, which permits the acquisition of TLC coated surface images;
- temperature (T) and pressure (p) measurement systems;
- acquisition and control system, performed by means of a personal computer (PC).

Given the importance of any of these components, they will be discussed in detail in the following sections.

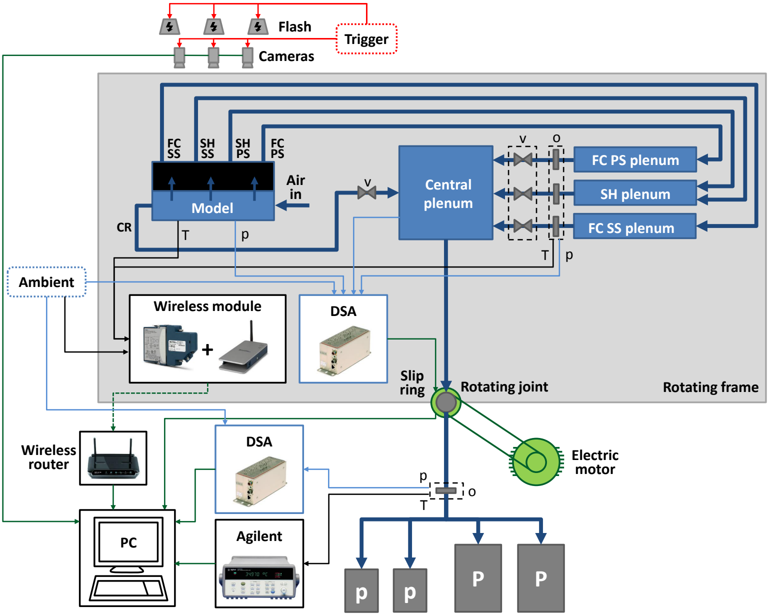

Figure 2.1: Test rig scheme.

2.2 Leading edge model

The model investigated in the present work is a scaled down and slightly modified version of the AVIO C3 geometry studied in the framework of ERICKA project [57], which replicates in an enlarged scale (43:1) a realistic leading edge internal cooling system of a high pressure gas turbine blade. The original AVIO C3 geometry has been scaled down with a scale factor of 0.7 (obtaining a global new SF of about 30) to satisfy the similitude requirements in terms of Rotation number with respect to the real engine geometry, considering a rotational speed of 200 rpm of the rig. For more details refer to [58]

As depicted in the sectional view of the analyzed model in figure 2.2, a trapezoidal feeding channel supply the cooling air to the model through its inner radial extremity. A part of it enters three holes located on an impingement plate and generates three jets, which impact on the LE internal surface. The mass flow not entering the impingement holes is extracted from the model at the radial outer extremity of the feeding channel.

Impingement plate is 30.1 mm thick and houses three large racetrack shaped holes with an exit hydraulic diameter $D_h = 35.5$ mm, a ratio between the lower and the higher length of the hole and the hydraulic diameter of respectively $l/D_h = 0.85$ and $L/D_h = 1.14$ and a radial-wise spacing $P_x = 133.5$ mm. The holes section major axis lies in the radial direction, and they are connected to the channel wall through a wide radius fillet. Such holes grant the coolant the access to the outer cavity, representing the leading edge cooling section itself. Its most important geometric dimensionless parameters are the jet-to-target ratio $Z/D_h = 2.34$, the target plate curvature $D_{LE}/D_h = 1.11$ and $P_x/D_h = 3.75$. The axis of the model central jet is located at a radius of 750 mm. Four big fins are located on the impingement surface, with the aim to confine the impingement jets in order to limit their radial dispersion and to isolate the three jet impact zones: this permits to define three distinct impingement modules. The extraction of the spent coolant

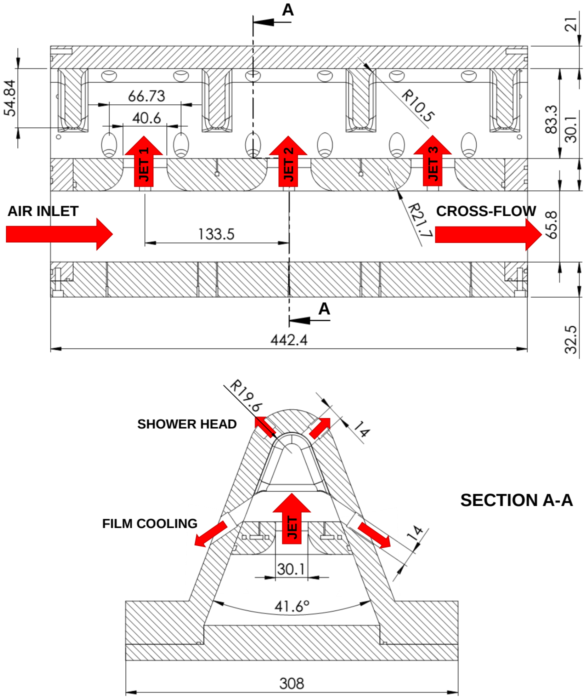

Figure 2.2: Sectional view of LE model. Measures are in mm.

flow from the impingement cavity takes place by means of four rows of six holes each, simulating the effect of showerhead (the central two rows, SH) and film cooling (the outer two rows, FC) systems on impingement cooling. These extraction holes have a diameter of 14 *mm*; such choice, which imply the adoption of a different scaling factor for them [58], represents a compromise which allowed to achieve an adequate extraction area value, a suitable geometry and at the same time to maintain industrially significant impingement-to-extraction hole diameter ratio ($D_j/D_{FC,SH} = 2.55$). As the heat exchange measurements were performed by means of optical thermometry, the model is entirely made of transparent PMMA, in order to obtain both complete optical access to the inner geometry and thermal insulation.

2.3 Rotating equipment

As already mentioned, the test rig has been realized to perform rotating tests, thus the model and the principal rig components need to be supported by a suitable structure. As a consequence, the elements developed and used for previous rotating experiments performed in the same laboratory have been exploited [93]. The test article, the extraction plenums and part of the measurement instrumentation are installed on the rotating chassis; it has an horizontal axis of rotation and a radius of 1100 mm, and has been realized keeping in mind both the tests specifications and the available space. To adequately support all the equipment at high rotating speeds, its structure is made of welded Fe510 square profiles. A rotary joint realized by Celco® Profil performs the multiple tasks of supporting the rotating assembly, transmitting the motion to the chassis, extracting spent air from the test section and ensuring power supply and data transfer to the on board instrumentation. The latter task is made possible by the presence of slip rings, which permit the passage of up to eight Ethernet channels. The rotation is obtained by means of an electric motor (Marelli 7.5 kW three-phase asynchronous) controlled by an inverter (Lenze 7.5 kW 400 V), located below the joint and connected to it by means of a toothed belt. The whole assembly is supported by a steel frame and linked to the ground by means of damping supports. To ensure the safety of the laboratory environment, the rotating equipment is totally enclosed in a modular steel cage.

2.4 Air circuit

The aeraulic network has been built to ensure the reproduction of the correct flow conditions inside the model. The tests are performed in depression, thus ambient pressure air is introduced into the model by means of an inlet section, containing a foam filter and an honeycomb. The shape of such component and the thickness of the filters is designed to ensure a uniform flow into the model, in spite of the surrounding components and even in rotating conditions [94]; moreover, the possibility to locate the filters, and thus the “uniform” flow condition, at different radial positions allows to more realistically simulate the flow development into the radial feeding channel. After the inlet section, air enters the model itself, where a part of the flow enters the three impingement holes and evolves into the cooling cavity, and the remaining part exits the model at the other side of the feeding channel and thus defines the crossflow.

The spent impingement flow is drawn from the model through the four rows of extraction holes: the outer film cooling rows are connected to a plenum each, while the two central showerhead rows are both linked to a single plenum, using ducts with all the same length to ensure uniform losses. The three extraction plenums are installed at the opposite side of the rotating frame with respect to the model, and every extraction hole in the model is linked to an inlet hole in the plenum located at the same radius: in such way, the radial pressure gradients due to rotation can be compensated, and every hole of a row can work with the same pressure drop between the model and the plenum in both static and rotating conditions. Air leaves each of the three plenums through a short duct housing a calibrated orifice and a gate valve, which are used to respectively measure and control the mass flow rate trough the plenum.

At the opposite side of the model, the feeding channel is connected to a crossflow plenum, from which two ducts bring back air in the radial inward direction and converge in a single duct near the rotation axis; again, a gate valve permits mass flow adjustment. The three extraction holes flows and the crossflow all converge in a central plenum, from which air enters the hollow rotary joint and reaches the pumps.

The suction system is made of two couples of vacuum pumps, each in parallel configuration: a couple is manufactured by PVR and has a total capacity of 1800 m^3/h, the other is realized by Becker and has an overall capacity of 600 m^3/h. The machines are powered by a three-phase asynchronous electric motor each. Each couple gets controlled by means of a suitable control board, which allows to independently start or stop each pump and to continuously vary their speed through an inverter.

An image of the complete rig layout is presented in figure 2.3

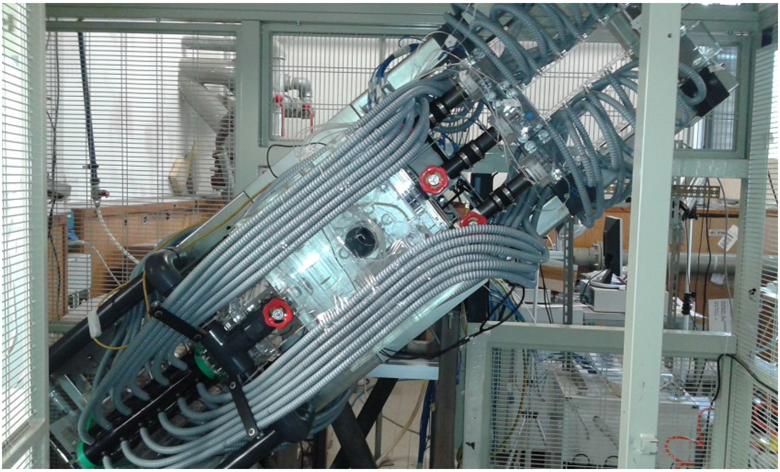

Figure 2.3: Picture of the rig assembly.

2.5 TLC thermography

The analysis of heat exchange performances of a complex cooling system requires a point-by-point knowledge of temperature on the heat exchange surface, in order to extract the distribution of heat transfer coefficient on the investigated section. To achieve such goal, a suitable technique consists in the application on the surfaces of interest of temperature sensitive coatings: in particular one of the most widely applied methods is the use of thermochromic liquid crystals (TLC), as the chromatic properties of such substances are related to their temperature. In recent years, the decreasing costs of display equipped electronic devices and the improvements in manufacturing and application of such coatings have caused an increasing diffusion of TLC: in fact, such technique presents many desirable features, including a relatively low cost and complexity of application, a small alteration of thermal and flow field, a rapid response time and the possibility to achieve high accuracy and resolution in measurements. The main features of TLC thermography will be briefly expressed in the following sections; for further in formations, please refer to [95], [96].

2.5.1 TLC characteristics

A liquid crystal (LC) is a phase whose properties are intermediate between liquid and solid ones. In fact, the molecules of a LC do not present an order in relative positioning, but they show a regularity in relative orientation: as a consequence, LC possess both the optical properties of crystalline solids and the fluidity of the liquids. A distinctive property of liquid crystals is the dependency of their chromatic characteristics from temperature, as the consequence of the corresponding variation in their molecular structure. In fact, below a precise temperature, called *event temperature*, the crystal appears transparent, because the various molecules are all parallel in their orientation; above the event temperature, the molecules start to rotate the one with respect to the other. As a consequence, if a vector $\vec{n}$ is defined to indicate the average molecular orientation, the envelope of $\vec{n}$ positions inside the LC describes a cylindrical helix. Such structure gives the LC a microscopic periodic structure, which enables it to selectively reflect light, in accordance with Bragg's law [95]. The reflected light wavelength depends upon the period of the microscopic structure, as well as upon the spectral content of incident light and the relative position of the light source and the observer.

As temperature increases, the relative rotation between adjacent molecules increases too, thus decreasing the helix pitch: as a consequence, the reflected wavelength decreases and the LC color shifts from red (long wavelength) to green and eventually to blue (short wavelength). This feature permits to set a correspondence between the temperature and the color of the LC, and thus to use such substance as a temperature measurement device. The non reflected wavelengths pass through the crystal with almost no interaction: to exploit the thermochromic feature of a LC it is thus necessary to provide it with a nonreflecting (usually black) background, so that only the temperature related colored light is reflected and all the other wavelengths are absorbed by the background.The temperature width of the color-play interval is different for various TLC formulations, and allows to classify them as *narrow band* (with an activation rang of $1 \div 2C$) and *wide band* ($5 \div 30C$). Above such range, the LC reaches the transition to the liquid phase (*clearing point temperature*) and returns to transparent again. The commercially available TLC products are formulated as paints, which allow to apply them on a surface and thus to obtain a point-by-point temperature measurement.

2.5.2 HTC measurement through TLC

Local convective heat transfer coefficient measurement for complex geometries is fundamental in many applications, one of the most significant of which is the development of internal cooling systems for gas turbine blades. In such framework, the experimental campaign provides the data requested by the investigation and permits to validate the computational models employed for the simulation of such phenomena.

The most widely applied methods to measure heat transfer coefficient by means of TLC are the *steady-state* or heated coating technique and the *transient technique*, a brief description of whose is presented in this section.

2.5.2.1 Steady-state technique

The steady-state technique directly follows from the application of the first principle of thermodynamics to a control volume including the measurement surface. For the present case, its application leads to a system of the kind depicted in figure 2.4. Such implementation requires the investigated surface to be covered with a conductive coating, which gets electrically heated, as well as with TLC from optical access side. The measurement surface is then exposed to a steady flow of air at temperature T_a until stable conditions are met, which is verified by the time invariance of the chromatic response of TLC. An image of the surface can then be recorded, from the analysis of which the TLC temperature can be obtained: by evaluating the thermal resistance of TLC-to-surface layer (or

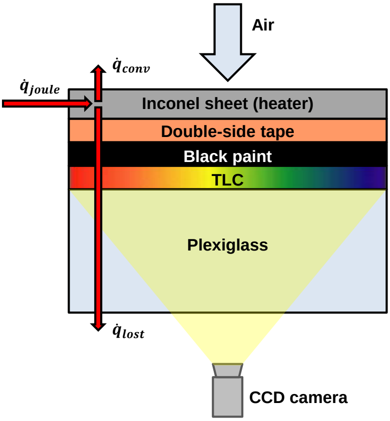

Figure 2.4: Scheme of a steady-state implementation cross-section view.

by ignoring it, in case it is negligible) the surface temperature T_s can then be evaluated. If the heat flux $\dot{q}_{joule}$ generated by the heater is known and the entity of the lost heat flux $\dot{q}_{lost}$ is evaluated, the convective heat transfer coefficient h can be calculated as:

$$h = \frac{\dot{q}_{joule} - \dot{q}_{lost}}{T_s - T_a}. \tag{2.1}$$

If the local values of the variables are known, equation 2.1 can be applied point-by-point and a map of the distribution of h on the whole measurement surface can thus be obtained. While the principle on which steady state technique is based is simple, difficulties can arise in the evaluation of the single terms of equation 2.1: in fact, a correction of the measured temperature can be required to obtain the surface temperature T_s; moreover, the entity of $\dot{q}_{joule}$ and $\dot{q}_{lost}$ can be strongly affected by the transversal conductive heat transfer in the heater (in spite if its reduced thickness, given its usually high thermal conductivity) and in the model material. As a consequence, such technique often needs to be supported by a FEM simulation of the model (see section 2.9.2), to evaluate the local electrical and thermal field. The application of steady-state technique can even be limited by the investigated geometry itself, since it can be difficult to affix the heating element on particularly complex geometries, which limits the availability of this approach only to flat plates or single curvature walls.

Given the features of the performed investigation, the steady-state technique was chosen for the present work: the reasons of such choice will be better highlighted in the following section.

2.5.2.2 Transient technique

To overcome the disadvantages of the steady-state technique with respect to the local resolution and applicability on complex surfaces, transient techniques have been developed, which allow to calculate h from a time-variant heat exchange phenomenon. The method briefly recalled here is the semi-infinite wall method [57]. Such technique requires the test article to be made from a low conductive material (to keep lateral conduction effects small) and with a large wall thickness (so that the thermal variation at the surface of interest does not influence the opposite surface of the model). Under these hypotheses, the conduction into the model can be assumed to be one-dimensional, and the heat transfer can be supposed to take place towards a semi-infinite wall. The model is usually kept at ambient temperature T_i, and as the test starts it is abruptly exposed to a flux with a different temperature T_a (both higher or lower): one-dimensional conduction into the wall can then be described by the the Fourier equation:

$$\lambda \frac{\partial^2 T}{\partial z^2} = \rho c \frac{\partial T}{\partial t}, \tag{2.2}$$

with the given boundary conditions:

$$T(z,0) = T_i \tag{2.3}$$

$$-\lambda \left. \frac{\partial T}{\partial z} \right|_{z=0} = h\left[T_a - T(0,t)\right] \tag{2.4}$$

$$T(\infty,t) = T_i \tag{2.5}$$

where z is the wall normal coordinate. It can be demonstrated [97] that the solution of equation 2.2 with boundary conditions 2.3, 2.4 and 2.5 on the wall exposed to the flow can be expressed as:

$$\frac{T_w(t) - T_i}{T_a - T_i} = 1 - \exp\left[\left(h\sqrt{\frac{t}{\rho c \lambda}}\right)^2\right] \mathrm{erfc}\left(h\sqrt{\frac{t}{\rho c \lambda}}\right), \qquad (2.6)$$

where T_w is the wall temperature ($z = 0$) and erfc is the complementary error function [57]. If the surface temperature T_w at time t is known, the heat transfer coefficient h can be calculated from the previous expression: this is usually made possible through the use of a TLC coating and a video acquisition system.
The transient method main advantage is its applicability to complex geometries and the usually higher achievable resolution [57]; however, this is counterbalanced by a greater complexity in data acquisition system and in post processing, which need to consider the deviance from ideal conditions (instantaneous temperature step and semi-infinite one-dimensional wall).

Despite that the previous studies on a similar geometry (see) were all performed using a transient technique, the rotating nature of the rig gives birth to various constraints which make such technique particularly complex to apply. In fact, video acquisition and illuminating apparatus should be fit on board, thus considerably increasing the size of the rotating assembly, and a perfect temperature step is way more complex to obtain, thus reducing overall measurement accuracy. As a consequence, steady-state method has been chosen, and the test model has been configured for the application of such technique: the leading inner surface of the impingement cavity has been sprayed with TLC and with black paint, and then a 25.4 μm thick inconel heating foil has been applied to the whole measurement surface with a double-side tape, as shown in figure 2.5. To achieve heat generation, the inner and outer radial edges of the foil have been connected to two modular copper bus bars (see figure 2.5), that in turn have been fastened to the model by means of six brass screws. Such screws reach the exterior surface of the model and enable the electrical connection of the foil with the terminals of a power supply.

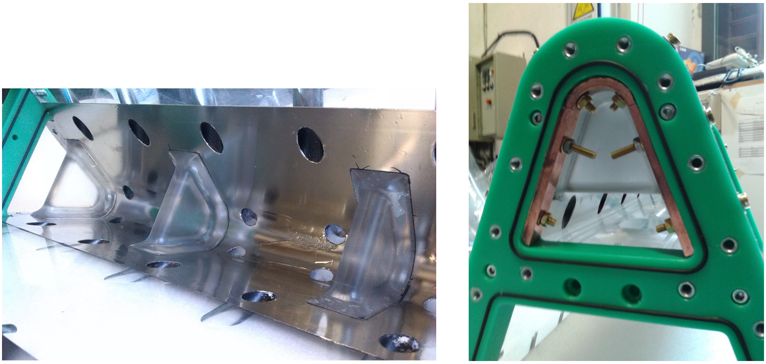

Figure 2.5: Inconel coated model inner surface (a) and bus bar configuration (b).

2.5.3 Use of TLC for quantitative measurements

The use of a TLC coating for quantitative temperature measurements requires the chromatic information to be acquired and associated with the corresponding temperature value. The first task is achievable through the use of a digital image acquisition system, which permits to record one or more images of the TLC coated surface. The interpretation of the image then allows to associate each pixel, and thus its chromatic data, with the corresponding geometric location. That represents a difficult purpose that need the definition of a relationship between the TLC color and its temperature.

The more robust and computationally efficient color descriptors have been defined and applied, depending upon the the particular investigation. In this case the chosen parameter is the *hue*, which allow to reduce the whole chromatic information to a single parameter. *Hue* is defined as:

$$hue = atg\left(\frac{\sqrt{3}(G-B)}{2R-G-B}\right) \tag{2.7}$$

where R, G and B are 0-to-1 red, green and blue color intensities respectively. For more details about such choice please refer to [58].

2.5.4 TLC calibration

The knowledge of the input-output characteristic is an essential feature for the use of any measurement system, and can be obtained by means of a suitable calibration operation. As mentioned in the previous section, in the case of TLC the knowledge of the intrinsic color-temperature response of the crystals is required, as well as of every other feature which can strongly alter such response. However, these features are many and difficult to control, and include the illumination source and its position, the relative angle between the observer and the TLC coated surface, the kind of image acquisition device and the eventual media interposed between the optical system and the measurement section. As a consequence, the calibration of TLC should be directly performed on the investigated system itself, because the invariance of external altering factor allows not to consider their influence on TLC response. However, an in-model calibration requires the test apparatus to be equipped with temperature control devices other than TLC on the measurement surface itself, which is often difficult and can alter the TLC response. To overcome these issues, the most suitable solution is usually the setting of a calibration apparatus able to accurately replicate the test optical conditions. For the present work, the latter solution has been adopted. The calibration has been performed by means of the steady state gradient method (a description of which can be found in Chan et al. [98]), on an apparatus whose optical configuration is as similar as possible to the test section one. To achieve this goal, the calibration device itself has been located in place of the test article for the calibration operation, and the TLC coated surface has been covered with a PMMA flat plate of the same material of the model itself (figure 2.6). In this way, the image acquisition and the illumination systems used for the tests and for the calibration are exactly the same.

The result of the calibration operation is a curve which relates the hue values exhibited by the TLC colors to the corresponding temperature values. Such relation is in general not monotonic, thus only the increasing part of the curve is selected: following this criterion, hue versus tempera-

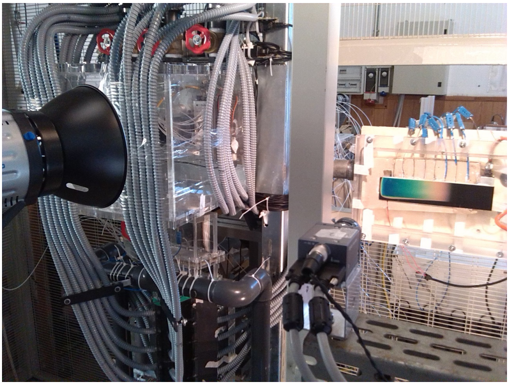

Figure 2.6: TLC calibration apparatus.

ture curves of the kind represented in figure 2.7 have been derived. Since three cameras have been used in the present work, such operation has been performed for each one, which allowed each camera to work with its own curve.

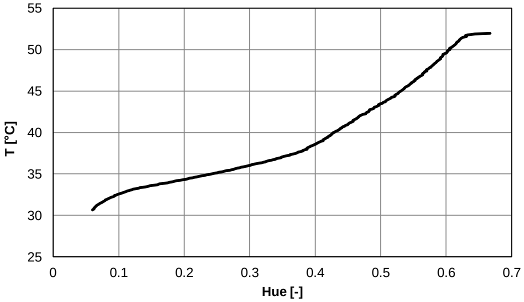

Figure 2.7: Example of a hue versus temperature curve obtained from the calibration.

2.6 Measurement instruments

In order to assess and to control both thermal and fluid dynamic parameters inside the model, the rig is equipped with a series of measurement instruments.

The correct mass flow split into the model and the set up of the correct Re_j are ensured by means of the gate valves which equipped the test rig downstream the several plenums: the cross flow plenum (which allows to control the split between the coolant mass flow and the cross flow) and the three plenums (which allow to control the split between the FC and SH extraction hole rows). The mass flow is measured, according to the standard UNI EN ISO 5167-1, by means of a series of calibrated orifices, measuring the static pressure drop of the air flow passing through them.

Several static pressure taps are located along the test rig: in the impingement cavity, in the rear part of the cross flow channel, in the inlet and outlet ducts of the model, into the central plenum and upstream and downstream each orifice. Static pressure measurements have been performed using two pressure scanners Scanivalve® DSA 3217. Each scanner incorporates 16 temperature compensated piezoresistive pressure sensors with a pneumatic calibration valve, a RAM memory, a 16 bit A/D converter and a microprocessor. The microprocessor compensates for temperature changes and performs unit conversion. Pressure data are output via Ethernet using TCP/IP protocol. To allow pressure to be measured even in rotating conditions, one of the two DSA is mounted on the rotating frame, as close as possible to the rotation axis to minimize the centrifugal force induced deformations of the piezoresistive elements. The various pressure taps have been linked to the different range sensors, with the aim to obtain the best available accuracy without exceeding the maximum sensor range.

Since the definition of the convective heat transfer depends upon the values of flow and wall temperatures, such quantities have also to be measured. As mentioned above, wall temperature has been evaluated by means of TLCs (Hallcrest 30C20W wide band thermochromic liquid crystals with an activation band between 30 and 50°C), while flow temperature has been monitored thanks to several T-type thermocouples (copper-constantan junctions) located along the leading edge model, whose shape allows to position the sensors where needed with little alteration of the flow field.

The choice of TLCs as temperature transducer requires the presence suitable video acquisition system, to record the chromatic information and then extract the thermal data. As a consequence, the rig is equipped with an image recording apparatus composed of three digital cameras (Sony® XCD-SX90CR), an illuminating system and a personal computer. The presence of three cameras is needed by the shape of the measurement surface and by the desire to achieve a full coverage heat exchange map: as a consequence, two cameras are located perpendicularly to the suction side and pressure side respectively, while a third camera focuses on the leading edge curved surface. The use of a steady-state technique allows to obtain the whole temperature field from a single image: as a consequence, the cameras do not need to be fit on the rotating assembly, and can be mounted on a dedicated static frame. In such configuration, the image acquisition takes place when the test article, during the rotation, crosses the cameras visual field. The illumination system has been designed to suit this technique: three Dörr DE 500 W studio flashes have been located in order to minimize shadows and reflections on the measurement surface. A laser transducer is employed to trigger a custom built electronic circuit that drives both cameras and flashes in order to synchronize the whole acquisition system.Fore more details regarding the test rig measurement instruments and techniques please refer to [58].

2.7 PIV measurement technique

As aforementioned, the test rig exploited at the Department of Electrical, Management and Mechanical Engineering of the University of Udine for the flow-field investigation is analogous but slightly different from the one described above. Indeed, the test rig exploited for Particle Image

Velocimetry (PIV) measurements, a detailed description of which is available in [99], was characterized by a vertical axis rotating system. Velocity measurements were performed by means of 2D and Stereo-PIV techniques. The PIV system is custom-made and features a Litron Ltd. 200 mJ double cavity Nd-YAG pulsed laser and two PCO Sensicam cameras with cooled 12bit CCD with a resolution of 1024x1280 pixels. Cameras mount Nikkor optics with either 105, 60 or 35mm fixed focal length and two-axis Scheimpflug adapters for stereo viewing. Cameras and laser are connected through the synchronization and acquisition systems. The seeding was provided by a Laskin-nozzle-type seeding generator operated with vegetable oil, which guarantees a very narrow particle size distribution with an average diameter of 1.2 μm.

For both 2D and Stereo-PIV data, the commercial software PIV view (from PIVTEC Gmbh) was used to perform the processing of the image pairs. In particular, for Stereo-PIV data, image back-projection and then stereo reconstruction were computed; furthermore, a disparity correction was also used in order to minimize the misalignment errors [100].

Concerning the measurements under rotation, it has to be underlined that the present PIV system is stationary; therefore, a phased-locked configuration has been adopted. Since the measurement output is the absolute velocity field, a more complex pre- and post- processing procedures [101, 102] were adopted in order to get an accurate reconstruction of the relative velocity field inside the test section.Detailed description of the investigated planes in the PIV experimental campaign, as well as validation of the rotating and stereo-PIV tests, can be found in [99]. In order to have a deep understanding of the impingement jets evolution the two planes showed in figure 2.8 were chosen for the PIV measurements. The reference system has origin in the rotating axis in the model symmetry plane, the z-axis is centered on the impingement plate side facing the LE cavity.

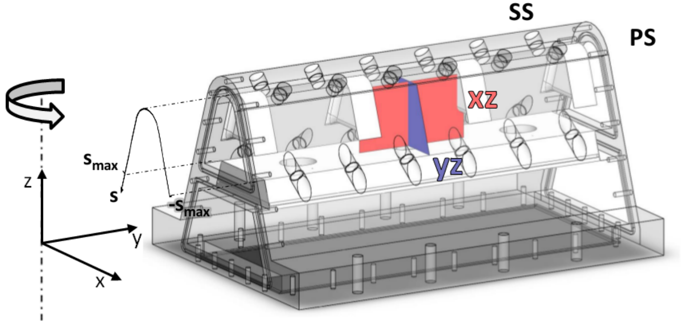

Figure 2.8: PIV reference system and investigated planes

2.8 Experimental uncertainty

2.8.1 HTC uncertainty

The experimental uncertainty assessment on the measured values of heat transfer coefficient was performed locally, for every measured point, according to the standard ANSI/ASME PTC 19.1 [103], based on the Kline and McClintock method [104]. Among the variables considered in this calculation, given its definition (equation 2.1), the difference between coolant and target surface temperatures is the leading parameter for uncertainty increase. Due to such reason the maximum value of local uncertainty occurred on the jet impact regions, where the air-wall temperature difference is smaller than any other point on the investigated area. The maximum local uncertainty was verified for tests performed at $Re_j = 40000$, and its value stood at around 20% for static tests, while it reached around 30% for rotating tests because of the lower accuracy of on-board cold junction compensation. Nevertheless far from jet impact zones the uncertainty is usually under 10%, resulting in average values always lower than 13% and 14% for static and rotating tests respectively.

An overview of the average uncertainties for every test performed is reported in its evolution with Re_j in figure 2.9.

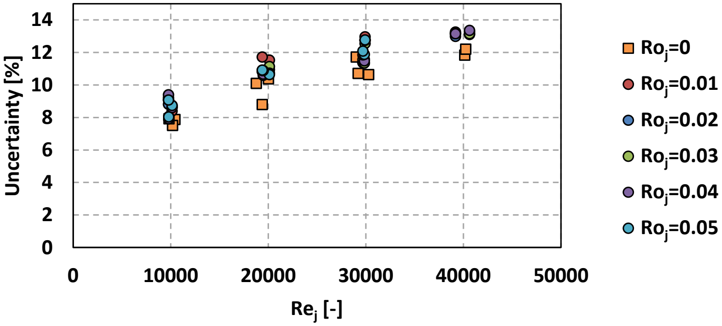

Figure 2.9: Average heat transfer coefficient uncertainty for the whole test matrix

2.8.2 Uncertainty of flow field measurements

The results presented during this dissertation refer only to statistical quantities, such as the time averaged velocity fields. Since a limited number of samples (1000) was exploited to compute the flow statistics, the sampling error tends to be larger than other error sources and therefore it was chosen as the overall upper bound estimate for the PIV data uncertainty.

For the 2D measurement under static conditions, the normalized r.m.s. errors in the statistical quantities are computed as in Armellini et al. [105]:

$$\epsilon_U = \frac{\sigma[U]}{|U|} = \frac{1}{\sqrt{N}} \cdot \frac{u'}{|U|}, \epsilon'_u = \frac{\sigma[u']}{u'} = \frac{1}{\sqrt{2N}} \tag{2.8}$$

where σ is the standard deviation, U is the mean velocity, u' is the r.m.s. velocity fluctuation and N is the number of independent samples. The uncertainties in the measured values of U and u' are simply obtained by multiplying the errors in Eq. 2.8 by a confidence coefficient, Z_c. Assuming values $Z_c = 1.96$ (corresponding to a 95% confidence level) and N = 1000, the overall upper bound estimate of the uncertainty in the mean velocities turns out to be less than 2%. This value was applied to the most part of the velocity fields, except for some limited regions of separated flow, where very low velocities and high fluctuations occur. Under the same assumptions, for the latter zones, the maximum uncertainty in the

estimate of the r.m.s. velocities is less than 5%.
Under rotating conditions, the error introduced by the image processing has to be taken into account as it affects the acquired data. In accordance with the analysis proposed by Armellini et al. [102], the velocity uncertainty has to be increased by 1% of U_b (Eq. 4.2). As far as concern Stereo-PIV measurements' accuracy, it has been quantified through a cross comparison with the 2D PIV data in both static and rotating conditions. For more details, please refer to Furlani et al. [99].

2.9 Test setting and post-processing

The whole rig apparatus described above is aimed at measuring heat transfer coefficient through experimental tests, which need to be performed by following a precise procedure and in well defined thermal and fluid dynamic conditions. In the following sections, experimental conditions, methods and data analysis features will be presented.

2.9.1 Test conditions

The main objective of PRIN INSIDE project is the study of the effects of rotating conditions on the heat transfer performances of a impingement cooling system of a high pressure gas turbine blade leading edge. Moreover, the effect of several other characteristic parameters have been investigated during this work.

Since the model is realized to achieve similitude in terms of jet Reynolds number with respect to the real system, test conditions have been defined as target values of such parameter: in particular, Re_j nominal values of 10 000, 20 000, 30 000 and 40 000 have been replicated by suitably adjusting the mass flow across the rig. leading edge surface and extraction holes distribution (number, location, angle). The jet Reynolds number is defined as follow:

$$Re_j = \frac{U_j \cdot D_h \cdot \rho}{\mu} \tag{2.9}$$

where U_j is the tangential velocity of the jet and D_h is the hydraulic diameter of the impingement hole.

Test specification also requested the study of the cooling system over the whole blade span (the model represent just a portion of a real blade), i.e. for different ratios between crossflow and impingement mass flow rates: in fact, the mass flow through the feeding channel decreases along its radial extension, as a consequence of the impingement holes. To replicate this phenomenon and in analogy with ERICKA UNIFI tests [57], three tests have been performed for each Re_j value and mass flow extraction configuration, mimicking hub, mid and tip sections of the blade. In such way, a test scheme alike the one depicted in figure 2.10 is achieved, with tests performed with crossflow fractions (CR) of 70%, 40% and 10%. Crossflow conditions are set by operating the gate valve located downstream of the feeding channel.

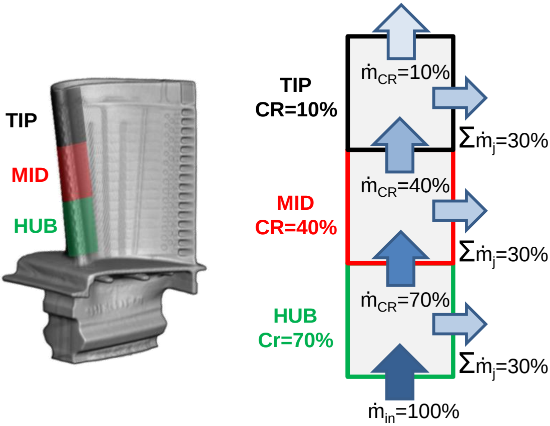

Figure 2.10: Cross-flow scheme

A distinctive feature of ERICKA tests was the replication of external pressure distribution effects on the internal cooling system. PRIN tests retrieve this feature, thus setting a mass flow split between the four extraction holes rows: 10% of the total cooling mass flow rate is extracted by the film cooling pressure side row, 40% by the film cooling suction side row and 50% by the two showerhead rows. However, for the present tests a second, "uniform" mass flow split has been investigated, with 25% of the total cooling flow extracted by each film cooling row and 50% by the showerhead rows. The differences between the two configurations are highlighted in figure 2.11. This second set was needed to better highlight the effects of pressure and suction side on the impingement performances, but also and especially to distinct this effect from the consequences of rotation. Extraction flow split is achieved by driving the gate valves of the three extraction plenums.

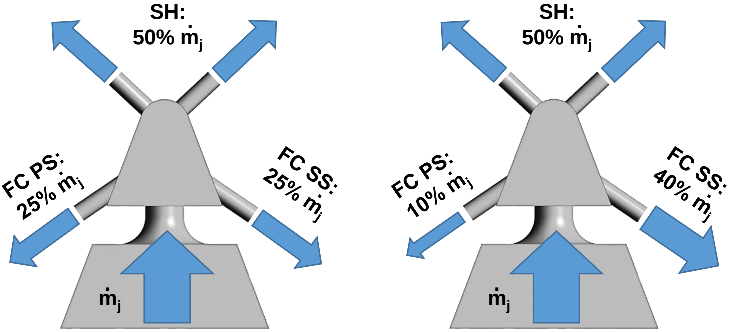

Figure 2.11: Spent coolant uniform (a) and non uniform (b) extraction.

Finally, in order to investigate the heat transfer distribution variations with the rotational speed, the aforementioned tests have been replicated in rotating conditions. Such tests have been performed varying the Rotation number (Ro) from 0 up to 0.05 (0.01-0.02-0.03-0.04-0.05) with the aim to reach actual engines working conditions; Ro is defined as:

$$Ro_j = \frac{\Omega \cdot D_h}{U_j} \tag{2.10}$$

where Ω is the rotational speed of the model, D_h is the hydraulic diameter of the impingement hole and U_j is the tangential velocity of the jet. Tests with $Re_j = 40000$ and $CR = 70\%$ have not been performed neither in static nor in rotating conditions in the present work, since the required mass flow would choke the measurement orifice located downstream the rig.

The performed test matrix of 64 points is summarized in table 2.1.

Table 2.1: Test matrix

$\mathbf{Ro_j}$	**CR 10**	**CR 40**	**CR 70**
0	Re_j 10k-40k	Re_j 10k-40k	Re_j 10k-30k
0.01	Re_j 10k-40k	Re_j 10k-40k	Re_j 10k-30k
0.02	Re_j 10k-40k	Re_j 10k-40k	Re_j 10k-30k
0.03	Re_j 10k-40k	Re_j 10k-40k	Re_j 10k-30k
0.04	Re_j 10k-40k	Re_j 10k-40k	Re_j 10k-30k
0.05	Re_j 10k-30k	Re_j 10k-30k	Re_j 10k-30k

All the requested test conditions (Re_j, CR and Ro) and all the measurement instrumentation are managed, monitored and controlled through a personal computer by means of a dedicated LabVIEW program. Such program allows to setup and manage jet Reynolds number and crossflow, and can provide the rotational speed needed to achieve a desired Rotation number value. A different personal computer takes care of image acquisition.

2.9.2 Data post processing

The data acquired during the test need to be elaborated to extract the heat transfer distribution, which is achieved through a complex post processing operation. Given the heat exchange coefficient formulation of equation 2.1, the values of $\dot{q}_{joule}$ and $\dot{q}_{lost}$ are needed for its calculation, as well as wall and air temperatures. As already mentioned, the coolant is ambient air and its temperature can be monitored using T-type thermocouples, while T_S is measured with TLC using the steady-state technique. At the end of the test, three images of different sections of the measurement surface (PS, LE, SS) from the cameras are available, which need to be joined together. A dedicated MATLAB® macro firstly aligns and crops each image; then, it extracts the hue distribution from each image and associates to it a temperature distribution, thanks to the calibration curve of each camera. The same macro also performs a curvature correction for the leading edge distribution, maps the images on the effective model geometry and finally joins them together, thus providing a unique temperature distribution map for the whole measurement surface.

Considering the complexity of the LE geometry and the presence of shower-head and film-cooling holes, it was not possible to assume a constant Joule heat flux distribution on the whole surface. For this reason a thermo-electric FEM simulation of the real model was carried out using the commercial code ANSYS Mechanical APDL v15 in order to evaluate the imposed heat flux; the model geometry was rolled out and meshed with around 10^5 *SOLID226* 20-node brick elements, specifically designed for the simulation of thermal-electric phenomena. After the imposition of a realistic set of boundary conditions to the model (in terms of both voltage drop across the Inconel sheet and heat transfer coefficient on every surface), such simulation allows to achieve the heat flux $(\dot{q}_{joule} - \dot{q}_{lost})$ on the target surface and to consequently update the HTC distribution thanks to the equation 2.1.

The computational model is composed by two layers: the inconel sheet on the inner side and the PMMA on the outer one, and the appropriate material properties (thermal and electric conductivity) have been attributed to the two zones. For the holes, a convective heat transfer coefficient is defined using the Colburn equation, which provides the Nusselt number value for completely developed turbulent flow in smooth tubes [106]:

$$Nu = 0.023\, Re^{0.8}\, Pr^{1/3} \tag{2.11}$$

In such way, the heat sink effect of the extraction holes has been taken into account. Concerning the outer PMMA surface, the model has been approximated as an horizontal cylinder where a constant h value, derived from the mean value of Nusselt number Nu_m calculated by means of

Wilks correlation [107], is imposed:

$$Nu_m = 0.579 \left(\frac{Gr_D Pr}{[1 + (0.442/Pr)^{9/16}]^{16/9}} \right)^{1/4} \tag{2.12}$$

where Gr_D is the Grashof number calculated with the model equivalent diameter, obtained by considering the external surface smaller dimension as a half circumference. Finally, in the inner surface a suitable heat transfer coefficient distribution has to be imposed by means of an array parameter; as it is also the output of the present post-processing procedure it is necessary to develop an iterative calculation, which will be presented in this section. All the other surfaces are considered adiabatic, which introduces little approximation since PMMA material completely surrounds the modeled section. The presence of the inconel layer allows to apply the electrical load through the simple imposition of the voltage drop measured during experimental test, which is directly set for the nodes at the foil extremities. A scheme of the boundary conditions is depicted in figure 2.12. As aforementioned, a boundary condition for the simulation is the convective heat transfer coefficient on the inner surface, which is the objective of the investigation itself, thus an iterative procedure is necessary to approach the solution. The scheme of such procedure is

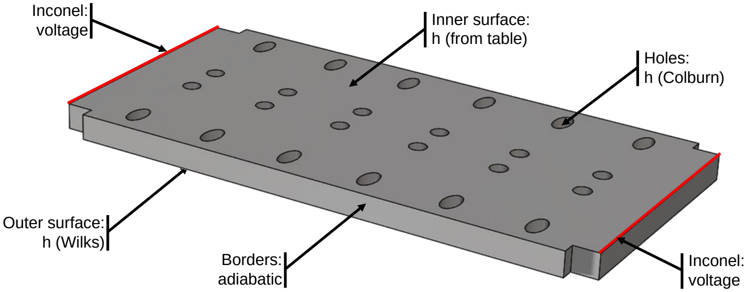

Figure 2.12: Boundary conditions for the FEM analysis.

presented in figure 2.13.

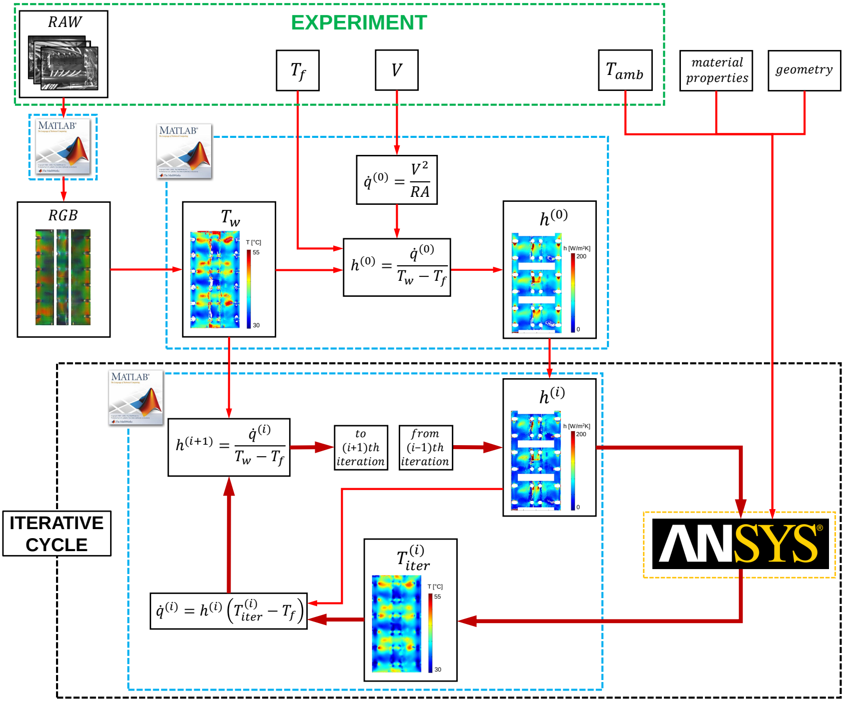

Figure 2.13: Scheme of the post processing procedure.

The same MATLAB® macro used to extract the wall temperature distribution also performs a first estimation of the heat transfer coefficient ($h^{(0)}$). For such calculation, flow and wall temperature are the measured ones, while the heat losses through the PMMA are neglected and the heat flux is calculated as a constant mean value, given by:

$$\dot{q}^{(0)} = \frac{V^2}{R_{foil} A_{foil}} \tag{2.13}$$

where V is the measured voltage and R_{foil} is the mean inconel resistance (which has been found to be constant across the experiments). An attempt distribution of h is thus calculated from equation 2.1, and is imposed as the inner boundary condition for the FEM analysis, thus entering the iterative cycle. The result of such analysis is a temperature distribution on the inner side of the model (T_{iter}), which is used to calculate a new value of the net heat flux $\dot{q}$ using the attempt h map. The obtained distribution of $\dot{q}$, together with the "real" measured temperature values, allows to calculate a refined map of h, which can again be imposed as boundary condition for the FEM, and so on. The relative difference between the measured and the calculated values of the wall temperature is used for error evaluation and thus for cycle convergence check, together with the variation of h between the iterations.

The whole iterative cycle is performed through a single MATLAB® macro, including calculations, values interpolation, automatic ANSYS® execution and outcomes management. The final results are provided in terms of Nu values, calculated from h through the equation 4.1. Such post-processing procedure have to be repeated for every experiment.

Chapter 3

Numerical modeling

The experimental campaign of the present test case has been accompanied by a parallel computational analysis. Such numerical investigation was aimed to assess the suitability of CFD approach at studying the physical phenomena involved into the internal cooling system of the leading edge of a rotating gas turbine blade. The results of the numerical analysis have been firstly compared with the experimantal ones, in order to validate the model both in static and in rotating conditions; this allow to develop a suitable numerical approach to study this and similar cases in different fluid dynamic conditions or varying some geometrical features. Then, such results have been exploited to deepen the comprehension of the investigated issue. In particular, the computational results were useful to better understand the flow field development into the internal cooling system and the presence of certain instabilities and non-stationary recirculating zone arising into the model, which allow to explain the heat transfer distribution along the leading edge target surface.

Firstly, this chapter focuses on computational fluid dynamic and turbulence modeling, with particular attention to the numerical tools used in this work. Then, a detailed overview of the numerical setup adopted for all the models exploited during such investigation are reported.

3.1 Computational Fluid Dynamics

The experimental investigation of heat transfer and fluid flow phenomena, represents the only way to obtain reliable informations about physical processes, by means of direct measurement of characteristic physical quantities. However, such an approach presents objective difficulties and limitations: tests on full scale equipment are often too expensive or impossible, and even an investigation on a scaled model of the system, like the ones presented above, does not allow to obtain a complete comprehension of the physical processes. Moreover, measurement instruments allow to record only a limited number of variables in a finite number of locations, and experimental uncertainty has to be considered too, since it reduces the confidence in measured quantities.
Such problems could be avoided if the basic physical principles governing the system could be expressed in a mathematical notation and solved: this would allow to obtain a theoretical model of the phenomenon able to suitably represent its behavior in any location and time. The aim of Computational Fluid Dynamics (CFD) is to employ such model and elaborate a method to solve it, with the goal of fully comprehend the physical phenomenon by solving its governing equations through computational resources. In fact, computer analysis offers several advantages with respect to experimental investigation:

- (generally) lower costs and higher speeds;
- availability of complete and detailed informations;
- high flexibility in setting different geometries and conditions;
- capability of simulating both realistic and ideal phenomena.

At the same time, numerical calculations are not free from disadvantages:

- it can happen that a suitable mathematical model for the phenomenon could not be found;
- it is possible for predictions with a limited objective on complex geometries not to be cheaper than experiments;

- the solution of extremely fast and small scale phenomena may require computational resources far beyond the capability of present day computers.

Moreover, the principal limit of CFD is that computational results need to be validated through experimental measurements, which is an essential step to assume the adequateness of the mathematical model to the physical one. For these reasons, in order to obtain wide and reliable predictions the computational and experimental studies have to coexist and interact: the validity of the first can be stated only through the second, and the experimental results interpretation can be helped by the detailed flow field knowledge achieved through a computational study.
As written above, any numerical method is based on a *mathematical model* of the phenomenon: fluid dynamic theory states that the behavior of any flow can be completely described through a set of partial differential equations expressing the basic conservation laws. Such set of equations cannot generally be solved in a closed form except for extremely simple geometries, boundary conditions and flow fields, and its application to engineering interest cases cannot be performed by means of a pure analytical study. A *discretization method* is therefore required, approximating the set of differential equations by a system of algebraic equations for the variables at a finite number of points in space and time. The discrete locations where the variables are calculated are defined by the *numerical grid*, a discrete representation of the fluid domain. The necessity to obtain a set of algebraic equations requires every feature present in differential equation to be expressed through the discrete values of the variables: such goal is obtained through the application of a suitable *finite approximation* technique. Once this large system of non-linear algebraic equations has been built, it can be solved by means of a suitable *solution method*, which usually performs successive linearizations of the equations and solves the resulting system through direct or iterative techniques. To obtain an accurate solution in an efficient way, the definition of a suitable *convergence criteria* is essential, since it permits to stop the calculation when the numerical set of values adequately approximates the solution of

the analytical problem.
Given its importance, the mathematical modeling of fluid mechanics is presented in the following section; a more in-depth analysis of the various aspects of a numerical method can be found in [108], [109].

3.1.1 Mathematical model

A representation of the behavior of any fluid can be obtained by expressing the basic conservation laws of physics in a mathematical form. In particular, the macroscopic behavior of an homogeneous continuum fluid can be suitably represented through the conservation equations of mass, momentum and energy, which altogether constitute the Navier-Stokes equations.

Continuity equation The mass balance for an infinitesimal control volume implies that the rate of increase of mass in the element must equal the net rate of mass flow through the element, and can be mathematically expressed by the relation:

$$\frac{\partial \rho}{\partial t} + \frac{\partial (\rho U_j)}{\partial x_j} = 0, \tag{3.1}$$

where ρ is the fluid density and U_j the velocity component in x_j Cartesian direction; as in the following, the repeated index notation indicates summation.

Momentum equation The momentum equation directly follows from Newton's second law: the rate of increase of momentum of fluid particle equals the sum of applied (surface and body) forces. The application of such principle to an infinitesimal control volume for each Cartesian direction leads to the following set of relations:

$$\frac{\partial (\rho U_i)}{\partial t} + \frac{\partial (\rho U_i U_j)}{\partial x_j} = -\frac{\partial p}{\partial x_i} + \frac{\partial \tau_{ij}}{\partial x_j} + F_{Mi}, \qquad i = 1, 2, 3, \tag{3.2}$$

where p and τ_{ij} represent pressure ad viscous stress components respectively (i.e. the hydrostatic and deviatoric part of the stress tensor) and

F_{Mi} is a source term including the overall effect of body forces on i-momentum.

Energy equation The energy equation follows from the first principle of thermodynamics, stating that the rate of change of energy in a fluid particle is equal to the rate of heat addition to the particle plus the rate of work done on the particle. The application of such conservation principle to an infinitesimal control volume allows to obtain the energy equation. For compressible flows can be expressed in a suitable form by considering specific total enthalpy as the conserved quantity:

$$h_0 = i + \frac{p}{\rho} + \frac{1}{2}(u^2 + v^2 + w^2), \tag{3.3}$$

where i is the fluid internal (thermal) energy and $\frac{1}{2}(u^2+v^2+w^2)$ represents the specific kinetic energy. With such assumption, the energy conservation equation takes the form:

$$\frac{\partial(\rho h_0)}{\partial t} + \frac{\partial(\rho h_0 U_j)}{\partial x_j} = \frac{\partial p}{\partial t} + \frac{\partial}{\partial x_j}\left(\lambda \frac{\partial T}{\partial x_j}\right) + \Phi + F_h, \tag{3.4}$$

where λ is the fluid thermal conductivity, $\Phi = \frac{\partial \tau_{ij} U_i}{\partial x_j}$ is the viscous dissipation and F_h is a term taking into account energy sources (energy generation, changes in potential energy or other modeled energetic interactions).

Fluid model Other relations are required to mathematically close the system constituted by equations 3.1, 3.2 and 3.4. Such relations can be obtained from the definition of a fluid model suitable for the investigated phenomenon. Usually, the fluid is assumed to be a *perfect gas* in thermodynamic equilibrium, thus the following equations of state can be defined:

$$p = \rho R T, \tag{3.5}$$

$$i = c_v T, \tag{3.6}$$

where R is the specific gas constant and c_v the specific heat at constant volume:. These relations allow to express static pressure p and internal energy i as functions of ρ and T, thus reducing the unknowns number in the previous set of equations.
Other unknowns include the viscous stress components τ_{ij}, which are usually modeled through the assumption of *Newtonian fluid*:

$$\tau_{ij} = \mu \left(\frac{\partial U_i}{\partial x_j} + \frac{\partial U_j}{\partial x_i} \right) + \delta_{ij} - \frac{2}{3}\mu \left(\nabla \cdot \vec{U} \right). \tag{3.7}$$

where μ is the fluid dynamic viscosity.

General transport equation Noticing the commonalities between the forms of the equations 3.1, 3.2 and 3.4, analogue terms can be identified in each of these equations, and thus a general differential form of the conservation equation can be written:

$$\underbrace{\frac{\partial(\rho\phi)}{\partial t}}_{\text{Rate of change}} + \underbrace{\frac{\partial(\rho\phi U_j)}{\partial x_j}}_{\text{Convection}} = \underbrace{\frac{\partial}{\partial x_j}\left(\Gamma \frac{\partial \phi}{\partial x_j}\right)}_{\text{Diffusion}} + \underbrace{F_\phi}_{\text{Source}} . \tag{3.8}$$

where ϕ is a general scalar variable.

3.2 Turbulence modeling

Almost every flow encountered in engineering practice, including the cases analyzed in the present work, are turbulent in nature. In these cases, the physics of fluid motion becomes extremely various, with a continuous development and destruction of three-dimensional flow structures on a wide range of length and time scales. Such behavior is very challenging in terms of fluid analysis and simulation, since the computational resources required for a complete solution of engineering interest cases are far beyond the ones available at the present day. Such issue can be handled with various approaches, the most interesting of which will be presented in the present section.

3.2.1 Nature of turbulence

The state of motion of a fluid flow is strictly dependent upon the intrinsic forces which develop within. Usually, the main forces present in flows of engineering interest are inertia forces (associated with convective effects) and viscous forces: it is then common practice to relate the state of motion of such flows with the Reynolds number, expressing the relative importance of inertia and viscous forces:

$$Re = \frac{UL}{\nu}, \tag{3.9}$$

where U and L are characteristic velocity and length scales of the mean flow and ν is the kinematic viscosity. For low Reynolds numbers, the flow regime is *laminar*, which means that the flow is smooth and adjacent layers of fluid slide past each other in an orderly fashion. In such case, the flow field is steady if the boundary conditions are constant. However, if Reynolds number is increased above a critical value (Re_{crit}), a radical transition in the flow character takes place: the flow behavior becomes intrinsically random, chaotic and unsteady even with constant boundary conditions, and its regime is thus said to be *turbulent*. Turbulence is a phenomenon presenting the following features [109]:

- **Unsteadyness** - variable values are not constant in time, but they can be decomposed as the sum of a time constant mean value and a fluctuation: $\phi(t) = \overline{\phi} + \phi'(t)$.

- **Tridimensionality** - even if flow can be described as one or two dimensional, fluctuations always occur in three dimensions.

- **Vorticity** - coherent vorticity flow structures, named *eddies*, appear and develop over the whole fluid domain;

- **Wide range of scales** - turbulent eddies present different length, velocity and time scales, which coexist at the same time and location.

- **Randomness** - even if a deterministic description of eddies behavior can be given, their appearance takes place in random locations. A model for turbulence can neither be completely deterministic nor totally statistic.

- **Self sustainability** - larger eddies (*energy carrying range*) extract kinetic energy directly from the mean fluid motion, and then handle it down to smaller eddies originating from their disintegration. Such energy transfer from larger to smaller scales, named *energy cascade*, takes place for a wide range of scales without appreciable energy production or dissipation (*inertial subrange*). When energy reaches the smallest eddies (*dissipation range*), whose characteristic Reynolds number Re_η (based on characteristic velocity v and characteristic length η) is equal to 1, viscous forces become predominant and dissipate the turbulent kinetic energy into heat.

- **Continuity** - smallest eddies length scale η, named *Kolmogorov scale*, is way bigger than any molecular scale.

- **Mixing** - the three-dimensional fluid flow activates convective transport in directions perpendicular to the mean flow, increasing mixing and heat exchange.

3.2.2 Numerical approach to turbulence

The above mentioned characteristics of turbulent regime result in an extremely complex fluid flow field, that in turn exponentially increases the computational cost of its numerical simulation. The governing equations of turbulent flows are still the Navier-Stokes equations in their general form, thus the general numerical method presented in section 3.1 is still valid for their solution. The greater complexity arises from the wide range of time and length scales of the turbulent eddies, which result in an equally wide range of scales to be computed and solved. As a consequence, even if Navier-Stokes equations include every information required for the simulation of a turbulent flow, the extraction of these information through direct solution of the equations is in general extremely costly and difficult [109]. To overtake this issue, all or a part of the turbulent behavior can be accounted through analytical models, which reduce the number of flow structures needing a direct solution. The various computational approaches to turbulence are distinguished by the amount of scales solved and modeled:

- **Direct Numerical Simulation (DNS)** - such approach involves no modeling, and the complete spectrum of time and length scales is solved. To perform such kind of analysis, mesh size and computational time step have to be as small as the Kolmogorov characteristic length η and characteristic time τ respectively, extremely increasing the computational cost. As a consequence, at present day DNS is not feasible for engineering practice flows, where phenomena lengths and times are way bigger than the smallest scales ones, and its application is limited to low Reynolds flows. DNS is however a useful tool to validate other approaches or to deepen the understanding of turbulence physics.

- **Large Eddy Simulation (LES)** - such approach is based on a direct solution of the largest turbulence scales (energy carrying range), while the smallest scales are modeled. In fact, small scales are isotropic and their behavior is universal, thus their effects on larger scale flow structures can be suitably accounted through a numerical model, while larger and anisotropic scales are solved. The separation between resolved and modeled scales is achieved through the application of a high-pass filter to the Navier-Stokes equations. Such filter is a local spatial mean of the variables, calculated on a local length, so that all flow structures lying below such dimension are filtered and modeled. Even so, the computational cost of a LES simulation is still high, in particular for wall-bounded flows. However, the accuracy in the prediction of flow behavior and the increase in the available computational resources are expanding LES application field, especially where turbulent phenomena play a major role (combustion, aeroacoustic).

- **Reynolds Averaged Navier Stokes (RANS)** - such approach completely neglects the whole turbulence spectrum, since it only accounts for turbulent unsteadiness through its steady effect on the mean flow. To achieve this goal, Navier-Stokes equations are averaged in time on a period long enough to include all turbulence frequencies. This allows RANS to exclusively solve the steady structures, drastically reducing computational cost while maintaining a good accuracy in the prediction of the mean flow: as a consequence, RANS is nowadays the most widely used approach for CFD simulations, both in industrial and in scientific applications.

- **Hybrid models** - the idea behind such approaches is to overtake the disadvantages of both LES and RANS through the application of each model in the flow region where there are more suitable. In particular, these models behave like RANS in the zones where the application of LES would result extremely costly or inadequate (e.g. near the solid boundaries) and present a LES-like solution where RANS would not be adequate, as in separated or strongly unsteady flows. The moderate computational cost, the improved accuracy and the relative ease of application make Hybrid Models extremely interesting for a wide range of applications. Such approaches include the various formulations of Detached Eddy Simulation (DES) and Scale Adaptive Simulation (SAS).

Since the numerical simulations presented in this work have been performed using RANS, SAS and DES turbulence models, these approaches will be presented in detail in the following sections.

3.2.3 RANS models

As already stated above, RANS approach consists in an averaging of Navier-Stokes equations over time. To perform this operation, the definition of Reynolds Averaging can be applied:

$$\overline{f}(x) = \lim_{\Delta t \to \infty} \frac{1}{\Delta t} \int_{t}^{t+\Delta t} f(x,\tau)\, d\tau. \tag{3.10}$$

The application of such definition to a generic variable ϕ allows its decomposition in an average value $\overline{\phi}$ and in a fluctuating value ϕ': $\phi = \overline{\phi} + \phi'$. Considering Reynolds operator properties, the application of Eq. 3.10 to the instantaneous value of a fluid property causes the disappearance of its fluctuating part:

$$\overline{\phi} = \overline{\overline{\phi} + \phi'} = \overline{\overline{\phi}} + \overline{\phi'}, \qquad \overline{\overline{\phi}} = \overline{\phi}, \qquad \overline{\phi'} = 0. \tag{3.11}$$

However, if the averaging is applied to the product of two generic time-dependent variables ϕ and ψ, the contribution of the fluctuations is not removed; in fact, the application of Reynolds averaging properties leads to:

$$\overline{\phi\psi} = \overline{(\overline{\phi} + \phi')(\overline{\psi} + \psi')} = \overline{\overline{\phi}\,\overline{\psi}} + \overline{\overline{\phi}\psi'} + \overline{\phi'\overline{\psi}} + \overline{\phi'\psi'} = \overline{\phi}\,\overline{\psi} + \overline{\phi'\psi'}. \tag{3.12}$$

For compressible flows, the definition of density-weighted Favre averaging is also useful:

$$\tilde{f}(x) = \lim_{\Delta t \to \infty} \frac{1}{\overline{\rho}\Delta t} \int_t^{t+\Delta t} \rho f(x,\tau)\, d\tau = \frac{\overline{\rho f(x)}}{\overline{\rho}}, \tag{3.13}$$

which, in turn, allows the decomposition $\phi = \tilde{\phi} + \phi''$. Favre averaging usefulness for the derivation of RANS equations derives from the exact verification of the simplification [109]:

$$\overline{\rho U_i U_j} = \overline{\rho}\tilde{U}_i\tilde{U}_j + \overline{\rho U_i'' U_j''}. \tag{3.14}$$

Keeping in mind the previous statements, the application of time averaging to the Navier-Stokes equations in their general form 3.1, 3.2 and 3.4 leads to [109]:

$$\frac{\partial\overline{\rho}}{\partial t} + \frac{\partial(\overline{\rho}\tilde{U}_j)}{\partial x_j} = 0, \tag{3.15}$$

$$\begin{aligned}
&\frac{\partial(\overline{\rho}\tilde{U}_i)}{\partial t}+\frac{\partial(\overline{\rho}\tilde{U}_i\tilde{U}_j)}{\partial x_j}+\frac{\partial(\overline{\rho U_i''U_j''})}{\partial x_j}\\
&=-\frac{\partial\overline{p}}{\partial x_i}+\frac{\partial}{\partial x_j}\left[\mu\left(\frac{\partial\overline{U_i}}{\partial x_j}+\frac{\partial\overline{U_j}}{\partial x_i}\right)-\frac{2}{3}\mu\delta_{ij}\frac{\partial\overline{U_j}}{\partial x_j}\right]+\overline{F_{Mi}},\qquad i=1,2,3,
\end{aligned}\tag{3.16}$$

$$\frac{\partial(\overline{\rho}\tilde{h_0})}{\partial t}+\frac{\partial(\overline{\rho}\tilde{h_0}\tilde{U_j})}{\partial x_j}+\frac{\partial(\overline{\rho h_0''U_j''})}{\partial x_j}=\frac{\partial\overline{p}}{\partial t}+\frac{\partial}{\partial x_j}\left(\lambda\frac{\partial\overline{T}}{\partial x_j}\right)+\overline{\Phi}+\overline{F_h},\tag{3.17}$$

In such way, the so called unsteady time averaged transport equations are obtained, in which time dependency of the average values is included. Such form of the conservation equation is applied in the URANS (Unsteady RANS) models, in which time averaging operation is performed on a time interval Δt bigger than the time scale of the largest eddies, thus leveling all the turbulent fluctuations, but still smaller than the time period of unsteady flow structures of different nature. URANS models are thus able to appreciate the effects of global unsteadiness even if a time averaging operation is performed. If the physics of the phenomenon leads to steady flow field, time dependency can be ignored, thus reducing the complexity of the equations and the computational cost of their solution: this can be obtained by imposing Δt to tend to infinity, which implies all time derivatives to become zero. The resulting equations are the the steady RANS equations, and are suitable for every flow not presenting macroscopic unsteady behavior.

As it can be seen, the form of the Reynolds averaged equations 3.15, 3.16 and 3.17 is similar to their general form, but the nonlinearity of convective terms in momentum and energy equations causes a new term for each equation to appear, depending on fluctuating quantities. Such terms depend upon the fluctuations which the time averaging operation is intended to remove, thus they are unknown in this particular approach. As a consequence, their contribution needs to be modeled. As will be presented soon, such modeling permits to reformulate these convective terms as diffusive ones, thus they are moved to the right hand side of the equations and are assimilated to the viscous and conduction term respectively: that is why the tensor $\overline{\rho U_i'' U_j''}$ is called *Reynolds stress tensor* and the vector $\overline{\rho h_0'' U_j''}$ is called *turbulent heat flux*. These terms introduce 9 unknowns in the averaged Navier-Stokes equations, thus the system is undetermined again: a mathematical closure of the equation set is then needed for it to be solved, and can be obtained by expressing the newborn terms as a function of the variables related to the mean flow. The ensemble of relations that can be defined to relate mean and fluctuating quantities embodies the *turbulence model*.

Amongst all kinds of approaches to turbulence, the most widely used in industrial and engineering practice are the *Eddy Viscosity Models*. Such models are based on the Boussinesq hypothesis, which sets an analogy between macroscopic turbulent eddies and microscopic molecular behaviors [110]: so, as momentum transfer caused by the latter is defined by the dynamic viscosity μ, the effect of eddies on the mean flow can be described through an additional *turbulent* or *eddy viscosity* μ_t. Such parameter allows to relate the Reynolds stress tensor with strain rate or, equivalently, with velocity gradients:

$$-\overline{\rho U_i'' U_j''} = \mu_t \left(\frac{\partial \overline{U_i}}{\partial x_j} + \frac{\partial \overline{U_j}}{\partial x_i} - \frac{2}{3} \delta_{ij} \frac{\partial \overline{U_k}}{\partial x_k} \right) - \frac{2}{3} \rho k \delta_{ij}, \tag{3.18}$$

where k is the mean turbulent kinetic energy: $k = \frac{1}{2} \overline{U_k' U_k'}$. The last term containing k is required by the definition of k itself, which forces the trace of the Reynolds stress tensor to be equal to $2k$ [108]. The closure problem is then simply reduced to an evaluation of the eddy viscosity μ_t, hence the name of such class of models. The main advantage of this approach is its ease of implementation, which exclusively consist in the replacement of μ with an effective viscosity $\mu_{eff} = \mu + \mu_t$. A similar procedure can be applied to the energy equation too, where the effect of turbulence can be accounted through the definition of a turbulent thermal diffusivity a_t and the substitution of the thermal diffusivity $a = \lambda / \rho c$ with an effective value $a_{eff} = a + a_t$.

Eddy Viscosity models can be further classified depending on the number of transport equations solved to compute turbulent viscosity: in fact, mirroring the definition of molecular viscosity as the product the free path and the mean velocity of a molecule, μ_t can be defined as the product of a turbulent length scale and a turbulent velocity scale:

$$\mu_t \propto \; l^* \; u^*. \tag{3.19}$$

Up to two additional transport equation can be defined to derive l^* and u^*, which allow to distinguish different classes of turbulence models: *Algebraic Models* or zero equation models derive l^* and u^* from mean flow and geometry respectively, without solving additional transport equations; *One Equation Models* still use the length scale but solve an additional transport differential equation for the turbulent kinetic energy k, bound to the velocity scale; *Two Equation Models* specify two additional transport equations for both k and its rate of dissipation (absolute ϵ or specific ω). Given their more physical predictions, two equation models have become a standard for industry and engineering computations.

The landmark model for the eddy viscosity two equation models is the standard $k - \epsilon$ model. It implies the solution of two additional transport equation for turbulent kinetic energy k and its dissipation rate ϵ, whose necessity arises from the expression of length scale l^* and velocity scale u^* as a function of such parameters:

$$l^* \propto k^{3/2}/\epsilon, \qquad u^* \propto k^{1/2}, \tag{3.20}$$

which allow to derive eddy viscosity μ_t from k and ϵ:

$$\mu_t = C_\mu \; \overline{\rho} \; u^* \; l^* = C_\mu \; \overline{\rho} \; k^{1/2} \; k^{3/2}/\epsilon = C_\mu \; \overline{\rho} \; k^2/\epsilon, \tag{3.21}$$

where C_μ is a constant. A transport equation for k can be directly derived from Navier-Stokes equations [109]:

$$\frac{\partial(\rho k)}{\partial t} + \frac{\partial(\rho k U_j)}{\partial x_j} - \frac{\partial}{\partial x_j}\left[\left(\mu + \frac{\mu_t}{\sigma_k}\right)\frac{\partial k}{\partial x_j}\right] = P_k - \rho\epsilon, \tag{3.22}$$

It can be observed that the diffusion coefficient in Eq. 3.22 is obtained from the sum of dynamic and eddy viscosity, where the latter is divided by a coefficient σ_k named Turbulent Prandtl Number whose value is usually close to unity. The source term is split into a proper production term P_k and a sink term $-\rho\epsilon$, which contains the turbulent kinetic energy dissipation ϵ. A second transport equation can be defined to obtain ϵ:

$$\frac{\partial(\rho\epsilon)}{\partial t} + \frac{\partial(\rho\epsilon U_j)}{\partial x_j} - \frac{\partial}{\partial x_j}\left[\left(\mu + \frac{\mu_t}{\sigma_\epsilon}\right)\frac{\partial\epsilon}{\partial x_j}\right] = C_{\epsilon 1}P_k\frac{\epsilon}{k} - \rho C_{\epsilon 2}\frac{\epsilon^2}{k}, \quad (3.23)$$

where $C_{\epsilon 1}$, $C_{\epsilon 2}$ and σ_ϵ are constants whose values are defined as a part of the modeling.

The k-ϵ model is one of the most widely applied turbulence models, as it includes reasonable turbulence physics at a moderate computational cost and has proven to be stable and numerically robust for a number of engineering interest cases. However, it suffers from many known disadvantages, as the inability to well predict swirled and adverse pressure gradient flows [111], thus failing to predict the onset and the amount of flow separation, and its nature of High-Reynolds model, which leads to the inability to correctly simulate near-wall turbulence damping [109]. Near wall behavior can be imposed through the use of Wall Functions or by a grid refinement and the inclusion of molecular viscosity effects in the model coefficients, leading to the so-called Low Reynolds approach.

A better solution of wall-bounded and adverse pressure flows can be obtained through the k-ω model, presented by Wilcox in 1998 [111]. Such model adopts as the second transported turbulent parameter the specific dissipation of turbulent kinetic energy per unit volume and time, defined as:

$$\omega = \frac{\epsilon}{\beta^* k}, \quad (3.24)$$

where β^* is a model constant (usually set to $\beta^* = C_\mu$); this results in:

$$\mu_t = \overline{\rho}\,\frac{k}{\omega}. \quad (3.25)$$

The resulting scale equation can thus be written as:

$$\frac{\partial(\rho\omega)}{\partial t} + \frac{\partial(\rho\omega U_j)}{\partial x_j} - \frac{\partial}{\partial x_j}\left[\left(\mu + \frac{\mu_t}{\sigma_\omega}\right)\frac{\partial\omega}{\partial x_j}\right] = C_{\omega 1}P_k\frac{\omega}{k} - \rho C_{\omega 2}\omega^2. \quad (3.26)$$

The improved behavior of such approach in the critical regions for the k-ϵ model is counterbalanced by a strong sensitivity to freestream conditions: depending on the value specified for ω at the inlet, a significant variation in the results of the model can be obtained [112]. To solve such problem, a blending between k-ω model near the surface and the k-ϵ model in the freestream region was developed by Menter [112]. It consists of a transformation of the k-ϵ model to a k-ω formulation and of a subsequent addition of the corresponding equations, each multiplied by a blending function which selects the most suitable model for each flow region. The resulting hybrid model takes the name of Baseline (BSL) k-ω model.

Although BSL model combines the advantages of both k-ϵ and k-ω models, it still fails to properly predict the onset and amount of flow separation from smooth surfaces The main reason for this deficiency is that both k-ϵ and k-ω models do not account for the transport of turbulent shear stress, which results in an overprediction of the eddy viscosity in adverse pressure separated regions. To overcome this issue, the k-ω Shear Stress Transport (SST) was proposed by Menter [112]: the model is built upon BSL formulation and is based on Bradshaw's assumption that the principal shear stress is proportional to the turbulent kinetic energy, which is introduced into the definition of the eddy-viscosity; in the adverse pressure gradient regions, where such assumption should be violated, the proper transport behavior is obtained by a limiter to the formulation of the eddy-viscosity [109] [113]. The SST model is the most used and validated model for cases analogous to the one presented in this work [8], thus it has been adopted for the steady RANS simulations, as reported in the following paragraphs.

For an extensive review of these and other models, please refer to [108], [111].

3.2.4 Scale Resolving Simulations

While present day CFD simulations are mainly based on RANS turbulence models, certain classes of flows encountered in engineering practice are better covered by models in which all or a part of the turbulence spectrum is resolved in at least a part of the computational domain: this is particularly important when accuracy improvement for unsteady and highly-separated flows is needed, as well as when additional informations are required (like acoustics, fluid-structure unsteady interactions, vortex cavitation, etc) [15]. Such numerical methods are termed Scale-Resolving Simulation (SRS) models, and include both LES and hybrid RANS-LES models. Amongst these, LES has been the most widely used SRS model over the last decades: as shown in section 3.2.2, it is based on the concept of resolving only the large scales of turbulence and to model the small scales, relying on the universal and isotropic behavior of the latter ones. However, LES structure itself make it particularly demanding for to wall-bounded flows, which is a typical situation in engineering flows. In fact, the turbulent length scale l^* of the large eddies can be expressed as [15]:

$$l^* = \kappa y, \tag{3.27}$$

where y is the wall distance and κ is a constant. This relation implies that near the wall even the largest turbulent scales become relatively small and require high resolution in space and time in order to be solved. Equation 3.27 implies $l*$ to approach to zero near the wall: however, in reality this is not verified, as the molecular viscosity prevents scales smaller than the Kolmogorov limit. This causes the development of the *viscous* or *laminar sublayer* in the region closer to the wall, in which turbulence is damped and thus does not need to be resolved. However, the viscous sublayer thickness decreases as the flow Reynolds number increases: as a consequence, for high Re values the viscous sublayer becomes increasingly thinner and allows the survival of smaller and smaller eddies, which need to be resolved in a LES computation. Such situation, depicted in figure 3.1, makes wall-resolved LES prohibitively expensive even for moderate Re values. Another significant issue of LES application is the necessity of an accurate specification of the turbulent boundary conditions at the inlets [114], which are usually unknown. Such issues make LES not suitable for application to most engineering flows, despite its ability to provide details on turbulent flow structure which cannot be obtained form a RANS

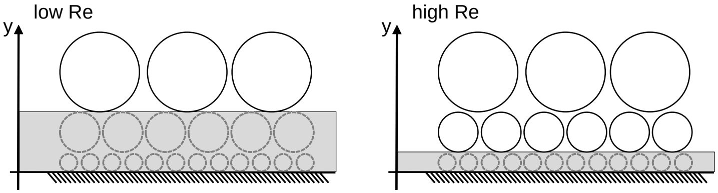

Figure 3.1: Sketch of turbulent structures (circles) for a wall-bounded flow and of their relation with viscous sublayer (grey area) for low (left) and high (right) Reynolds number [15].

formulation.

In an attempt to maintain the accuracy of LES in the wall distant regions, while limiting the simulation computational cost to an affordable level, hybrid RANS-LES models have been proposed. The aim is to limit the scale resolution only to those regions where instability occurs and to cover the remaining part of the domain with a RANS approach. In fact, it is possible to combine RANS and LES models thanks to the formulation of the filtered momentum equation itself: both approaches in fact model the unresolved turbulence scales with an eddy viscosity, and thus the filtered equations can operate in RANS or LES mode according only to the size of such parameter provided by the turbulence model [15].

The most widely used hybrid RANS-LES approaches, as well as the ones tested in the present work, include the Detached Eddy Simulation (DES) and the Scale Adaptive Simulation (SAS), which will be briefly presented in the following sections.

3.2.4.1 Scale Adaptive Simulation

The Scale Adaptive Simulation (SAS) represents an improved URANS formulation, which allows the resolution of the turbulent spectrum in unstable flows. Such approach was first introduced by Menter and Egorov [115] and is based on the introduction of the von Karman length scale

L_{vK} into the turbulence scale equation:

$$L_{vK} = \kappa \left| \frac{\overline{U}'}{\overline{U}''} \right|, \quad \text{with} \quad \overline{U}' = \sqrt{\frac{\partial \overline{U}_i}{\partial x_j} \frac{\partial \overline{U}_j}{\partial x_i}} \quad \text{and} \quad \overline{U}'' = \sqrt{\frac{\partial^2 \overline{U}_i}{\partial x_j^2} \frac{\partial^2 \overline{U}_j}{\partial x_k^2}}, \tag{3.28}$$

where κ is a constant. As implied by its definition, the von Karman length scale includes the second velocity gradient, which is sensible to inhomogeneous and unstable velocity profiles. This property can thus be exploited to automatically identify the unstable regions, thus reducing eddy viscosity and switching to a LES-like behavior only when required by the flow physics. This behavior, which thus adapts the length scale to the resolved turbulent structures (hence the name of the model), can be implemented in any two equation RANS model through an appropriate modification of the scale defining equation. The SAS version included in ANSYS® CFX, developed in [116], is based on the robust k-ω SST model, and hence is named SST-SAS. The implementation of SAS into RANS model is simply achieved through the inclusion of an additional production term Q_{SAS} in the ω equation (Eq. 3.26), in which the quadratic ratio of turbulent length scale and von Karman scale $(l^*/L_{vK})^2$ is included. As noted in [117], von Karman length scale is smaller for an unsteady velocity profile than for a steady velocity profile, thus leading to an increase in l^*/L_{vK} ratio in unsteady regions which triggers on the production term: as a consequence, the production of ω is increased and the eddy viscosity $\mu_t = \overline{\rho}\, \frac{k}{\omega}$ (Eq. 3.25) is decreased [118].

A main advantage of the presented approach is that it has no effect on the SST model RANS performances in stable flow regions: as a consequence, as the RANS part of the model results unaffected by the grid spacing, and the issues related to Grid Induced Separation and to “gray zones” are avoided. Such robustness is a significant improvement over DES approach, and allows the use of SAS on a much wider range of numerical grids [119]. Such advantage is counterbalanced by the fact that the underlying turbulence model has to go unsteady in order for the SAS method to produce a resolved turbulent spectrum: SAS is not able to switch from a RANS to a

LES-like behavior in absence of large and unstable separation zones [15], and can thus produce a steady flow field even in the zones where a scale resolution is desired. Moreover, unlike DES, SAS cannot be forced to go unsteady by grid refinement [120]. This results in SAS methodology to be more suitable for globally unstable flows (e.g. flows past bluff bodies, with strong swirl instabilities or strong interactions) rather than for locally unstable ones (e.g. flows with localized separation zones) [15], even if the adequateness of the numerical method needs to be evaluated case by case. Considering the strong instability developed by the investigated case, which will be discussed in the following sections, the SAS approach was selected as one of the turbulence models applied in the present work, in consideration of its robustness and its increase in resolution with respect to URANS.

3.2.4.2 Detached Eddy Simulation

The idea at the basis of Detached Eddy Simulation (DES), firstly proposed by Spalart [121], is the possibility of covering the boundary layer with a RANS model and of automatically switch to LES mode in the detached regions of the flow. In such way, compared to classical LES methods, DES saves orders of magnitude of computing power for high Reynolds number flows [120]. The switch between the two approaches is based on the grid local dimension:

$$C_{DES}\Delta_{max} > l^* \quad \rightarrow \quad \text{RANS}$$

$$C_{DES}\Delta_{max} \leq l^* \quad \rightarrow \quad \text{LES}$$

where C_{DES} is a model constant, Δ_{max} is the maximum edge length of the local computational cell and l^* is the turbulence length scale calculated by RANS model. As a consequence, as the grid is refined below the limit l^*/C_{DES} the DES limiter is activated and switches from RANS to LES. This suggest that DES requires grid and time step to be LES quality in the resolved regions: however, the reduction in computing cost comes from the RANS treated near wall region, where the small value of l^* does

not trigger the switch.
The switch can be included in any two-equation eddy viscosity model by reformulating the destruction term in the k equation 3.22 as:

$$\epsilon = \beta^* k\omega \quad \rightarrow \quad \epsilon = \beta^* k\omega \cdot F_{DES}, \quad \text{with} \quad F_{DES} = max\left(\frac{l^*}{C_{DES}\Delta_{max}}, 1\right). \tag{3.29}$$

In the present work, the finite volume Navier-Stokes solver ANSYS® CFX has been used, which implements a DES formulation based on the k-ω SST model: such formulation has the advantage of accurately predict the turbulent boundary layers up to separation and to carry over from the SST model in midly separated regions [113].
One of the main issues of DES model is that there is no mechanism of preventing the limiter of becoming active in the attached portion of the boundary layer. This happens when the local grid spacing is less than the boundary layer thickness δ, and results in a premature unphysical flow separation, called Grid-Induced Separation (GIS) [122]. To prevent this issue, an option is to "protect" the boundary layer from the limiter. This results in a shielded formulation of DES, achieved in the version of SST DES of ANSYS® CFX thanks to the zonal formulation of SST model. The limiter is then expressed as:

$$F_{DES-CFX} = max\left(\frac{l^*}{C_{DES}\Delta_{max}} \cdot (1 - F_{SST}), 1\right), \quad \text{with} \quad F_{SST} = 0,\, F_1,\, F_2, \tag{3.30}$$

where F_1 and F_2 are the SST blending function. According to [120], this formulation would reduce the GIS problem by an order of magnitude, but still can't eliminate it entirely. Following the same shielding concept, a new version of DES model was developed by Spalart et al. [123], named Delayed DES (DDES), which involves a similar reformulation of the limiter:

$$F_{DES-Delayed} = max\left(\frac{l^*}{C_{DES}\Delta_{max}} \cdot (1 - F_{DDES}, 1\right). \tag{3.31}$$

The function F_{DDES} is designed in such a way to give $F_{DDES} = 1$ inside the wall boundary layer and $F_{DDES} = 0$ away from the wall, thus achieving a proper shielding, without suppressing the formation of resolved turbulence as the flow separates from the wall [15].
A second important issue of DES formulation is that for free shear flows (in which the shielding is not active) the limiter can be activated much before the grid is actually able to resolve the flow in LES quality. There can be even an order of magnitude in grid dimension between the activation of the limiter and a sufficient LES resolution: in between these values, the model is undefined and the solution will be neither RANS nor LES. In such "grey zones" the RANS model is impacted, but the development of an unsteady solution is still not allowed. As a consequence, great effort must be spent on order to provide the model an adequate grid resolution according to the desired RANS or LES behavior, which requires a preemptive knowledge of the model structure and of the fluid phenomenon. In spite of these issues, the possibility to trigger the scale resolution simply by grid refinement makes DES a suitable option for those flows exhibiting local unsteadiness. For this reason, DES has been selected as one of the numerical methods tested for the present work, as will be better pointed out in the following sections.

3.3 Numerical setup of computational investigations

The numerical setup of the CFD models adopted during the present computational campaign is here reported for both steady-state and unsteady simulations. The following sections will present the simplifications used to study the leading edge model geometry, the computational grid and finally a detailed overview of the adopted boundary conditions for both the over mentioned numerical analysis.

3.3.1 Steady state simulations (RANS)

Given the symmetry of the investigated geometry with respect to a radial plane, this configuration allows to suppose the whole flow field to be symmetric on a macroscopic scale, which permits to reduce the computational domain to only half the geometry. Starting from this supposition, the domain represented in figure 3.2 has been defined.

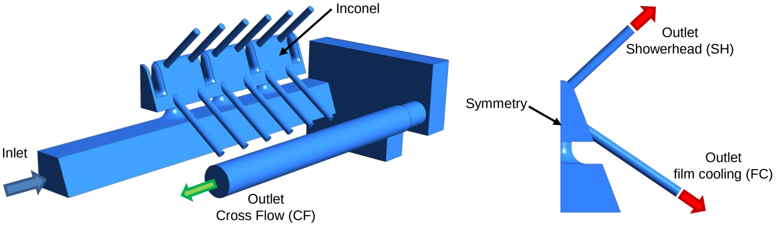

Figure 3.2: Computational domain for the uniform extraction case.

The computational domain includes the whole measurement section, and includes a length of inlet and outlet ducts that is sufficient to avoid influences on the interest region [94]. The effects of foam and honeycomb filters are accounted for: two porous subdomains have been defined, where additional source terms in the momentum equations are activated to consider the filter induced losses [94]. Depending on the configuration of the simulated test (hub or tip), such subdomains can be moved on the corresponding filter location (see section 2.4). Regarding extraction holes, a single outlet has been defined for each row: this configuration allows to easily simulate the presence of the downstream plenum. The length of the extraction ducts to be included has been determined to avoid flow recirculations at the outlet.

The domain is discretized by means of a suitable computational grid, which has been defined as unstructured given the complexity of the geometry. The mesh has been built using ANSYS® ICEM v15, and its characteristic dimensions are the result of a sensitivity analysis on both stability and accuracy of the simulations. Since impingement is an intrinsically unstable phenomenon (see section 1.5), it has not been easy to reach a converged solution exploiting a RANS approach. The use of increasingly refined grids in search of a greater accuracy have not always allowed to improve the resolution of the unstable structures that arise into the model, leading to some convergence issues. As a consequence, it has not been possible to follow a standard mesh sensitivity approach, and an accurate zone by zone crafting of the grid had to be performed. Such approach has the aim to obtain the best available resolution (with the most refined grid possible) into the most interesting zones (i.e. on the impingement surface), while granting the stability of the simulation and a converged solution. Following it, a mesh sensitivity analysis was performed (for the test case with a Re_j of 40000 and a CR of 70%) obtaining the computational grid used in the present work. Since the comparison of converged and diverged solutions do not add any relevant information to the dissertation, the results of such sensitivity are not reported here. Such approach is particularly valid for the impingement cavity, as in the other regions the higher flow stability has allowed to perform a simple mesh sensitivity analysis. By following this criterion, the grid represented in figure 3.3 is obtained, which presents density-induced refinement on the impingement target surface, and an increasing mesh size towards the center of the leading edge cavity.

The mesh is composed of around $6.1 \cdot 10^6$ elements, and is built as a hybrid grid using tetrahedral elements in the freestream regions and 20 layers of prisms in proximity of the physical walls: this allows both to accurately reproduce the geometry and to suitably describe the near wall gradients.
Simulations have been performed using the solver ANSYS® CFX v15. The boundary conditions have been set as follows. For all the solid walls the no slip wall condition has been used, and on the heater this setting has been combined with a constant heat flux condition (representing the presence of the inconel sheet). At the inlet, both a relative total pressure and a total temperature conditions have been set, together with a turbulence level of $Tu = 5\%$. Indeed, despite there is not a measure of inlet turbulence level, the assumption of uniform velocity and low turbulence represents a consistent hypothesis, especially thanks to the over mentioned two-layer sector (composed by an honeycomb and a foam

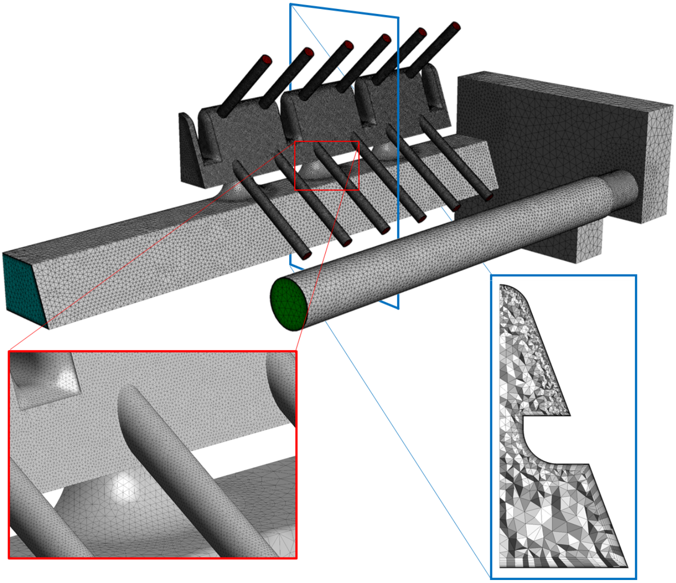

Figure 3.3: Numerical grid for the uniform extraction case, with a detailed and a cross-sectional views.

thickness) placed on the inlet region of the trapezoidal feeding duct. On the crossflow outlet a mass flow has been imposed, while on the outlets of showerhead and film cooling holes a condition of average static pressure has been chosen, which embodies a more physical behavior given the presence of the plenums; finally, the plane on which the complete geometry is cut has been supplied with a symmetry condition. It must be noticed that, as the test conditions are defined in terms of mass flow and not of pressure, a fine tuning of the pressure value at the extraction outlets had to be performed for each test, with the aim to recover the desired mass flow value. Moreover, it is important to remember that, since the simulations have been performed before the experiments, the actual values of fluid temperatures and heat fluxes could not be imposed: as a consequence, despite the known independence of heat transfer coefficient values from wall and fluid temperatures [124], some discrepancies between the numerical and experimental results could arise. The domain has been set as non buoyant: in fact, an estimation of the Grashof number revealed that the condition $Gr_j \ll Re_j^2$ is verified in any test condition, thus a purely forced convection is present.

Given the nature of the investigated phenomenon, and in agreement with the experiences found in literature [8] [40], turbulence has been modeled using a RANS k-ω SST model, given its good behavior in both freestream and near wall regions. Standart k-ϵ has also been considered, but its application resulted in a strong overestimation of Nu values.

The automatic near wall treatment approach has been chosen among the ones available in CFX. This model blends between wall functions and a low-Reynolds resolution on the basis of y^+ value, thus granting a robust approach while taking advantage of the local grid refinements. For the present case, y^+ value is below 1 in every point of the impingement target surface, thus the low-Reynolds formulation is recovered in such region.

The High Resolution discretization scheme, a Total Variation Diminishing-class algorithm [125], has been adopted as the finite approximation technique for the resolved equations, with the aim to improve the solution accuracy. Due to the aforementioned convergence issues resulting from the impingement phenomenon instabilities, the turbulence transport equations had to be solved using a First Order scheme, in the attempt to increase convergence stability. Since the usual convergence criteria could not be reached (residuals below 10^{-6} for all the equations), the solution was considered converged when all of the values of interest (monitored during the solution) reached a constant level and maintained it for at least 200 iterations, and when the residuals were below 10^{-4}. Despite all the adopted measures, a perfectly converged solution could not be achieved for all the tests: in such cases, converge was considered to be reached when a periodic oscillating behavior was shown and the amplitude of the oscillations was below 5% of the variable value.

3.3.2 Unsteady simulations (SAS and D-DES)

Even this set of simulations, carried out to simulate rotating condition and static tests with the non-uniform coolant extraction, has been performed using ANSYS® CFX v15 solver. The computational model, as shown in figure 3.4, has been defined with the same criteria of the symmetric extraction case, but including the complete geometry.

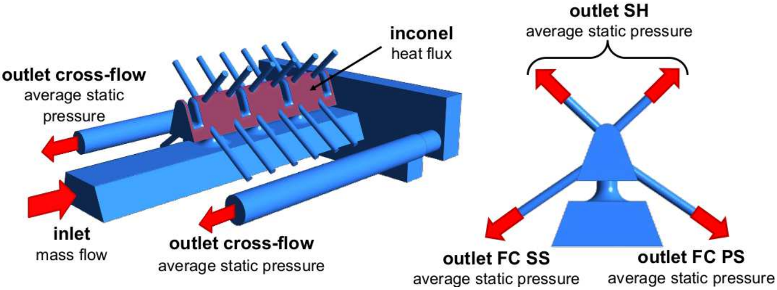

Figure 3.4: Computational domain for for unsteady simulations.

A suitable mesh (that can be depicted in figure 3.6) has been built using ANSYS® ICEM v15, following both the best practices drawn up by the code developers for Scale Resolving Simulations [15] and the experience acquired from the RANS simulations. In particular, a refined LES-quality grid has been built into the leading edge cavity, in order to trigger the DES limiter and thus activate the turbulence resolution. In the remaining part of the domain, a coarser, RANS-quality mesh has been defined, with the aim to reduce the computational cost of the simulation. The refinement level of the impingement cavity region has been derived from a sensitivity analysis, with the aim to achieve the best compromise between a sufficient scale resolution and a reasonable computational cost. This has been achieved by exploiting the M criterion, which was firstly proposed by Pope [126]. According to such criterion, the turbulence resolution obtained in a simulation is suitably represented by the parameter M, defined as:

$$M = \frac{k_{mod}}{k_{res} + k_{mod}} \tag{3.32}$$

where k_{mod} and k_{res} are the modeled and resolved turbulent kinetic energy respectively. A satisfactory resolution of the flow field is considered to be achieved where the local value of M is below 0.2. For the present case, k_{mod} has been calculated as the time averaged value of k provided by the solver, while k_{res} has been derived from:

$$k_{res} = \frac{1}{2}\overline{u_i' u_i'} \tag{3.33}$$

where the time averaging operation is extended to the whole simulation time. Subsequent grid refinements have been performed, until a suitable turbulence resolution ($M < 0.2$ in the leading edge cavity) has been obtained for the test with Rej = 30000, CR = 70% and non uniform extraction: this goal has been achieved with the DDES model, while SAS scheme showed a lower grid sensitivity, and did not present turbulence resolution improvements below a certain grid refinement. The obtained M distributions are depicted in figure 3.5.

It can be observed that both SAS and DDES cover with RANS-like behavior the feeding channel and a relevant part of the crossflow plenum, as well as the inner part of the impingement holes. The differences become clear in the impingement cavity, where the DDES returns M values below 0.2 in the most part of such region , while the SAS resolves a significantly lower amount of turbulence, and covers the impingement jets themselves with a mostly RANS approach. This fact can be ascribed to the grid sensitivity of the DES model, where the turbulence resolution is triggered by the grid dimension: having provided the model with a sufficient mesh refinement, the impingement region is covered with the desired LES approach. On the other hand, the scale resolving capabilities of the SAS model are triggered by the flow field unsteadiness, thus where the flow instabilities are not sufficient the model applies a mainly (U)RANS approach, even with a LES-quality mesh. The obtained resolved turbulence distribution confirms the known guidelines for the application of

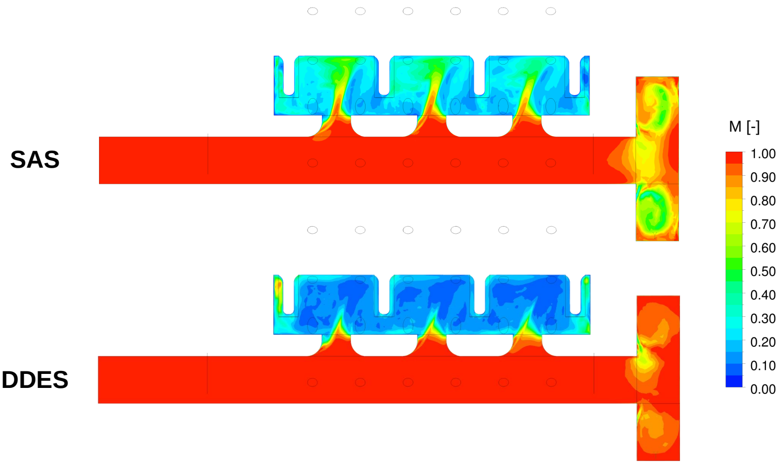

Figure 3.5: Distribution of M on the domain radial symmetry plane for the test with $Re_j = 30000$, $CR = 70\%$ and non uniform extraction.

these models: in fact the DDES model is suggested to be more suitable for locally unstable flows (like the present case is), while the SAS formulation for globally unstable ones [15].

However, it must be remembered that the scale resolution of the SAS is not achieved through an actual LES model (like the DES) but with an improved URANS formulation [114]. As a consequence, the M criterion is a suitable method to evaluate the quality of a LES or a DES simulation and to determine an adequate mesh size for these approaches, but these considerations are not valid for the SAS, given the different numerical approach on which it is based. In fact, in the next chapter SAS and DES will be shown to provide very similar results, despite the different values of M.

Following these guidelines, a $14.8 \cdot 10^6$ element, hybrid unstructured mesh has been obtained, using tetrahedral elements in the freestream region and 17 layers of prisms to cover the near wall regions. A representation of such grid is depicted in figure 3.6.

The boundary conditions of the static non-uniform extraction simulations

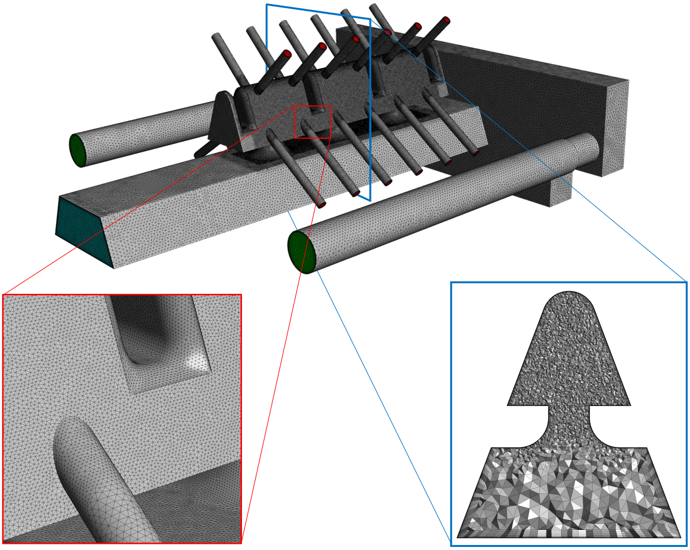

Figure 3.6: Numerical grid for the non uniform extraction case, with a detailed and a cross-sectional views.

also reply the ones used for the RANS case, except for the inlet, where a fixed mass flow rate has been imposed, and the crossflow outlet, which is now composed of two different sections (the two radial discharge ducts) and where an average static pressure value has been set. The values imposed at the boundaries have been tuned to obtain the desired flow conditions, using a preliminary RANS simulation as an initialization run. Concerning the rotating tests (performed only exploiting the DDES model), further differences have to be considered. A rotating relative reference frame has been exploited to impose the desired rotating speed; moreover, a differentiated static pressure condition was applied on each outlet of both FC and SH rows (a different pressure for each hole of the extraction row). This, in order to compensate radial pumping effect due to rotation, as experimentally made by means of symmetric connections between model and plenum [127, 128].

Regarding the finite approximation of the variables, the High Resolution scheme of CFX has been exploited, which automatically blends between Upwind and Central Difference when the solution switches from RANS to LES-like [120]. Transient simulations have been run using a Second Order Backward Euler scheme for the transient term discretization, and the time step has been set to $2 \cdot 10^{-5}\, s$: such value has been derived from a sensitivity analysis, and is small enough to maintain a Courant number lower than 1 in all the domain significant regions and residuals below 10^{-4} for every transport equation. The computations have been run for 3000 time steps for initialization purposes, and the sampling has been performed for the subsequent 8500 time steps (corresponding to a simulation time of 0.17 s): such interval has been chosen to ensure the flow to transit at least one time through the entire domain. All the relevant quantities have been calculated as the time average value on the sampling time interval.

All the aforementioned settings are common to both SAS and DES runs. The only difference between the two simulations is, in fact, the turbulence model itself. For the first, the SST-RANS model has been exploited, which is built upon the RANS k-ω SST formulation: in ANSYS® CFX v15, the latest version of such model [116] is implemented. For the second run, the SST-DES model has been used, which also applies the k-ω SST model in the RANS regions; however, given the excessively conservative behavior of the CFX implementation of DES shielding function [114], a delayed DES (DDES) model has been applied for the present case.

All the other numerical settings have been recovered from the RANS simulations, thus for more informations refer to section 3.3.1.

Chapter 4

Experimental and numerical results in static conditions

In this chapter both experimental and numerical results obtained in static conditions are presented. The heat transfer coefficient distribution achieved during the experimental investigation on the leading edge internal surface is firstly discussed. Then, the effects on the cooling system effectiveness of several characteristic fluid dynamic parameters is shown, such as the jet Reynolds number, the cross flow mass flow rates or the different (uniform or non-uniform) extracted coolant mass flow split. After that, the results of the numerical investigation performed in static conditions are reported: firstly, RANS simulations carried out on the uniform extraction configuration are discussed; then the benchmark of the two hybrid RANS-LES models in non-uniform extraction conditions is reported. The comparison between computational and experimental results is finally shown in order to validate the computational models.

During the present work, the impingement cooling system effectiveness will be analyzed exploiting the Nusselt number (Nu) distribution on the leading edge internal surface. In fact, Nu represents a suitable dimensionless expression of the heat exchange coefficient:

$$Nu = \frac{hl}{\lambda}, \tag{4.1}$$

where h is the heat transfer coefficient, l is a case-dependent reference length (the impingement hole hydraulic diameter in this work) and λ is the fluid thermal conductivity.

To avoid ambiguity, directions names are chosen to be coherent with the real blade reference system: as a consequence, crossflow and leading edge direction will be referred as radial, while the lateral extension of the profile will be defined as circumferential, as illustrated in figure 4.1.

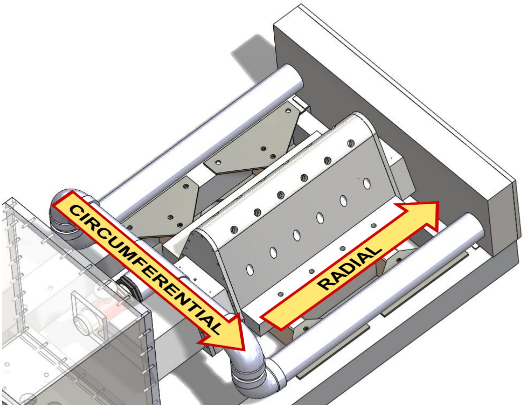

Figure 4.1: Directions definitions on the model geometry.

4.1 Experimental results

The results of the experimental campaign are presented in this section. Following the test matrix described in the paragraph 2.9.1, Nusselt number distributions are reported for the uniform extraction case in figure 4.2 (i.e. tests where each extraction row draws 25% of the coolant mass flow rate) and for the non uniform extraction case in figure 4.3 (i.e. tests where 10%

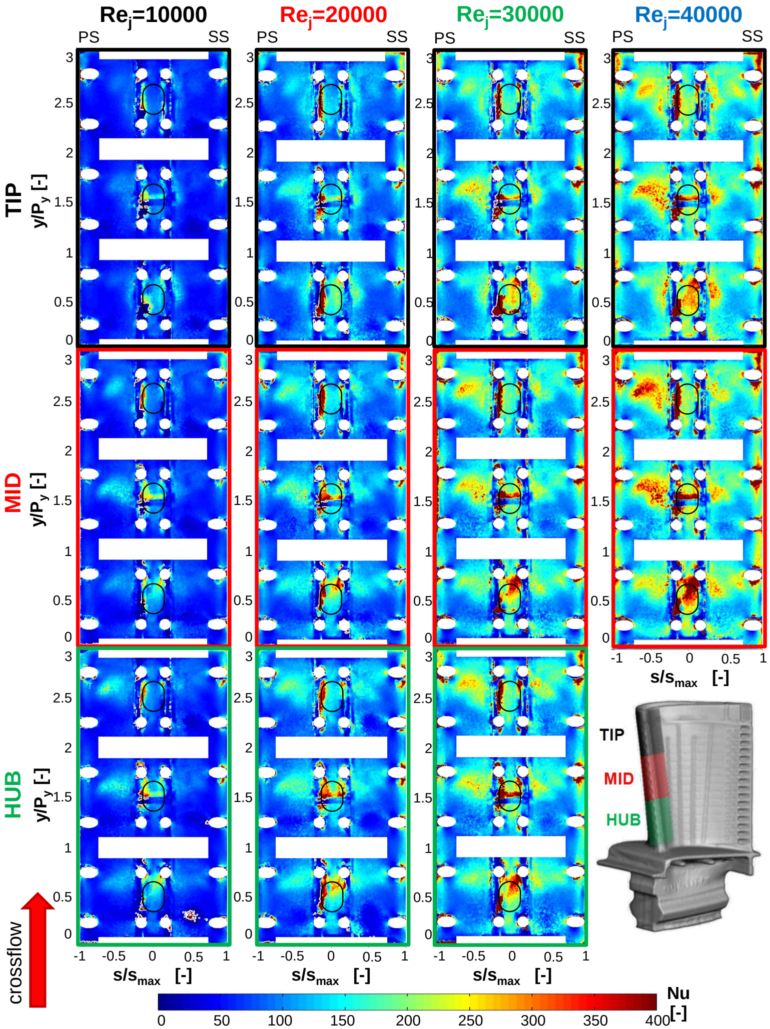

Figure 4.2: Nu distributions for tests with uniform extraction.

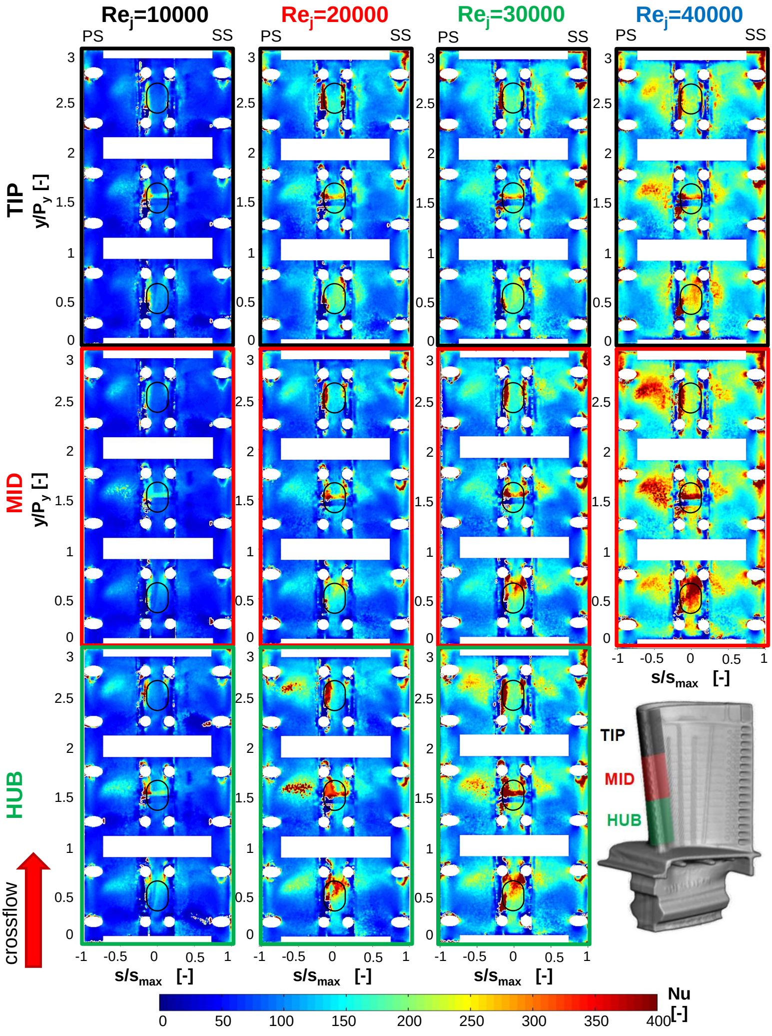

Figure 4.3: Nu distributions for tests with non uniform extraction.

of the coolant mass flow rate is extracted by the FC PS row, 40% by the FC SS row and the remaining 50% by the showerhead rows) varying both jet Reynolds numbers and crossflow conditions. Moving from left to right, Re_j varies form 10000 up to 40000, while from the bottom to the top of the figures CR goes from 70% to 10%. Since the different crossflow rates stand for the hub, mid the tip regions of the blade, such representation enable to study the whole span of the blade, and allows to appreciate the heat exchange variation through the total cooling system extension.

For a better representation, Nu distribution on the inner curved surface has been reported to a flat plane through geometric development. On such flattened surface, horizontal coordinate s represents the circumferential distance from leading edge, and is scaled with the maximum lateral extension s_{max}; instead, vertical coordinate y indicates the radial distance from the inner point of the measurement surface, and is scaled with the impingement holes radial pitch P_y. The area corresponding to the ribs has been removed from the analysis, because of the constraints implied by both the geometry and the measurement technique; at the same time, even the extraction holes positions have been excluded from the analysis. The projection of the impingement hole position is also represented on the maps.

4.1.1 *Nu* distribution analysis

As shown in figure 4.4, a qualitative analysis of Nu distribution reveals that three high heat exchange areas are present for each impingement module, two of which are located on the lateral flat surfaces, while the remaining one is positioned in the center of the highly curved LE surface, between the showerhead holes. The lateral high Nu zones are elongated in shape, and for some tests are almost split in two separate lobes. Given their position, such peaks can be attributed to the interaction between the impingement jets and the lateral surfaces: the flow exits the impingement hole, expands and impacts on the lateral surfaces, before even reaching the center of the target area. The presence of two lobes for some tests is not easy to explain: a possible reason for such shape could be the

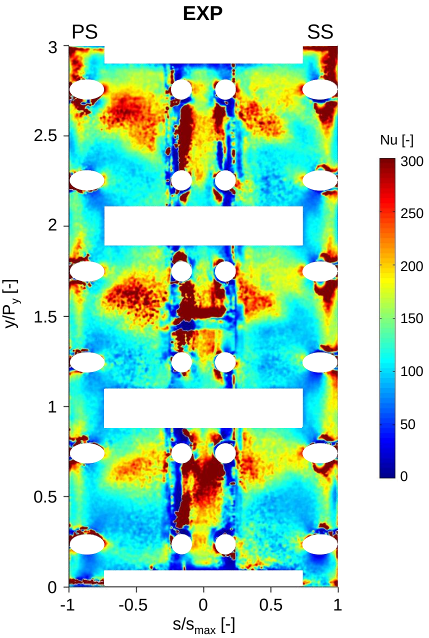

Figure 4.4: Nu distributions for tests with non uniform extraction.

impact of unsteady flow structures (eddies) entrained by the jet [8]. Even if a similar unsteadiness has not been evidenced in the experiments, a high frequency fluid (and thus thermal) phenomenon could have been easily masked and averaged by the thermal inertia of the surface coating. These suppositions about the flow field instabilities and the consequent arising of such two-lobes shape of the high Nu area, are evidenced by the computational analysis, which will be illustrated in this chapter. Such high heat transfer zones are located downstream the impingement hole (with respect to the crossflow direction), which indicates that they are not able to completely deflect the flow into a perpendicular jet, which is bent towards radial direction.

The central high heat transfer zone can be interpreted as the combined effect of direct jet impingement and showerhead extraction. However, their entity and shape are not easy to identify, given the high disturbance of such area: the leading edge model is indeed a highly critical region at detecting HTC distribution, for both optical and manufacturing issues. In fact the use of punctual and intense light sources creates strong shadows and reflections, especially in such zone because of the interaction with the showerhead hole rows; this phenomenon has been reduced through the use of three flashes and their accurate positioning, though a complete elimination can not be achieved. Moreover the model is composed of different PMMA modules, consisting in two cylinder sectors and two flat plates; even though the glue ensures structural and optical continuity for PMMA, the inclusion of air into the connected interface interrupts such continuity, thus generating additional shadows and reflections.

Despite of all these issues, it can be observed that the central high Nu region is located near the outer couple of showerhead holes: sometimes there are two separates peaks near the extraction holes, while in some tests they tend to converge into a unique, round shaped high heat exchange zone.

Considering the three impingement modules of a single test, it seems like Nu values increase in the crossflow direction, which can be attributed to the static pressure recovery in the feeding channel [66]. Such statements are valid for both the uniform and the non uniform extraction cases.

4.1.2 Effect of Re_j variation

In order to better highlight the effect of Re_j variation on heat exchange, both radially and circumferentially averaged Nu trends are reported respectively in figures 4.5 and 4.6. Such profiles are there presented on the first impingement module for tests with a crossflow of 40%. The disturbed zones surrounding the connection between the model pieces and the areas corresponding to the ribs are removed from the graphs, and are not considered for average values calculations.

It can be observed that an increment in Re_j has a positive effect on heat exchange, which is verified in every point of the distribution: this

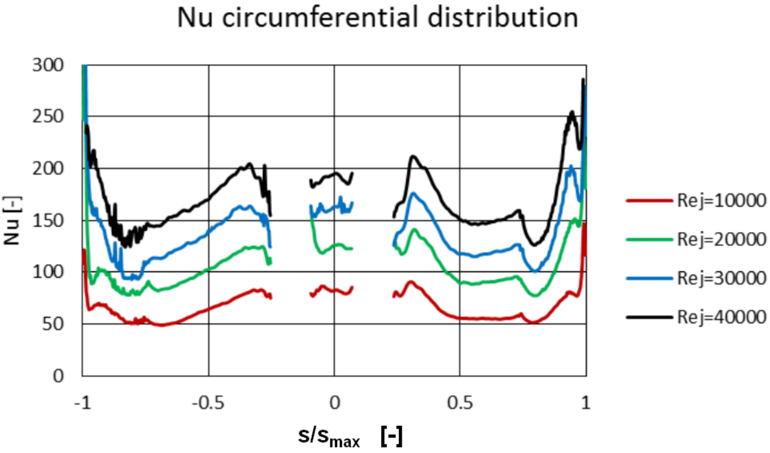

Figure 4.5: Radially averaged circumferential Nu trends for the first impingement jet, for different Re_j values ($CR = 40\%$).

trend can be identified for every impingement module and in all crossflow conditions, for both uniform and non uniform extraction cases.

Such phenomenon is coherent with the data available from works of many researchers found in literature, done on similar geometries [29, 42, 56], as confirmed by figure 4.7, which represents a quantitative expression of the Nu-Re_j dependency by plotting the area averaged Nu values versus the corresponding Re_j. It shows a comparison of both experimental and numerical mean results for each tested condition (numerical results will be discussed in the following sections), against the results obtained by Andrei et al. [56] and two other correlations: the Taslim correlation [42] and the Chupp correlation [29].

Both measured and CFD results, shown in this work, present the same increasing trend along with the Re_j number. Experimental results have a very good agreement especially with Taslim correlation, meanwhile the measured HTC is a bit higher then both Andrei et al. results and Chupp correlation. These differences could be due to the slightly different

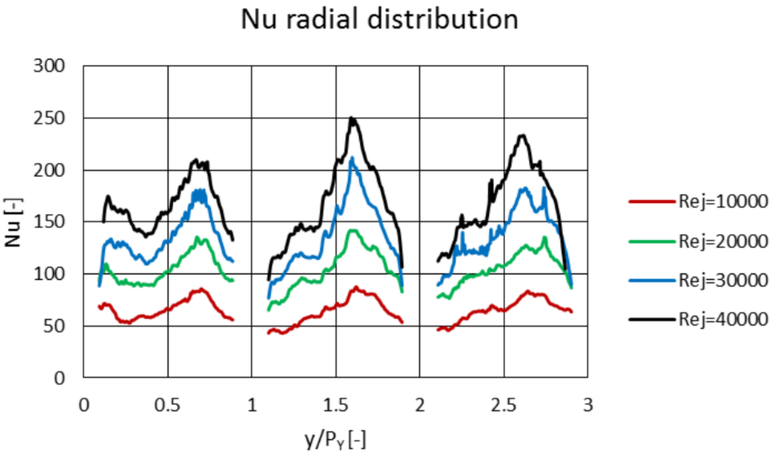

Figure 4.6: Circumferentially averaged circumferential Nu trends for the first impingement jet, for different Re_j values ($CR = 40\%$).

geometry between the Maiuolo's tested LE and the actual, in particular for the different extraction area ratio (between coolant extraction holes area and jet impingement holes area on the internal platform) which can affect the flow field into the LE cavity. The Chupp correlation [29] was instead defined for in-line impingement jets, while in the present test section there are four internal ribs which confined the jet impingement on a little span extension. The presence of a transverse flow (respect to the jet) may affect the flow field of both the direct impact of the impingement and the recirculating region in the LE section reducing the mean heat transfer distribution.

4.1.3 Effect of crossflow condition

The effects on the heat transfer distribution on the leading edge due to the variation of crossflow conditions can be verified in figures 4.2 and 4.3. A more quantitative analysis can be performed by comparing the circumferentially averaged Nu trends at various crossflow values with

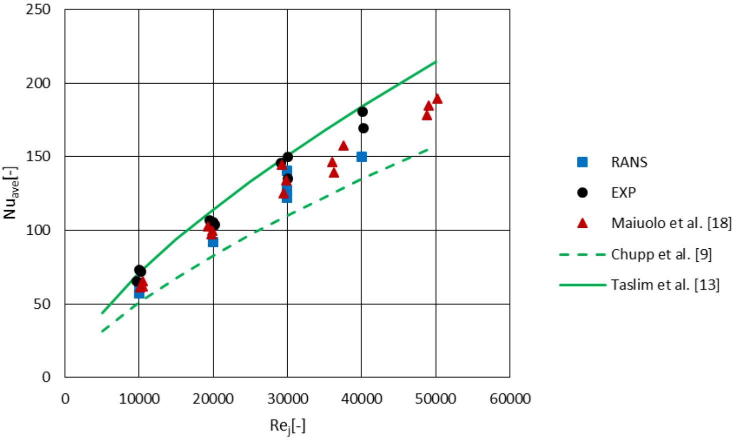

Figure 4.7: Comparison between experimental, CFD and correlations Nu values (averaged on the LE surface).

a constant Re_j, as presented in figure 4.8 (for the first jet and with a $Re_j = 20\,000$). It can be depicted that a decrease in the crossflow mass flow rate tends to increase the heat exchange in the inner zone of the lateral surface ($s/s_{max} = \pm 0.25 - 0.45$), while the contrary happens on the outer zone ($s/s_{max} = \pm 0.55 - 0.85$). A similar trend has been identified also by Andrei et al. [56], and can be interpreted as the consequence of two interacting aspects: an impingement jet inclination variation and the extraction holes location. A scheme of the presumed flow field is presented in figure 4.9. Because of the stronger inertial forces of the coolant into the feeding duct, a higher crossflow causes in a more inclined jet with respect to the target surface, which implies a greater distance between the jet orifice and the solid wall. As a consequence, the jet undergoes a greater diffusion and impacts mainly on the lateral surfaces. For lower crossflow values, the impingement hole achieves a more complete flow deflection, which results in a jet heading directly towards the leading edge region. However, in such zone showerhead holes are present, which draw a part of the impinging jet: the impact is thus direct, but also dampened by the

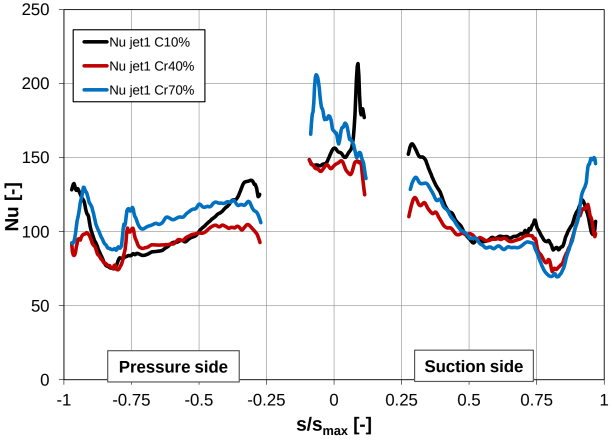

Figure 4.8: Radially averaged circumferential Nu trends for the first impingement jet, for different crossflow conditions ($Re_j = 20\,000$).

flow extraction. This supposition finds confirmation in PIV measurements, performed by Furlani et al. [99] at the University of Udine, as shown in figure 4.10. The measured internal flow field is reported in terms of 2D velocity on the two internal planes described in section 2.7 (XZ and YZ); velocities are scaled with respect to the jet bulk velocity, defined as:

$$U_b = \frac{\mu Re_j}{\rho D_h} \tag{4.2}$$

Even if such PIV measurements are performed in non-uniform extraction conditions, observing figure 4.10, the evolution of the jets can be noticed. In the HUB configuration the mass flow rate leaving the feeding channel is 7/3 of the mass flow rate through the three jets; the consequent high inertial forces do not allow the impingement holes to completely drive the flow normal to the leading edge surface, and the jets migrate towards the ribs. This effect is mitigated going towards the TIP configuration, given the lower cross-flow entity. Another effect of the various cross-flow

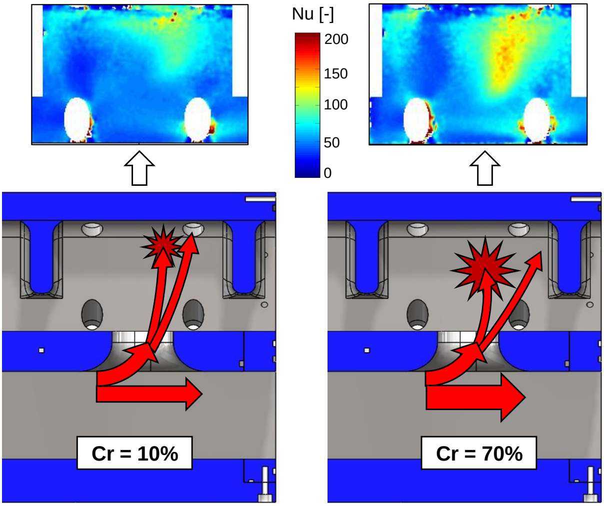

Figure 4.9: Presumed flow fields and resulting Nu distributions for different crossflow conditions.

configurations is the different spreading of the jets. TIP configuration presents a higher spreading along the crossflow direction as visible on the XZ plane of figure 4.10, while a more coherent jet exit the impingement hole in HUB configuration. Concerning the spreading on the lateral surfaces (circumferential direction), detected on YZ plane,it could be noticed that it is higher for higher feeding channel flow velocities (HUB) leading to the aforementioned stronger impact of the coolant on the lateral flat plates. The slight jet displacement towards the pressure side detected on the YZ planes is due to the non-uniform extraction condition, and its effect o Nu distribution will be deepen in the following section.

4.1.4 Effect of extracted flow split

The availability of two different measurement sets, with uniform and non uniform coolant extraction, allows to determine the effect of the

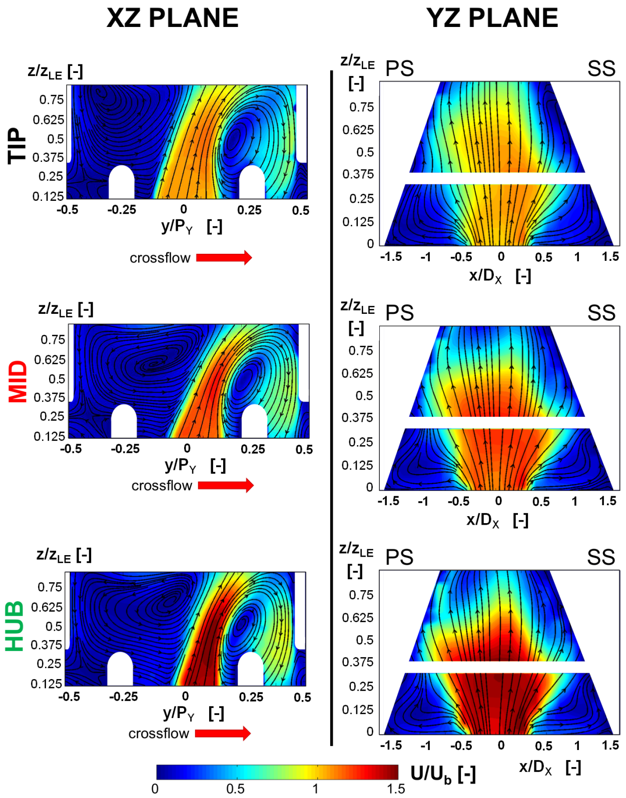

Figure 4.10: PIV velocity maps in static conditions for a whole blade configuration at $Re_j = 30000$.

external pressure distribution on the internal blade cooling system.

Looking at two Nusselt distributions for uniform (figure 4.11 (a)) and non uniform (figure 4.11 (b)) flow extractions, it can be stated that the overall effects of coolant flow distribution are weak and do not alter neither the average heat transfer entity nor the Nu distribution in a significant way. Such reduced influence of extraction conditions is also verified in the open literature [34]. It is possible to observe that neither of

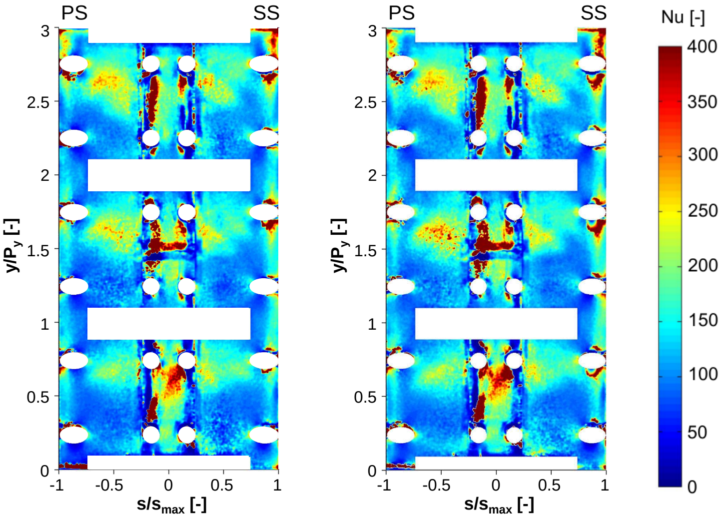

Figure 4.11: Uniform (a) and non uniform (b) extraction cases Nu distributions, for tests with $Re_j = 30000$ and $CR = 70\%$.

the maps depicted in figure 4.11 is symmetric, not even the one obtained from the uniform extraction test. This fact can be due to inaccuracies in the model manufacturing and in the rig assembling, and is a minor effect if compared to Re_j or crossflow variations, as seen in the previous paragraphs. However, this asymmetry can interfere with the one due to the distribution of coolant flow, eventually concealing the effects of the latter. To overcome this issue, the relative difference between two tests can be evaluated, thus considering the basic asymmetry as an offset and highlighting the sole effects of coolant extraction. Such comparison is more suitably performed in terms of Nu/Nu_0 values, where Nu_0 is a reference value obtained from a correlation extracted from all the experimental data (uniform and non uniform extraction cases):

$$Nu_0 = 0.1917 Re_j^{0.6418} \tag{4.3}$$

This is required by the fact that an exact reproduction of nominal Re_j value could not be achieved for the tests, and that the variation of the latter parameter has a strong influence on Nu values. By subtracting the Nu/Nu_0 distributions for non uniform and uniform extraction tests performed in similar Re_j and crossflow conditions, maps of the kind represented in figure 4.12 can be obtained: values above zero indicate that the extracted flow split enhances heat exchange, while the contrary happens for values below zero.

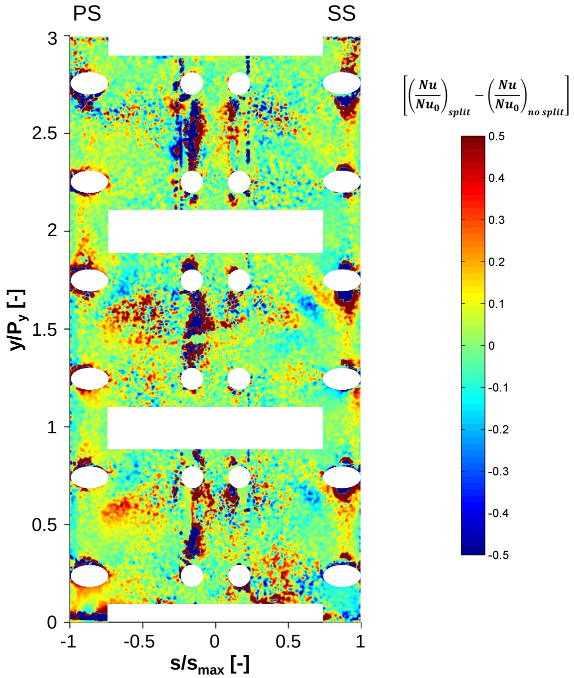

Figure 4.12: Difference between Nu/Nu_0 distributions of non uniform and uniform extraction tests ($Re_j = 30000, CR = 70\%$).

The distribution of figure 4.12 allows to identify that, at least for the first and second jet ($y/P_y = 0 \div 2$), an uneven coolant flow extraction leads to a strengthening of the heat exchange peak on the pressure side: this fact can be due to the lower mass flow rate of pressure side film cooling holes (from 25% to 10% of the total coolant flow), which reduces the impinging flow deflection and thus strengthens the jet impact. Similarly, the effect of mass flow rate increase for suction side film cooling holes (from 25% to 40% of the total coolant flow) can be observed mainly on the suction side itself: in such region, it can be noticed that near the outer film cooling hole of each module ($y/P_y \simeq 0.75$ and $y/P_y \simeq 1.75$) Nu/Nu_0 increase and decrease regions are adjacent, which reveals a shift of the high heat transfer zone towards the holes itself. On the contrary, these effects seem to be almost absent for the third impingement module ($y/P_y = 2 \div 3$), where the only evidence consists in a slight heat transfer increase for the pressure side and in a slight decrease for the suction side. The aforementioned considerations have been confirmed by CFD analysis, as illustrated in section 4.2.2.

4.2 Computational results

The main findings achieved by the numerical investigation during static simulations will be presented in the following sections. Firstly the CFD investigations of the uniform extraction case, performed exploiting a RANS approach, are reported. Then, the unsteady simulations carried out on the non-uniform extraction tests are presented, with particular attention paid to the benchmark of two hybrid RANS-LES models: SAS and DDES.

4.2.1 Uniform extraction case simulations

The first numerical analysis performed in the frame of the present work involves the tests with uniform mass flow extraction, i.e. the ones in which both film cooling rows extract 25% of the total coolant mass flow each, and the two showerhead rows the remaining 50%. This case has been suitably simulated by means of a steady RANS approach, as will be presented in this section.

Given the relatively low computational cost of RANS simulations, a complete variation range of the main parameters has been achieved:

- $Re_j = 10\,000 \div 40\,000$ (for $CR = 10\%$)
- $CR = 10\% \div 70\%$ (for $Re_j = 30\,000$)

The resulting Nu distributions are depicted in figures 4.13 and 4.14 respectively, along with the experimental results obtained in the same flow conditions (i.e. same Re_j and crossflow percent). For clarity purposes, the RANS results have been reflected with respect to the symmetry plane, in order to cover the full impingement surface.

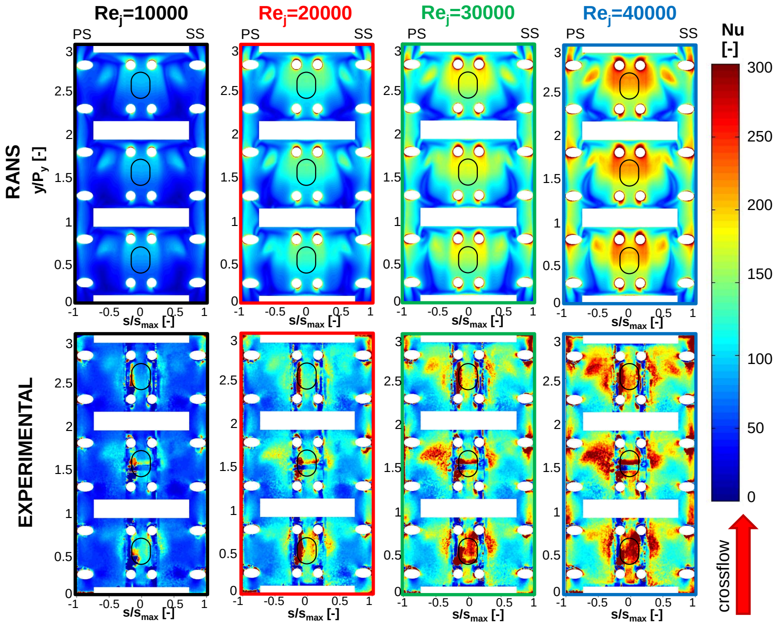

Figure 4.13: Nu maps comparison for RANS and experimental tests performed with $CR = 10\%$.

The comparison performed in figure 4.13 reveals a general underprediction of Nu values with respect to the experiments. The difference is

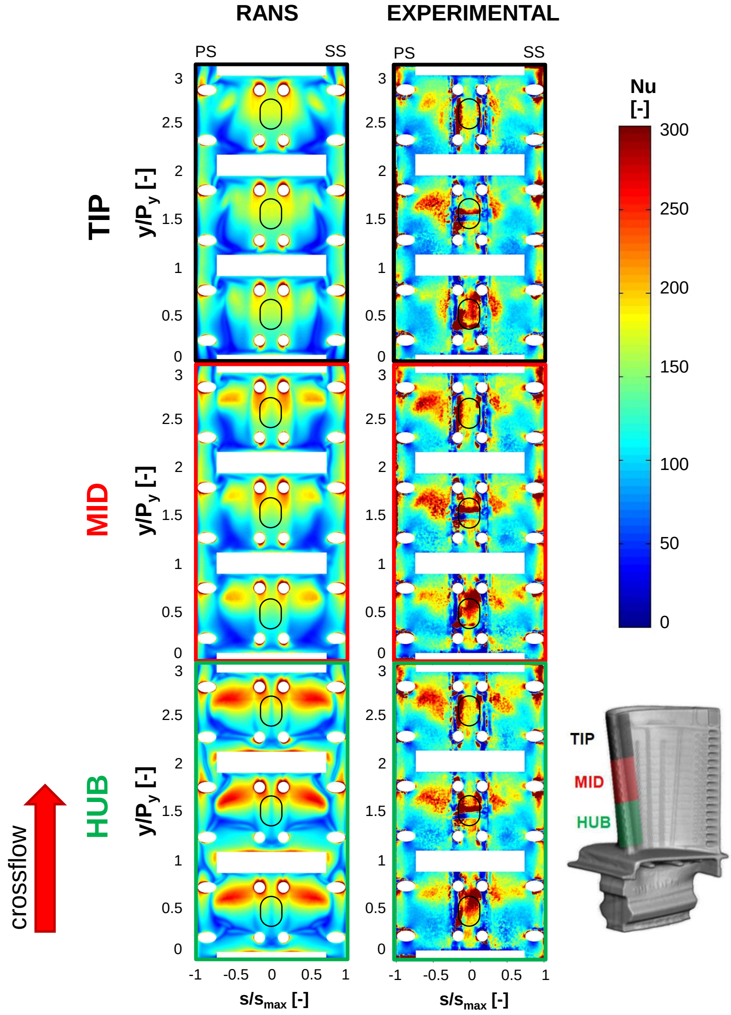

Figure 4.14: Nu maps comparison for RANS and experimental tests performed at $Re_j = 30\,000$.

less marked on the peak values, while in the remaining zones is more pronounced. Despite this, the shape of the Nu distribution is correctly predicted in the most cases: this leads to the supposition that the simulations manage to suitably reproduce the actual flow field inside the model, and that the discrepancy could be mainly due to wall values. Regarding this fact, it must be remembered that the numerical campaign has been performed before the experimental one, thus the exact values of fluid temperature and wall heat flux could not be imposed: this fact could have caused local alterations of flow and thermal phenomena, which could have contributed in part to such discrepancies.
The analysis of the Nu distribution shows that the impact locations are correctly predicted by the CFD, with only local differences. In particular, there is a stronger tendency of the two central heat exchange peaks at converging into a single structure; moreover, the lateral peak, located for all the tests at $s/s_{max} \simeq 0.5$, is usually smaller then the one detected by the experiments. The shape of the Nu pattern around the film cooling holes is also reproduced with a reasonable accuracy. The maps also show that the increase in Nu values with a higher Re_j value is visible in both the measured and the calculated data, and its entity seems reasonably similar.
These considerations can be repeated in quantitative terms, if the radially averaged circumferential trends of Nu are analyzed: an example of the comparisons for the considered cases is depicted in figure 4.15, along with the error distribution, defined as:

$$err = \frac{Nu_{CFD} - Nu_{EXP}}{Nu_{EXP}} \cdot 100\% \tag{4.4}$$

The trend confirm the constant underestimation of RANS results with respect to the experimental ones, with numerical values showing an error of around 30% on the flat lateral surfaces. A more accurate prediction can be observed near the film cooling holes. Despite the values shift, it can be noticed that the trend is closely reproduced by the simulations. If the areas where both experimental and numerical results are available are considered, the overall maximum error on the area averaged Nu value is

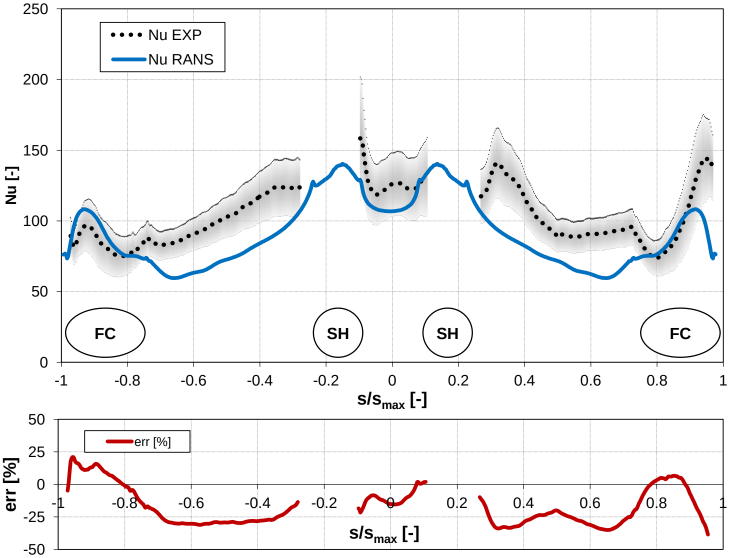

Figure 4.15: Circumferential Nu trend for RANS and experimental tests performed with $Re_j = 20\,000$ and $CR = 10\%$. The uncertainty of the experimental data is represented, as well as the holes position.

-18.38% for this set of simulations, verified for the test wit $Re_j = 40\,000$. Regarding the constant Re_j tests, the maps of figure 4.14 reveal that the numerical simulation tend to overpredict the change in Nu values with a crossflow variation: while the experimental data are almost insensitive to a change in the feeding channel mass flow rate, the numerical ones show a strong variation in heat exchange entity. Despite this, the shape of the Nu pattern seems to be suitably reproduced by the simulations, with some exceptions. For the 70% crossflow test, the Nu peaks show a wider lateral extension, involving the upper half of the target area between $s/s_{max} \simeq -0.8$ and $s/s_{max} \simeq 0.8$; only a slight shift towards lower y/P_y values can be observed in the simulations. For the 40% crossflow test, in both computation and experiment the size of the lateral peak is strongly reduced, with a corresponding expansion of the central high Nu area; in this case, the lateral peak extension seems slightly underestimated by the CFD, and its shape seems also not to totally coincide: this could be due to a different jet expansion, which could be lower in the simulated test. For the 10% crossflow test, the entity and extension of the lateral peak is further reduced in both numerical and experimental data; the accord in terms of shape is still satisfactory, but the same considerations performed for the 40% crossflow test can be repeated. A quantitative analysis for these tests is presented in figure 4.16.

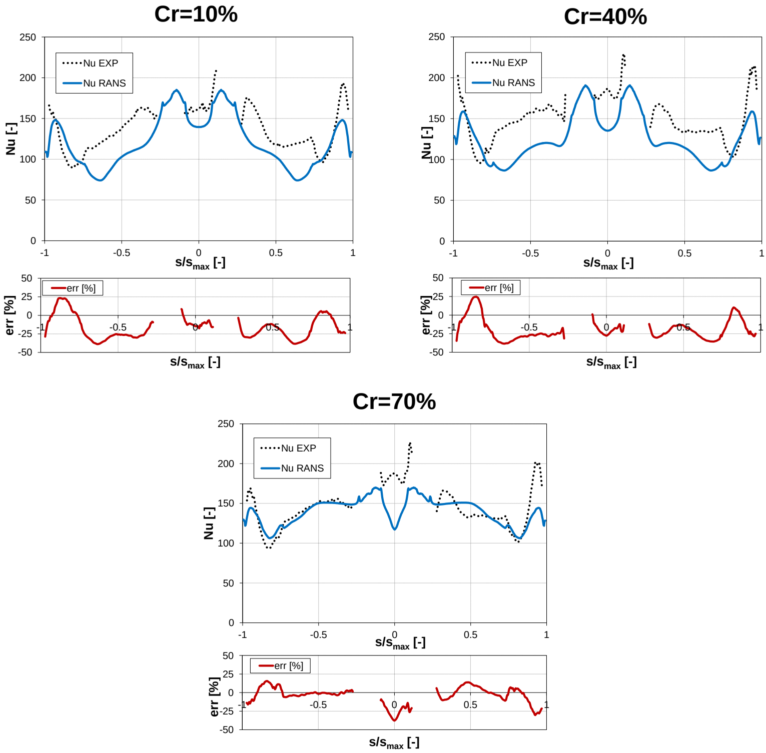

Figure 4.16: Circumferential Nu trends for RANS and experimental tests performed with $Re_j = 30\,000$.

It can be observed that the agreement is good for the 70% crossflow simulation, while for the 40% and 10% crossflow tests generally underestimate the experimental results: the relative error of the area averaged Nu is -5.79% for the first test, while the latter present errors of -17.65% and -20.75% respectively.

Despite the mentioned underestimation, it has been observed that the heat exchange pattern is suitably reproduced by the simulations; thus, the RANS numerical model is validated and it could be considered a suitable tool to interpret the flow field and deepen the physical phenomenon of such cold bridge cooling system.

If the flow field inside the impingement cavity is considered, the simulations show that a higher crossflow causes a larger spreading and a greater inclination of the jets: this causes the jet to directly impinge on the lateral surfaces (figure 4.17 (a)), resulting in higher local Nu values. On the contrary, a lower crossflow value causes the jet to aim directly at the showerhead holes, thus a considerable amount of jet flow is extracted before being able to perform the cooling action (figure 4.17(b)). This fact provides an explanation for the experimental Nu distribution, and substantially confirms the hypothesis about flow field presented in section 4.1.3: a lower crossflow shifts the impact location towards the center of the geometry (lower $|s/s_{max}|$ values), but the peak entity is not intensified due to coolant extraction from the jet. The effect of the crossflow value

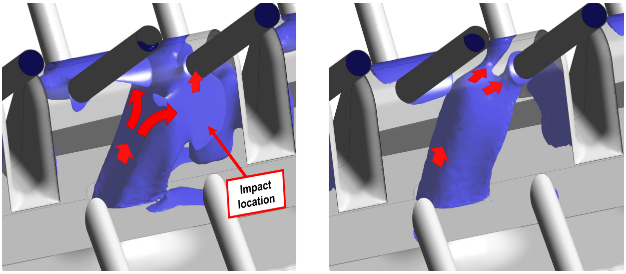

Figure 4.17: Velocity isosurfaces ($v = 10\ m/s$) of the second jet region for $CR = 70\%$ (a) and $CR = 10\%$ (b) tests with $Re_j = 30\,000$.

on jet inclination can be clearly observed also from figures 4.18 and 4.19, which represent the flow fields on the symmetry plane for the second jet and on a circumferential plane through the axis of the same jet: a higher crossflow value tends to bend and laterally spread the jet, thus altering the shape and size of the impact location. Moreover, the jet of the 70% crossflow case shows a higher velocity, which explains the higher Nu values with respect to the 10% case. An explanation of such higher velocity could be the computed flow behavior inside the impingement hole itself: the higher crossflow value causes the air to enter the hole with a greater angle, with respect to the the hole axis: given the relative small length-to-diameter ratio of the hole, this causes the flux to “see” a smaller passage area, which then results in a higher velocity. It is expected this effect to take place for both the real and the computed case, but since in the second case the jet might be more coherent [129], the resulting velocities could be higher and the impact location more defined.

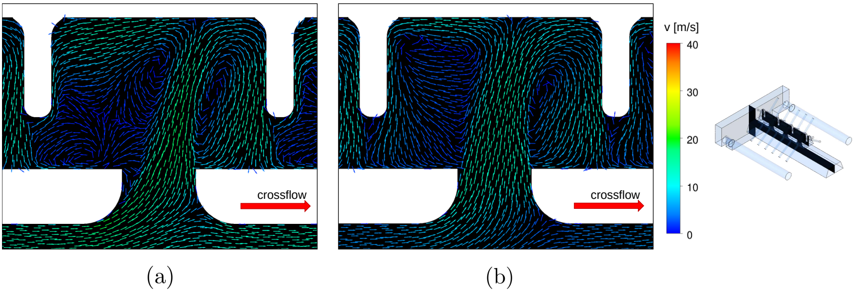

(a) (b)

Figure 4.18: Vector plots on the symmetry plane of the second jet for $CR = 70\%$ (a) and $CR = 10\%$ (b) tests with $Re_j = 30\,000$.

As concluding remark, it can be stated that the performed RANS simulation are not able to exactly predict the pure Nu values, given the widespread under-prediction of experimental data. However, the relatively accurate reproduction of both the heat exchange pattern and its trend varying the Re_j and the CR allows to use their results to interpret

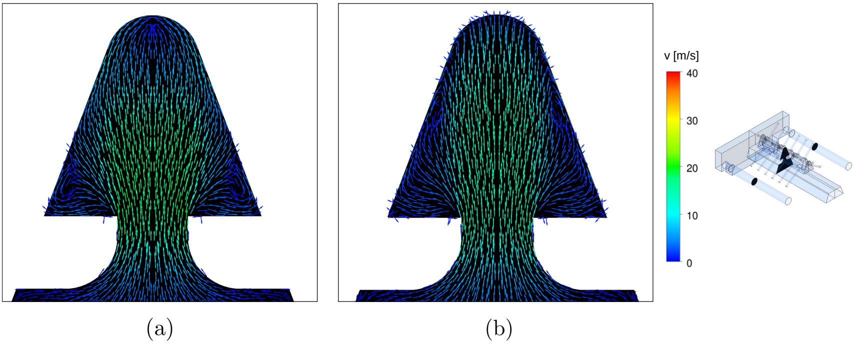

(a) (b)

Figure 4.19: Vector plots on a cross-section plane of the second jet for $CR = 70\%$ (a) and $CR = 10\%$ (b) tests with $Re_j = 30\,000$.

the flow field structures inside the impingement cavity. This model can also be used to investigate similar cases assessing the impact of minor modification of the geometry or in different test conditions, like will be reported in the following section.

4.2.1.1 Coolant extraction area effects

As suggested in the previous section, the RANS model could be exploited to assess the effect of several geometrical and fluid-dynamics characteristic parameters. In this section the analysis performed with the aim to study the effect of a different coolant extraction area of the FC and SH holes on the heat transfer distribution is reported. Such numerical investigation has been carried out in order to clarify the differences of the results of the present work with respect to another experimental investigation, performed by Andrei et al. [56], on a similar LE geometry having different extraction area. In order to evaluate such effects, results from Andrei et al. are compared with the new experimental results and CFD simulations. Two different computational models were developed: the first model, referred as RANS1, represents the simulation reported in the previous paragraphs replicating the real test rig geometry; the second one, referred as RANS2, is identical to the first, apart from a reduction in FC and SH holes cross sectional area. Its extraction area was reduced in order to obtain the same value of Andrei et al. [56] tests, and was then scaled down to consider the different scale factors of previous and new geometries. The comparison between the results of each test point, is reported in figure 4.20, where a comparison of a non-dimensional Nu (each map is obtained dividing Nu for its area averaged value) distributions is shown for a Re_j value of 30000. This comparison reveals that a reduction in extraction area does not significantly alter the Nu distribution shape.

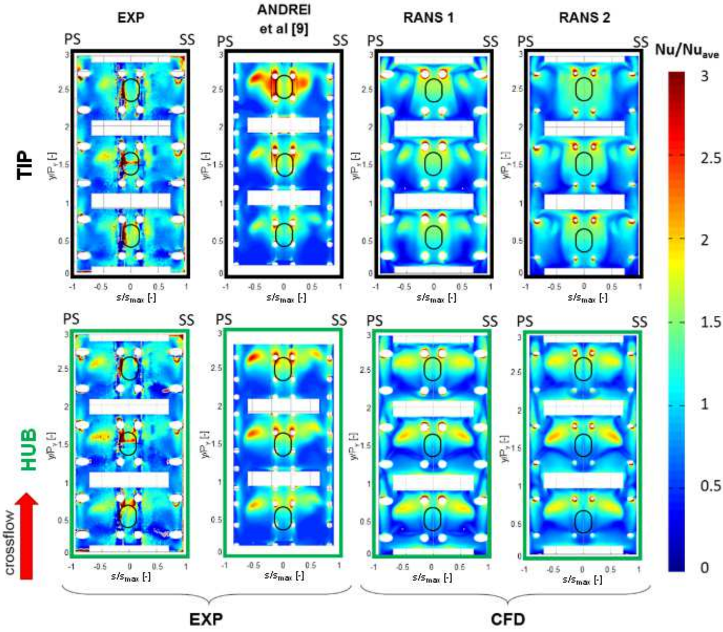

Figure 4.20: Coolant extraction area effect - Experimental and numerical results.

Experimental results show very similar Nu peaks related to the impingement jet shapes, nevertheless a sharper Nu reduction far from them can be observed in Andrei et al. [56] results. The Nu distribution seems to be well replicated by both simulations as well. Computations performed with CR=70% show a stronger similarity between full and reduced extraction area cases, while slight differences are present for the CR=10% tests. A smaller extraction area causes a reduction in extension and entity of the lateral Nu peaks, while the central high Nu area appears to be widened and strengthened. This fact can be justified by considering that, as already said, a smaller crossflow rate causes the flow to be strongly guided by the impingement hole, leading to a direct impact of the jet on the central curved region of the target surface where the showerhead holes are. The different and smaller SH extraction holes strongly affect the flow field in such zone since they cause a stronger acceleration field, which intercepts a higher jet mass flow and draws it towards the central region. For the tests with CR=70%, where the jet impacts mainly on the lateral flat surfaces, the effects on heat exchange of the flow field surrounding the extraction holes are smaller.

4.2.2 Non-uniform extraction case simulation

The second part of the numerical activity, concerning the simulations performed in static conditions, consisted in the study of non uniform extraction tests, i.e. the ones in which film cooling pressure side row extracts 10% of the total cooling flow, film cooling suction side draws 40% of it and the remaining 50% passes through the two showerhead rows. In such case, the asymmetric flow field does not allow to exploit the domain geometric symmetry, and thus the whole model must be considered into the simulation (see section 3.3.2).

Starting from the results obtained in the uniform extraction case, a first attempt was performed using exactly the same numerical settings, but on the complete domain. However, the RANS steady approach did not allow to obtain a converged solution for such case: an unsteady, oscillating convergence history was always obtained, in spite of the application of the convergence-improving settings described in the previous section.

Given the positive results obtained in previous studies performed in the Department of Industrial Engineering of the University of Florence [119] [114], hybrid RANS-LES approaches have been chosen. In particular, the DES and SAS models have been tested, with the aim not only to model and interpret the present case, but also to determine which of these models is the most suitable for impingement cooling simulations. To achieve this goal, the same computational setting has been used for both SAS and DES, in order to highlight the effects solely bound to the different turbulence modeling. The computational cost of an unsteady simulation is still at least one order of magnitude higher than a steady one, thus it was necessary to limit such investigation to a single test case: the test with $Re_j = 30\,000$ and with a crossflow of 70% has thus been chosen as the reference case to be investigated. The time averaged Nu distributions on the impingement target surface for both the SAS and the DDES simulations are presented in figure 4.21, along with the corresponding experimental test result.

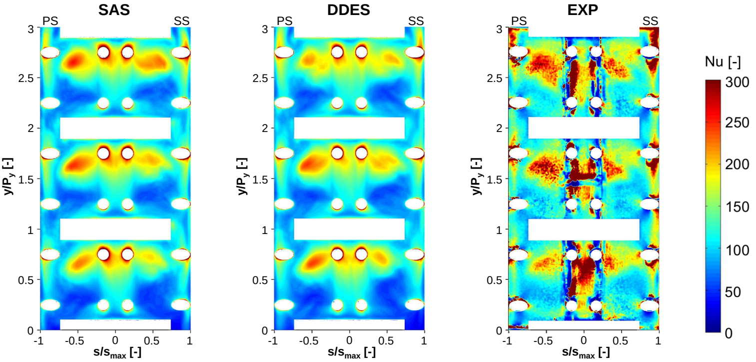

Figure 4.21: SAS (a), DDES (b) and experimental (c) Nu distributions, for the test with $Re_j = 30000$, $CR = 70\%$ *and non uniform extraction.*

From the analysis of such distributions, a general underestimation of the numerical results with respect to the experimental one can be noticed, since both SAS and DDES seem to predict Nu values lower than the experimental ones on the whole impingement surface. Despite that, a very good qualitative agreement is reached by CFD as the shape of Nu distributions are very similar to the measured one. On the contrary, a remarkable similarity can be observed between the SAS and DDES results.

These considerations are even more evident if the single impingement modules are analyzed, as shown in figures 4.22(a), (b) and (c).

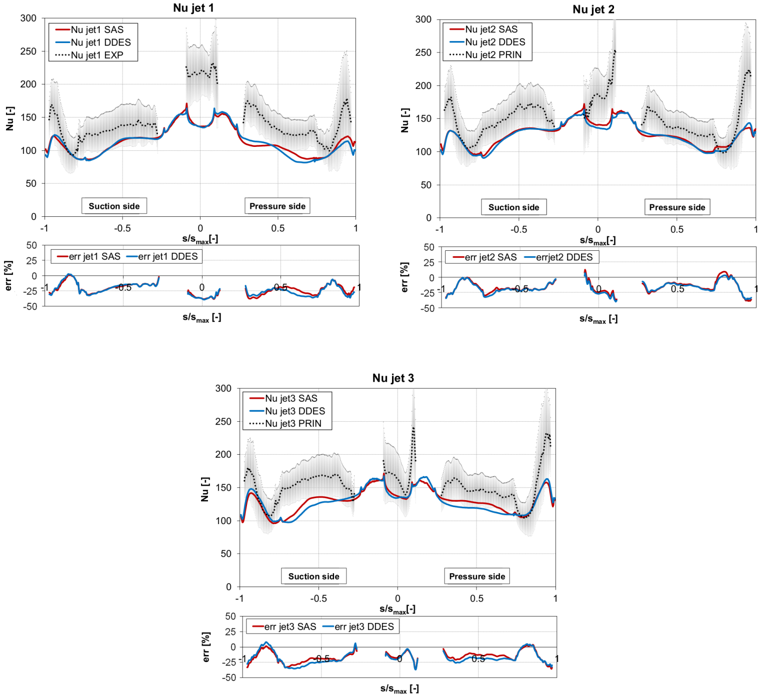

Figure 4.22: Circumferential Nu trends and error for the first (a), second (b) and third (c) impingement module. The uncertainty for the experimental data is also depicted.

By comparing the two numerical simulations, it can be observed that the predicted Nu trends are very similar to each other, with only slight discrepancies on the pressure side of the first jet and on the lateral surfaces for the third jet. This quantitative analysis also reveals that both SAS and DDES underpredict the experimental data, for all the three impingement modules. The error, defined by equation 4.4, is an almost constant value of around -20% on the lateral flat surfaces ($0.2 < \left|s/s_{max}\right| < 0.75$), while nonuniform values can be observed near the film cooling holes ($\left|s/s_{max}\right| > 0.75$) and on the central curved surface ($\left|s/s_{max}\right| < 0.2$). However, a comparison in the latter areas is not totally reliable, given the high noise of experimental data and the difficult modeling of these regions for the post processing. Nevertheless, it must be noticed that the discrepancy between the computed and measured values is comparable with the experimental uncertainty ($\simeq 20\%$). Moreover, as happened for the RANS simulations, the evidenced discrepancy could be related also to a difference in boundary conditions (fluid temperature and wall heat flux) than to an effective deficiency of the numerical or experimental data. This supposition is strengthened also by the fact that both SAS and DDES accurately reproduce the heat exchange pattern. This can be clearly observed if each Nu map of figure 4.21 is scaled with respect to the area averaged Nusselt value Nu_{avg}. The obtained distributions are represented in figure 4.23.

The analysis of the scaled maps reveals that the position and shape of the high Nu zones are correctly predicted by the simulations, as well as their relative entity. Even the shape and entity of the low heat exchange areas correspond, with only a small underestimation near the lower FC hole of each impingement module ($\left|s/s_{max}\right| \simeq 0.7$ and $y/P_y = 0.25$, $y/P_y = 1.25$, $y/P_y = 2.25$). The three maps show that the peak Nu values are stronger on the pressure side with respect to the suction side, and that high heat exchange area is wider. This indicates that the jet undergoes a stronger impact on such area, since it is less influenced by the mass flow extraction (FC PS holes mass flow rate is 1/4 of the FC SS one). However, the extraction holes mass flow rate only seems to slightly influence the relative Nu values around the holes themselves: all the maps show similar values in the areas defined by $-1 < \left|s/s_{max}\right| < -0.75$

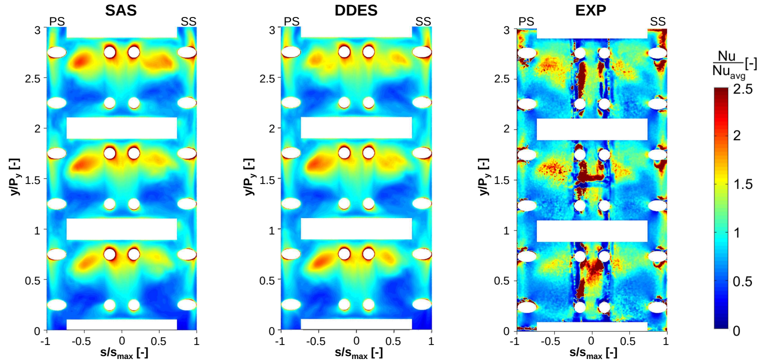

Figure 4.23: SAS (a), DDES (b) and experimental (c) Nu/Nu_{avg} distributions, for the test with $Re_j = 30000$, $CR = 70\%$ and non uniform extraction.

and $0.75 < \left|s/s_{max}\right| < 1$. In particular, the relative values are extremely similar for both the computed distributions, while for the experimental one a slight imbalance between pressure and suction side is present, with higher values on the latter. The noise of the experimental data does not allow to set a direct comparison between the maps on the central leading edge region: however, if the noiseless zones are considered, a reasonable agreement can be hinted also for such area. As already noticed for the RANS simulations, SAS and DDES tend to overestimate the surface Nu gradients: this could be due both to an underestimation of the jet lateral diffusion in the numerical results [129], and to an overestimation of the lateral conduction in the post processing of the experimental data.

If the distribution maps of figure 4.23 are observed in closer detail, the experimental results seem to be more accurately predicted by the DDES simulation: the shape of the relative Nu peaks of the third jet is more closely reproduced ($y/P_y \simeq 2.7$), and a better accuracy is evidenced even in the low heat exchange zones. This can be attributed to the greater number of resolved scales evidenced by the M criterion (figure 3.5), which allows a more accurate resolution of the flow field. The difference is however very small, and both the approaches suitably reproduce the scaled heat exchange pattern.

Looking at the Nu distribution asymmetries, as already anticipated in paragraph 4.1.4, both the simulations seem to confirm the reduced effect of the coolant extraction conditions on the shape of the heat exchange pattern: in fact, the differences between suction and pressure side distributions are small. The reduced entity of the asymmetry does not allow to identify whether or not it is correctly quantified by the simulations: to overcome this issue, the relative difference between suction and pressure side has been evaluated by defining a scalar K_{CFD}:

$$K_{CFD} = \frac{Nu(s,y) - Nu(-s,y)}{Nu_{avg}} \cdot 100\% \tag{4.5}$$

where Nu_{avg} is the Nusselt area averaged value. In fact, since the geometry is symmetric, $Nu(s,y)$ and $Nu(-s,y)$ are the Nusselt values in corresponding positions of the suction and pressure side respectively. The K_{CFD} definition implies its value to be positive where the suction side heat transfer performances overtake the pressure side ones and to be negative where the contrary happens. Given the "offset" asymmetry present in the experimental data, a different scalar K_{EXP} had to be defined:

$$K_{EXP} = \frac{[Nu(s,y)_s - Nu(s,y)_{ns}] - [Nu(-s,y)_s - Nu(-s,y)_{ns}]}{Nu_{avg}} \cdot 100\% \tag{4.6}$$

where Nu_s are the Nusselt values from the test with extraction flow split and Nu_{ns} are the ones for a test without split. Using the obvious hypothesis that a symmetric Nu distribution is obtained from CFD with symmetric flow conditions, the definitions 4.5 and 4.6 are equivalent, thus $K_{CFD} = K_{EXP} = K$. By evaluating K from both the experimental and numerical data, the distributions of figure 4.24 are obtained (given the symmetry of K distribution, only half of the map is depicted). Apart from the leading edge region ($|s/s_{max}| < 0.2$, the figure shows a reasonable agreement between the three distributions. Both SAS and DDES accu-

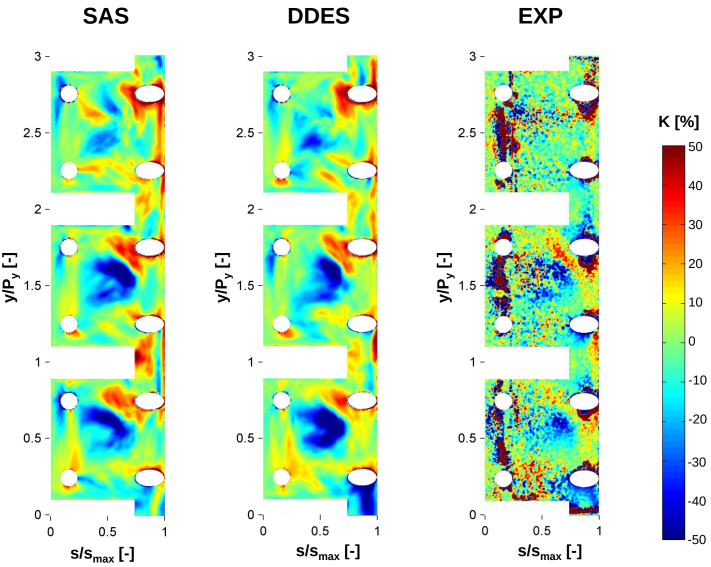

Figure 4.24: K distribution for SAS, DDES and experimental results.

rately reply the zones where the suction side Nu values are higher (near the film cooling holes) or lower (at the center of the flat surface) than the pressure side ones. However, both the experiment and the computations show that the imbalances between suction and pressure side are mainly in terms of distribution shape, and that the effect of suction and pressure side is thus negligible in terms of Nu average values.

As a concluding remark, it can be stated that both SAS and DDES underpredict the local Nu values in a sensible way. However, given the different boundary conditions with respect to the experimental test, the quite high experimental uncertainty and the accurate reproduction of the heat exchange distribution shape, it can be stated that both the models are reliable approaches for a cold bridge impingement system simulation. Despite this, the DDES is more advisable for a series of reasons:

- the accuracy in heat transfer pattern reproduction is slightly better;
- the accurate mesh crafting operation, required by the DDES to achieve LES-quality grid in the interesting regions, is not overly time-consuming, because the zone where the turbulence resolution is required is known and corresponds to the impingement cavity;
- the DDES is slightly faster than the SAS for the present case, as revealed by a cpu-time analysis.

Given such considerations, in the following the DDES result will be used as the reference case to interpret the experimental data, and it will be exploited to perform the further numerical simulations in rotating conditions.

Chapter 5

Effect of rotation on heat transfer distribution

This chapter reports the results achieved in terms of rotational effects on the leading edge heat transfer distribution. Exploiting the same structure of the previous chapter, the experimental findings are firstly presented, followed by the description of CFD results. A further validation of DDES model is reported; moreover, computational results help to deepen the comprehension of physical phenomenon that arise into the present cold bridge model, explaining the impact of rotation on the Nu distribution.

5.1 Experimental Results

In order to make more clear the dissertation concerning the experimental results, instead of the complete huge test-matrix, just the results of some cases, representative of all the configurations tested, are shown in this chapter. Results are presented again in terms of 2D Nusselt number distributions on the leading edge internal surface and PIV velocity plots on the two planes showed in section 2.7.

First of all, in order to assess the effectiveness of the LE impingement cooling system geometry in rotating condition, the Nusselt number value averaged on the whole surface (Nu_{ave}), can be observed for all the working conditions. figure 5.1a shows the Nu_{ave} evolution for all the test points.

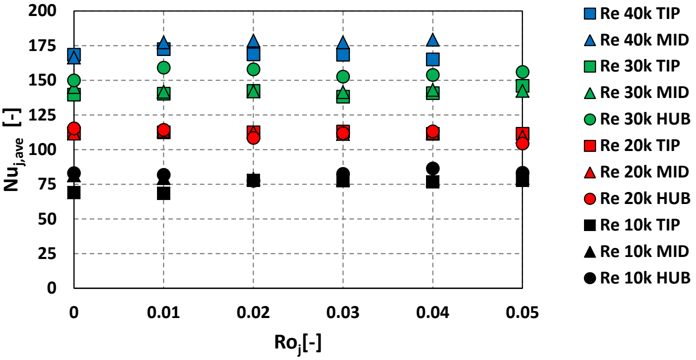

(a) Effect of rotation on Nu_{ave} for all the test points

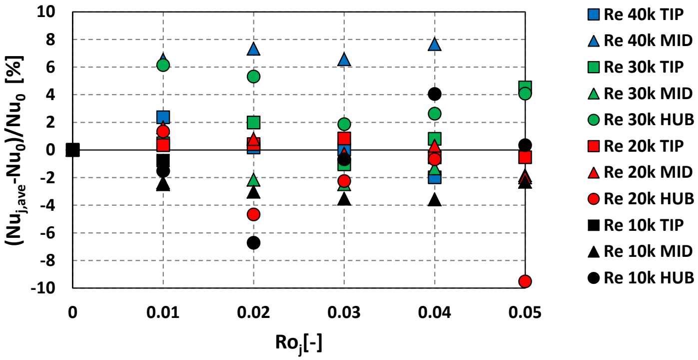

(b) Nu_{ave} percentage variation for all the test points

Figure 5.1: Average Nu variation with Ro_j

Again, it is possible to notice that it increases with Re_j and the negligible effect of CR on the average heat transfer coefficient for all the test points. Rotation seems to have little effect for this particular geometry, as is better underlined in figure 5.1b: the percentage variation

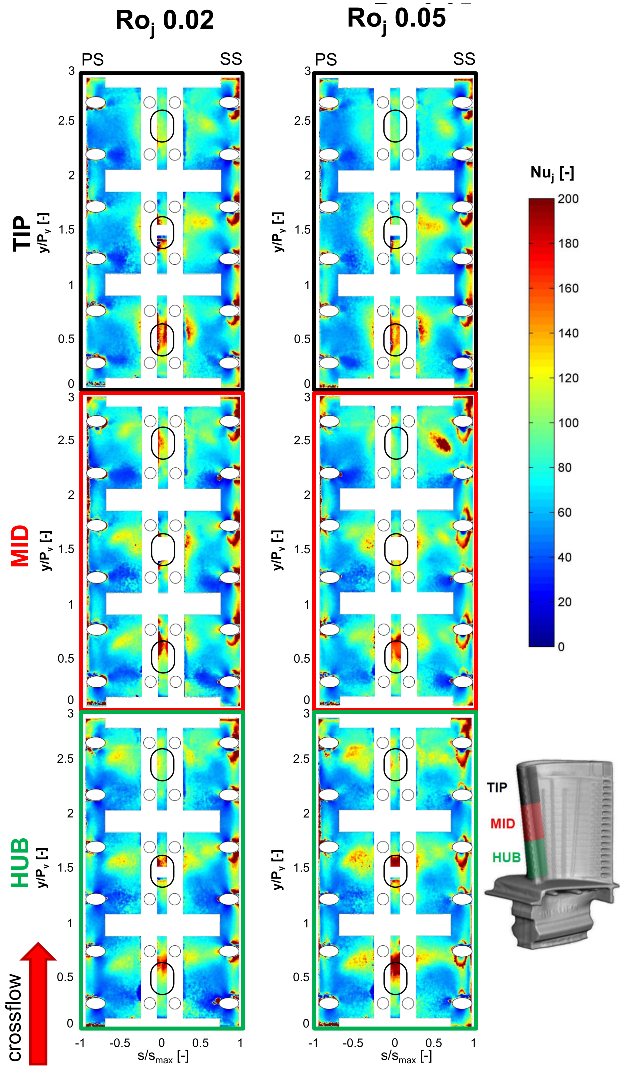

Figure 5.2: 2D Nu distributions at $Re_j = 10000$, $Ro_j = 0.02$ *and* $Re_j = 10000$, $Ro_j = 0.05$

with respect to the static cases Nu_0 for every Ro_j is comprised between ±8%, and a clear trend with Ro_j cannot be identified. In order to better understand the reason of this fact, it can be useful to to consider the Nu maps of figure 5.2, tests at $Ro_j = 0.02$ and $Ro_j = 0.05$ and at $Re_j = 10000$ are compared for each CR condition.These results clearly show that the rotation does not significantly affect Nusselt distribution, even if going from the HUB to the TIP the jets seem to be bent towards the SS. Nu maps also show that rotational effects are more and more pronounced as the cross-flow mass flow rate decreases. Tests performed in HUB conditions (CR= 70%) seem to be almost insensitive to rotational effects, while tests performed in TIP configuration (CR= 10%) show a noticeable migration of high Nu zones towards the suction sides. figure 5.3 clearly highlight such jet migration at the blade TIP, showing all the Ro_j conditions tested. The effect of increase of rotational speed on the Nu distribution is not negligible for low CR conditions, as the high heat transfer region is almost completely moved on the suction side flat plate. Moreover, it could be noticed that the effect of Ro_j is stronger passing from 0 up to 0.02 or, in other words, when the rotation is starting; on the other hand, it becomes almost negligible for higher velocity (Ro_j between 0.03 and 0.05).

In order to get more information about this phenomenon the PS and SS Nusselt distributions were separately averaged and their differences evaluated for every Ro_j condition. The results of this analysis are reported in figure 5.4. The differences between PS and SS follow the same trend for similar CR conditions: the HUB is almost insensitive to the rotation, in the MID the differences increase monotonically and the TIP the differences quickly reach a maximum value at $Ro_j = 0.03$ and then start to decrease. Since the Nu under an impinging jet is a function of various parameters, such as the jet velocity and the nozzle-to-target surface variation, the maximum in the trend can be interpreted as consequence of a combination in such parameters which maximize the rotational effects.

In order to deepen the comprehension of the physical phenomena, the analysis of the internal flow field that lead to the detected Nu distribution

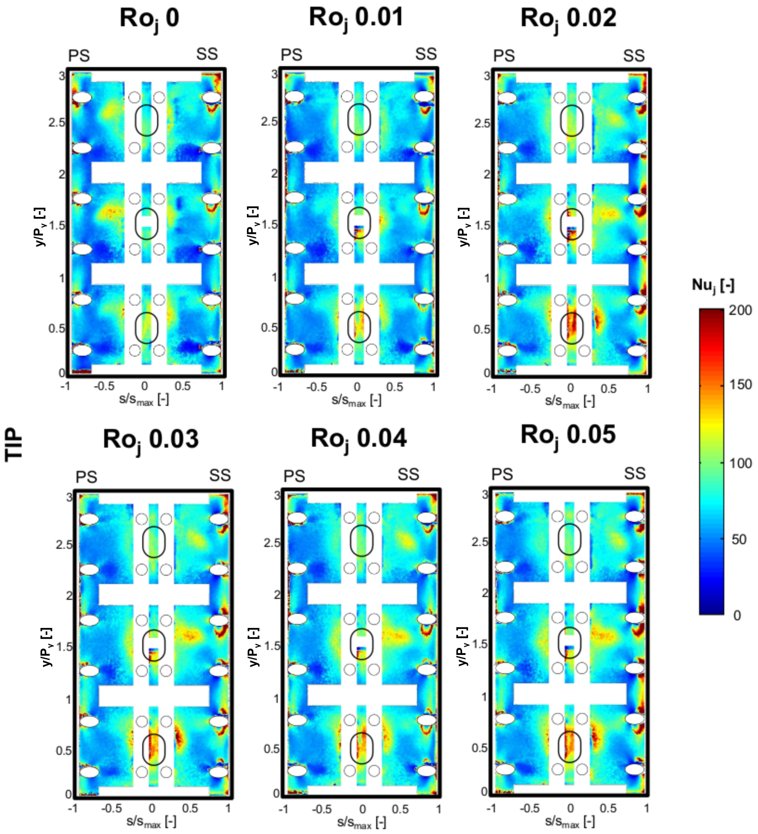

Figure 5.3: 2D Nu distributions at $Re_j = 10000$ *and* $Ro_j = 0 \div 0.05$ *for the TIP condition*

has been carried out. PIV measurements (performed by Furlani et al. [99] at the University of Udine) help to understand what happens inside the LE. figure 5.5 shows the internal velocity (scaled with respect to the jet bulk velocity defined by the equation 4.2) of the three CR configurations for $Re_j = 30000$ and $Ro_j = 0.05$. Again, HUB and MID seem to be scarcely affected by the rotation (compared with heat transfer maps obtained in static presented in section 4.10), while the jet on TIP is

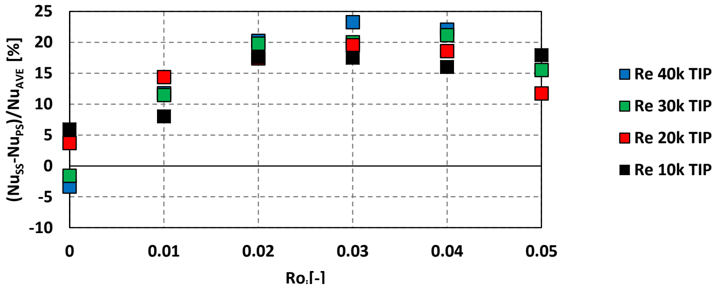

(a) TIP (CR=10%)

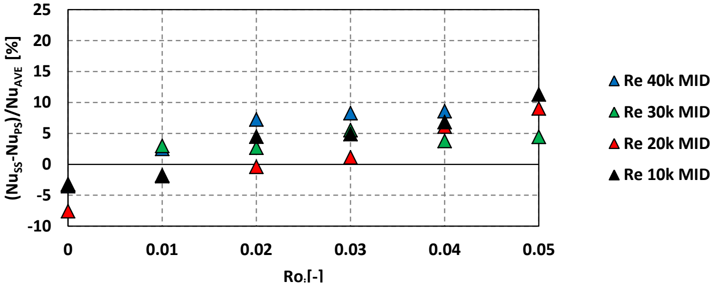

(b) MID (CR=40%)

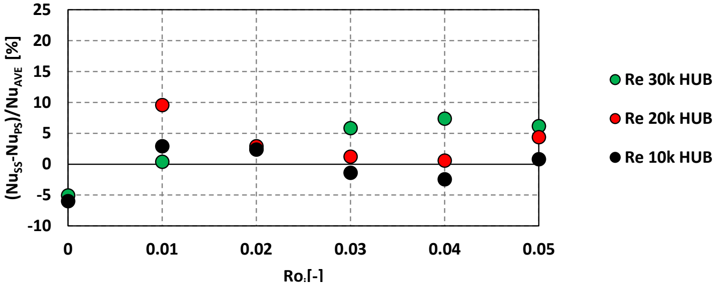

(c) HUB (CR=70%)

Figure 5.4: Nu differences between SS and PS at different Ro_j and cross-flow conditions

completely rotated towards the SS (see YZ plane), explaining the higher increase of Nu on that side. The bending of the jet helps also to explain the recorded insensitivity of the overall cooling performances to rotation,

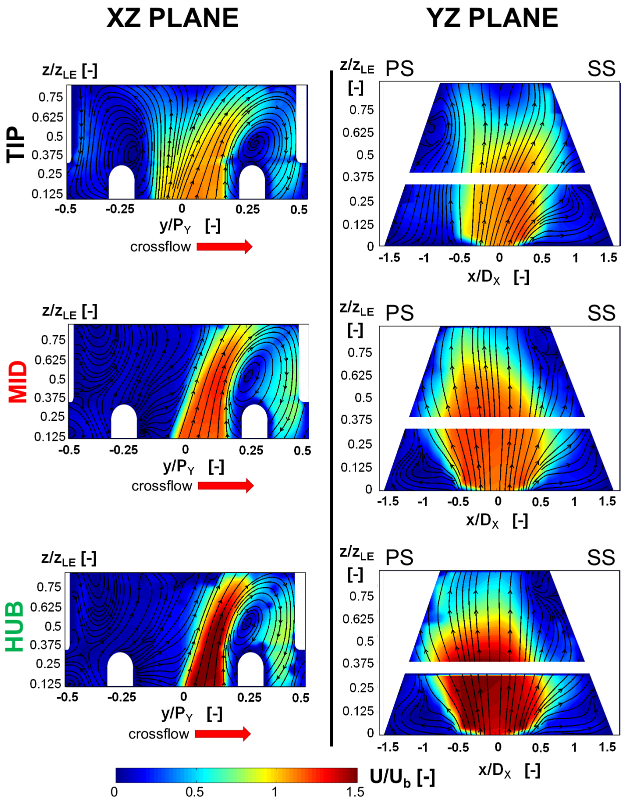

Figure 5.5: PIV velocity maps in rotating conditions for a whole blade configuration at $Re_j = 30000$ and $Ro_j = 0.05$

presented in figure 5.1a, which is in contrast with the open literature results [130, 131, 132, 133, 134, 135, 136]. In fact, given the target surface curvature and the impingement holes location, nozzle-to-target surface distance is similar for a wide region of the target area itself. As a consequence, even if rotation causes the jet to bend, nozzle-to-target surface distance not necessarily increases in this case; moreover, the angle between the jet direction and the target surface normal is not drastically altered by a jet inclination (i.e. the jet deflection is not increased). Thus, the jet momentum component perpendicular to the solid surface is only slightly altered by the rotation, and heat transfer is almost unaffected by the impact location. Another significant contribution to the heat transfer insensitivity to rotation is given by the ribs, which prevent the formation of a rotation induced cross-flow in the impingement cavity and confine the single jets into a limited region.

Considering the direction of rotation and the main velocity component of the jet, Coriolis forces should not affect the jet itself; thus another explanation for the bending of the jet should exist. Indeed, the flow velocity in the feeding channel is perpendicular to rotation axis and is thus subject to the generation of a total pressure gradient, positive on the PS, which cause a jet inclination on the opposite side. This evidence is confirmed by CFD analysis, and will be deepen in section 5.2.

5.2 Numerical Results

This section is devoted to the description of the main results achieved during the numerical simulations of rotating tests. The attention is focused at first to the further validation of the computational model comparing its results with the experiments. Once verified the capabilities of the CFD approach in predicting flow split and heat transfer distributions the numerical results are exploited to deepen the comprehension of experimental findings.

The comparison of measured (on the left side of the imagine) and predicted (on the right side of the imagine) flow field on the transversal plane XZ is reported in figure 5.6 in terms of normalized velocity. All these images are referred to the tests with a Re_j value of 10000. First of all, the results obtained in static condition and a cross flow mass flow rate representatives of HUB configuration ($CR = 70\%$) are shown; then, such comparison is reported also for rotating test ($Ro = 0.05$) for both HUB and TIP ($CR = 10\%$) configurations. Starting from static condition ($Ro_j = 0$), it is possible to observe that an overall agreement is achieved, at least for $x/P_x > -0.25\ mm$. The high-velocity jet and

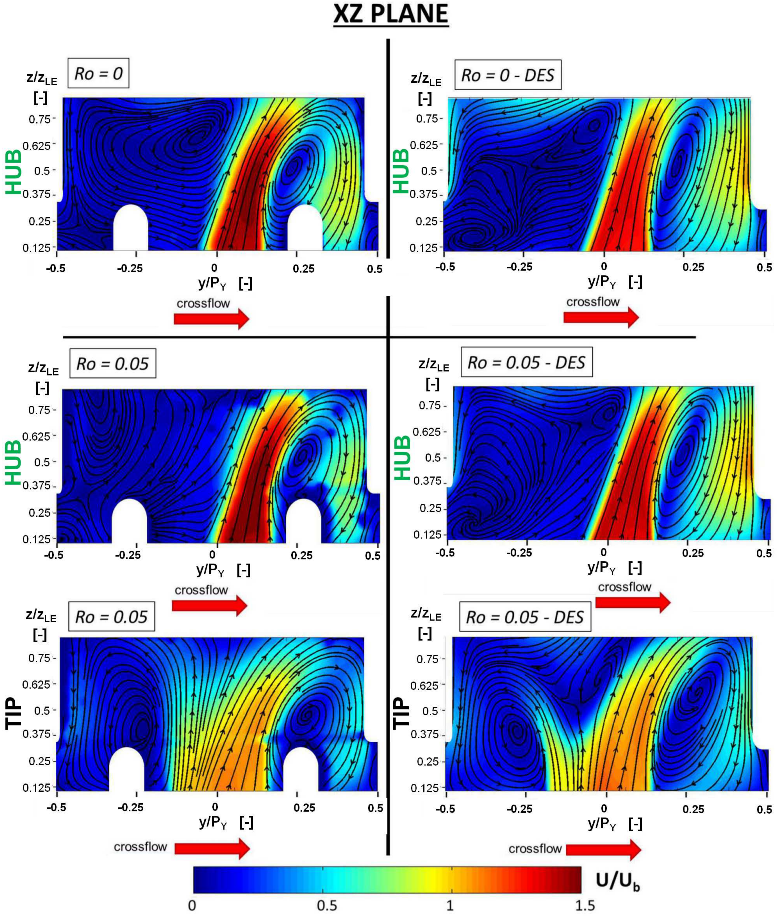

Figure 5.6: PIV (left) and CFD (right) velocity maps on plane XZ in static and rotating conditions for both HUB and TIP blade configuration at $Re_j = 30000$

the two recirculating flow structures generated by impingement on the wall are correctly reproduced from a qualitative point of view. Some discrepancies instead occur in the left part of the investigated region, where a single vortex is observed in the measured data and two distinct vortices are present in the calculated flow field. As clearly shown in the picture by the comparison of experimental measurements achieved in HUB configurations, rotation does not alter significantly the characteristics of the impingement jet (reasonably due to the high momentum), whereas it leads to a shift in the center of the recirculating vortex. CFD on the contrary does show an extremely slight sensitivity, with a flow field roughly unchanged. Moving to the tip of the blade, the same considerations made for the hub seem still valid: the right part of the cavity is well captured by simulation, even if the streamlines are too much diverted towards the left fin, reducing the extension of the recirculating region.

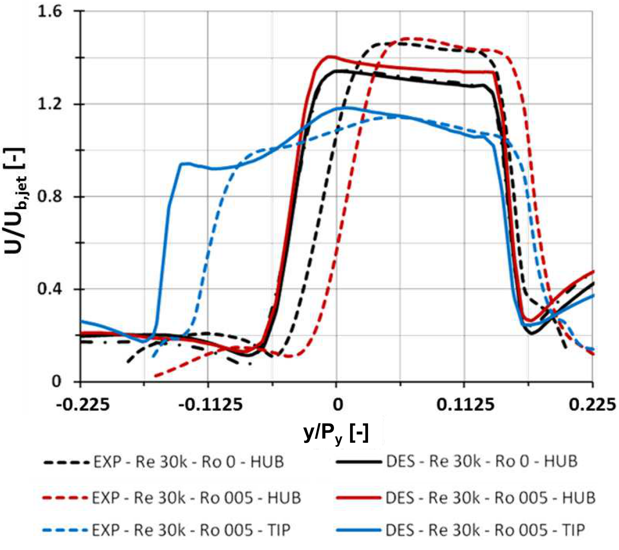

Figure 5.7: PIV and CFD velocity profiles on plane XZ ($z/Z_{LE} = 0.09$) *in static and rotating conditions for both HUB and TIP blade configuration at* $Re_j = 30000$

With the aim of better understanding the quantitative agreement with experimental measurements and highlighting the discrepancies between experiments and CFD, it is possible to refer to figure 5.7, where the velocity profiles extracted at $z/Z_{LE} = 0.09$ are reported (exploiting the same normalization of figure 5.6). Compared to PIV, CFD reasonably reproduces the flow field; nevertheless the impingement jet seems characterized by a lower velocity peak both in static and rotating conditions and the profile is generally stretched and moved towards the left side. As it is possible to observe, for the hub configuration, the rotation produces a shift to the right (the crossflow direction), as detected experimentally, whereas numerically an increase in the velocity peak without a shift along the radial direction is returned. At the tip the increased spread of the jet is confirmed.

To give a clearer representation of the flow field (figure 5.8), the comparison was extended to the additional cross-planes YZ. Following an analogous procedure to the one exploited for the plane XZ, velocity profiles at $z/Z_{LE} = 0.18$ (figure 5.9) were extracted.

These planes allow to show the three-dimensional features of the flow field within the impingement cavity, as well as the influence given by rotation. As shown in figures 5.8 and 5.9 (and as already observed in section 5.1), under static conditions the flow structures show significant spreading from the axis of the hole and a symmetry with respect to the $y/D_y = 0\ mm$ plane. Once rotation is provided the jets appear to be bent towards the suction side, especially when in the TIP configuration. CFD seems to accurately reproduce the streamline trajectories and a satisfactory agreement is achieved, especially concerning the flow field behavior varying both Ro and CR. Therefore, despite some discrepancies observed in the velocity magnitude, it is reasonable to assert that the DDES model is capable to reproduce the flow physics with a fairly good agreement also for the rotating test case.

As already mentioned in section 5.1, thanks to the CFD results the jet bending observed in figure 5.8 for the tip case can be justified by considering the flow behavior into the feeding channel. The interaction between the radial crossflow and rotation generates a strong Coriolis force on the coolant, which leads to a non-uniform total pressure and velocity

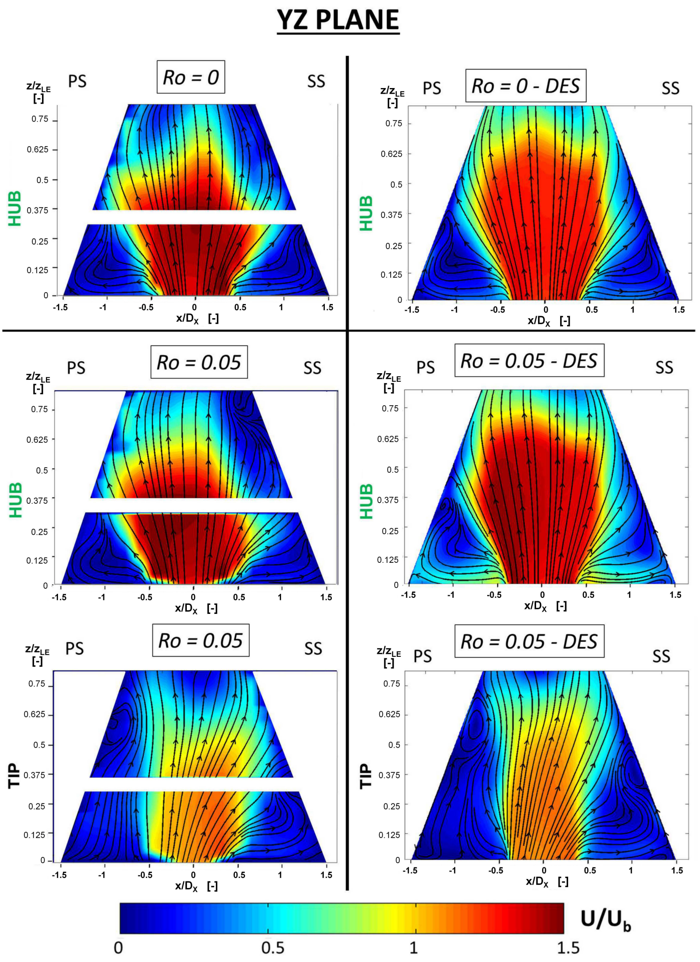

Figure 5.8: PIV (left) and CFD (right) velocity maps on plane YZ in static and rotating conditions for both HUB and TIP blade configuration at $Re_j = 30000$

distribution in the channel. In particular, the flow is driven towards the pressure side, which causes a higher total pressure distribution in such

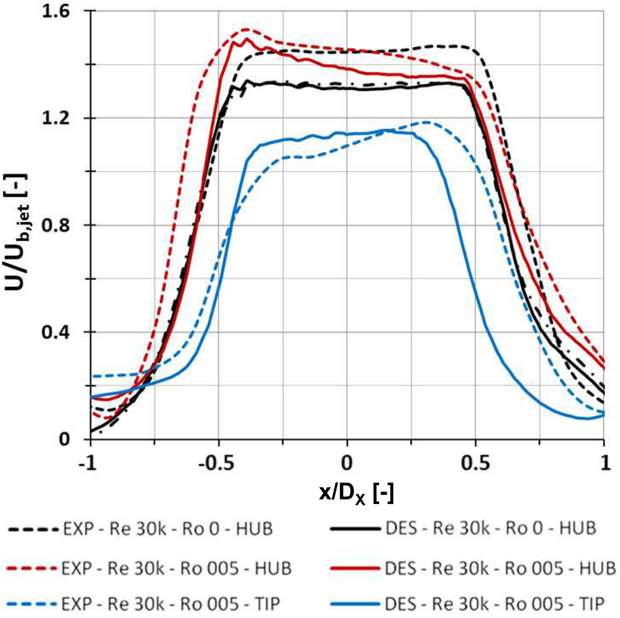

Figure 5.9: PIV and CFD velocity profiles on plane YZ (at $z/Z_{LE} = 0.18$) in static and rotating conditions for both HUB and TIP blade configuration at $Re_j = 30000$

region, as reported in figure 5.10. As a consequence, the jets are fed

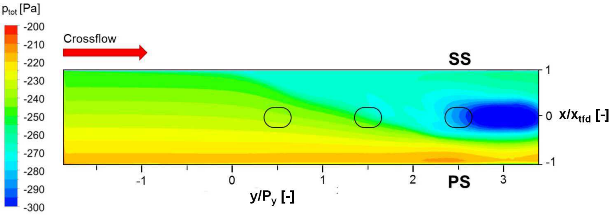

Figure 5.10: Total pressure distribution on a cross sectional plane ($Z = 0$ mm) of the feeding channel (DDES simulation, tip configuration)

by an uneven pressure distribution in the tangential direction, and tend to bend in the direction opposite to the higher pressure, i.e. towards the pressure side. This fact can also explain the increased sensitivity to rotation for tests with lower cross-flow mass flow rates at a given Ro_j value. In fact, Ro_j is defined with respect to the impingement holes velocity and hydraulic diameter, without considering the feeding channel flow. If a Rotation number is defined with respect to the feeding duct ($Ro_{CR} = \Omega \cdot D_{h,CR}/U_{b,CR}$, where $D_{h,CR}$ is the duct hydraulic diameter), it can be noticed that , if the cross-flow mass flow rate decreases at a given Ro_j value, so does its bulk velocity $U_{b,CR}$, and Ro_{CR} value increases. As a consequence, it can be supposed that rotational effects on the feeding channel increase as cross-flow mass flow rate decreases. Since it has been demonstrated cross-flow to have a significant influence on the impingement jet generation, it is evident that stronger rotational effects on the feeding channel imply stronger effects on the impingement jet too, i.e. a more pronounced bending.

Heat transfer represents always a more challenging benchmark with respect to pure aerodynamics, since it tends to emphasize even the small discrepancies in the velocity field and is characterized by a significant sensitivity to the turbulence properties of the flow. A first qualitative comparison, provided in figure 5.11, shows the main features of the heat transfer distribution within the impingement cavity.

As already reported in chapter 4, the DDES model is a suitable model for the simulation of such kind of internal cooling system. Indeed, it is able to catches the formation of the two lobes in the region characterized by the impingement of the jets to the lateral wall, as well as the significant contribution to local heat transfer augmentation ascribable to extraction holes, which regenerate the boundary layer through mass bleeding (see Byerley [137] for an extensive investigation on this topic). Concerning the effects of rotation, it is able to replicate the Nu peaks displacement due to the over mentioned bending of impingement jets both in HUB and TIP configurations. Since it was able to correctly detect the effects of rotational speed on the impingement jet bending, a correct assessment

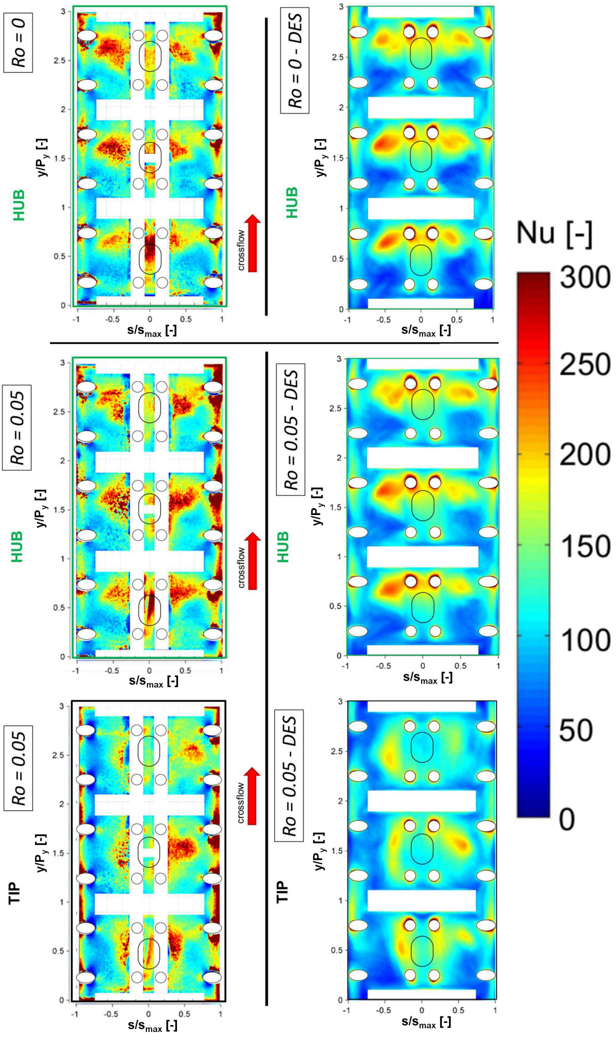

Figure 5.11: EXP and CFD LE Nusselt 2D maps in static and rotating conditions for both HUB and TIP blade configuration at $Re_j = 30000$

of heat transfer distribution was expected. A satisfactory agreement is highlighted in figure 5.11, as the computational model correctly reproduce the radial position of the peaks: at the hub the lobes are always located over the impingement hole, whereas moving to the tip the stagnation regions are aligned due to the above mentioned flow field development.

A quantitative comparison is provided in figure 5.12, where experimental and numerical results were line-averaged to obtain profiles along circumferential (y) and radial (x) directions. The profiles averaged in the radial direction and resolved in the lateral direction (figure 5.12(a)) show a general agreement between experimental measurements and CFD. The main discrepancies arise when the regions characterized by the Nu peaks are considered ($-0.75 < y/y_{max} < -0.25$ and $0.25 < y/y_{max} < 0.75$). It is worth stressing that the results are significantly smoothed during the averaging process, nevertheless an overall and persistent underestimation indeed occurs, especially in the regions characterized by low heat transfer rate, as already highlighted in figure 5.11. To better understand the extent of such underestimation, it is possible to refer to figure 5.12(b), where the profiles averaged in the lateral direction and resolved in the radial direction are reported. From this comparison it becomes evident that CFD is capable of predicting the experimental trend, despite the above mentioned general underestimation. It should be pointed out that the disagreement is rather variable and ranges between $10 - 20\%$ for the peaks and $15 - 40\%$ for the recirculating regions. In light of these considerations the CFD approach by means of hybrid RANS-LES models can be considered a valuable tool to provide a deeper understand of the flow physics as well a reasonable prediction of the Nusselt number distribution.

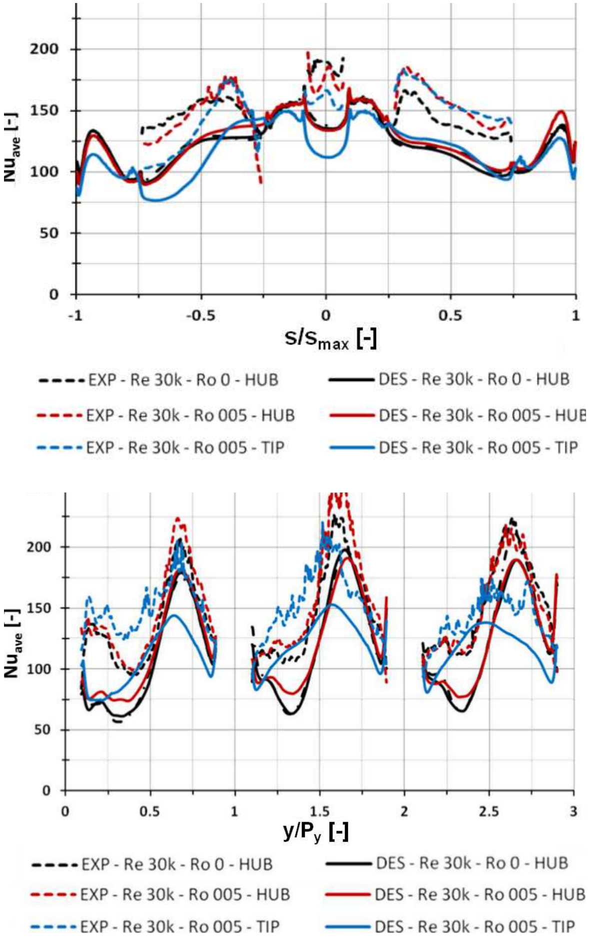

Figure 5.12: Circumferential (a) and radial (b) EXP and CFD LE Nusselt 2D profiles in static and rotating conditions for both HUB and TIP blade configuration at $Re_j = 30000$

Conclusions

The present study was performed within the PRIN 2010-2011 INSIDE project, whose aim was the experimental and numerical investigation of flow field and heat exchange in the internal cooling system of the leading edge of a high pressure gas turbine blade. In particular, the objective of this work is the determination of the heat transfer performances of a cold bridge type impingement system, considering the effects of coolant extraction through film cooling and showerhead holes. Essentially, such research activity is mainly focused at assessing the effect of rotation on the heat transfer coefficient distribution on the internal target surface of the LE. The geometry of the model, representing the inner region of a cooled blade leading edge, is composed by a trapezoidal radial feeding channel which supply coolant for the impingement cavity. Three jets are generated through three racetrack-shaped holes made on the impingement plate, which divides the two regions, and the corresponding impact zones are isolated by means of four large fins, thus defining three separated impingement modules.

An extensive experimental survey has been performed on such model. Test conditions have involved the variation of Rotation number, jet Reynolds number, crossflow conditions and mass flow extraction distribution. In particular, four Re_j values have been investigated, ranging from 10 000 up to 40 000 in order to meet engine representative flow field conditions, as well as for Ro which has been varied from 0.00 up to 0.05. The imposition of various crossflow conditions allowed to study the cooling system along the whole span of the blade: feeding channel outflow has thus been set as 70%, 40% and 10% of the total coolant inflow. Uniform and non uniform extraction conditions allowed to simulate the effect of external pressure distribution on the internal cooling system. Four rows of extraction holes are present: in the uniform extraction case each one draws 25% of the total cooling flow; on the other hand, in the non uniform configuration the 10% of the flow is extracted from the film cooling pressure side row, the 40% of it from the film cooling suction side row, while the remaining 50% is extracted by the 2 central rows of shower head. Measurements have been carried out on an enlarged scale model (SF 30.1:1) of the actual geometry both of the flow-field and of the heat transfer distribution through PIV and TLC thermography techniques respectively. Two parallel extensive experimental campaigns have been performed: the former at the University of Udine, which collaborated with the University of Florence within the PRIN 2010-2011 INSIDE project (PIV measurements at the Department of Electrical, Management and Mechanical Engineering), and the latter at the University of Florence (TLC measurements at the Industrial Engineering Department).

Moreover, a detailed CFD analysis of the model has also been performed. A benchmark of both steady and unsteady computational models has been carried out with the objective to evaluate their suitability at studying the physical phenomena involved into the impingement cooling system. Numerical results were also aimed to support the experimental results and to increase the comprehension of the involved fluid and thermal phenomena. While, the static uniform extraction cases have been simulated by using a steady RANS approach, both static and rotating non-uniform extraction simulations have been performed exploiting an unsteady hybrid RANS-LES models. In fact, RANS approach has revealed not to be suitable for the simulation of non uniform extraction cases, given the inability to reach a converged solution without a symmetric condition applied to the LE model. The $Re_j = 30\,000$, 70% crossflow case in static conditions has been exploited to benchmark two hybrid RANS-LES models: SAS and Delayed DES. Then, give the high computational costs, D-DES has been used to perform numerical simulations on a reduced test matrix in rotating configurations.

Both experimental and numerical results obtained in static tests showed that three distinct Nu peaks are present for each impingement module: two on the flat lateral surfaces are attributable to the jet spreading and interacting with the solid walls, while the last on the central curved zone is due to jet impingement and showerhead extraction. The lateral peaks often show a double lobe shape. The effect of a Re_j increase is an uniform heat exchange enhancement over the whole surface, while a decrease in the crossflow mass flow rate only alters the Nu distribution shape and not its entity; this latter fact has been attributed to different inclination of the jet. In fact, as confirmed by CFD analysis, the jet is not perfectly tangentially driven by impingement holes, but it is bent towards the crossflow direction and its bending increase with the crossflow mass flow rate due to the higher inertial forces. The results also show small differences of the non uniform extraction case with respect to the uniform one, with only a reduced heat exchange enhancement on the pressure side and a shift of the impingement location for the suction side. RANS simulations, performed in static conditions and uniform configurations, achieved a fairly good agreement with measurements. Despite a slight uniform underestimation of the experimental Nu area averaged values of about $-15\% \div -20\%$, a satisfactory replication in terms of heat exchange pattern has been reached, allowing for a deeper interpretation of experimental data through the computed flow field. It has also been found that the simulations suitably predict the effects of the Re_j variation and the consequences of a different crossflow rate even if with a certain overestimation of these latter.

Despite that even the two hybrid RANS-LES models, carried out in static conditions and non-uniform configurations, present a slight underestimation of the measured heat transfer rate, an accurate replication of the heat exchange pattern shape is performed by these models. In particular, an in-depth interpretation of Nu distribution through the simulated flow field shows that the heat exchange peaks are caused by the impact of large eddies, which are generated and entrained by the impingement jets. SAS and DDES models are substantially equivalent for the present case, even if the second seems preferable given its slightly better performances in terms of both heat exchange distribution accuracy and computational speed. Moreover delayed DES approach is considered more suitable for such kind of flow field instabilities; thus, the latter has been used to perform the numerical investigation in rotating conditions. The computational cost of unsteady scale resolving models is, however, at least one order of magnitude higher than steady RANS; moreover, the accuracy improvement over RANS is almost negligible for the present case. As a consequence, RANS approach would be preferable for the study of cold bridge impingement cooling, since it provides fair accuracy at a reasonable computational cost. Despite that, scale resolving models are needed when, as in the present investigation in rotating conditions, flow instabilities are high enough not to allow a RANS approach to provide a converged solution.

Concerning the rotational effects, both numerical and experimental results highlighted that rotation does not significantly alter area averaged Nu values; its effect is mainly verified as a shifting of heat transfer peaks towards the suction side of the leading edge. This fact is due to a bending of the jet in this direction, caused by an uneven rotation-induced total pressure distribution in the feeding channel. Indeed, as supposed during the experimental campaign and then confirmed by the CFD investigation, the stronger rotational effect affects the feeding channel: the Coriolis force acts on the coolant mass flow along the trapezoidal duct, leading to an increase of the total pressure on the pressure side of the internal channel. Such uneven pressure distribution causes the bending of the jet towards the suction side of the leading edge, affecting the leading edge HTC distribution as suggested before. Such rotational effects on the flow field are almost negligible in the hub region of the blade (CR = 70%) but become relevant on the tip, where the jets appear to be strongly bent towards the suction side. This is because the Coriolis force remarkably affects the trapezoidal duct pressure distributions for small cross flow mass flow rates, when the inertial forces are lower; instead, for higher

CR, when the inertial forces of the the coolant in the feeding channel are higher, the impact of the rotation is minor.

Also in rotating condition the agreement between experiments and computation is satisfactory. The impingement jet bending towards the feeding flow (crossflow) direction is well replicated by CFD, as the large recirculating zone along the fin with only a slight overestimation of jet spreading with respect to experiments. Less satisfactory agreement is achieved in the low velocity regions, where there is a stronger underestimation of the heat transfer distribution. Nevertheless, a reasonable reproduction of the experimental Nusselt number pattern is achieved by the simulations, and the highlighted underestimation of Nu values is coherent with the measurement uncertainty.

In conclusion, it is possible to state that the objectives of the present research activity have been achieved. An accurate and detailed experimental and numerical investigations of a realistic model of an internal cooling system of the leading edge of a high pressure gas turbine blade have been carried out. A novel rotating test-rig has been exploited allowing to achieve extremely detailed experimental results in terms of both flow field visualization and internal heat transfer coefficient distribution. The effects of rotation on the "cold bridge" model effectiveness have been assessed such as the effects of several others characteristic parameters. Besides such experimental campaign, a numerical investigation has been performed, allowing to benchmark and validate (both steady-state and unsteady) several computational models in static and rotating conditions of the model. Such validation has been carried out exploiting a perfect knowledge of the experiments set up and a level of detail of experimental measurements (against which compare numerical results) that has not precedent in literature. The computational approaches defined during the present work could be exploited in the future, to study the leading edge internal cooling system of a real rotating gas turbine blade, or to assess the performances of new configuration of impingement cooling: e.g. at evaluating the effect of different geometrical configuration (e.g. the impingement holes shape, the impingement plate/target surface distance or the configuration of the film cooling and shower head extraction holes).

Bibliography

[1] Meece, C. E. "Gas turbine technologies for the future." 12^{th} *Symposium on Air-Breathing Engines*, Vol. 1, 1995.

[2] Ballal, D. R. and Zelina, J. "Progress in aeroengine technology (1939-2003)." *Journal of Aircraft*, 41:43–50, 2004.

[3] Rolls-Royce plc. *The Jet Engine.* Fifth edition, 1996.

[4] Han, J. C. and Huh, M. "Recent studies in turbine blade internal cooling." *Heat Transfer Research*, 41:803–828, 2010.

[5] Ostanek, K. J. "Improving pin-fin heat transfer predictions using artificial neural network." *ASME Journal of Turbomachinery*, 136: 1–9, 2014.

[6] Gupta, S, Chaube, A., and Verma, P. "Review on heat transfer augmentation techniques: Application in gas turbine blade internal cooling." *Journal of Engineering Science and Technology, Review article*, 05:52–57, 2012.

[7] Viskanta, R. "Heat transfer to impinging isothermal gas and flame jets." *Experimental Thermal and Fluid Science, 6*, pages 111–134.

[8] N. Zuckerman, N. Lior. "Jet impingement heat transfer: Physics, correlations, and numerical modeling." *Advances in Heat Transfer Volume 39*, pages 565–631.

[9] Brown, S. E. “21st century hot engines.” *Popular Science*, pages 83–89, 1990.

[10] Winchler, L. *Design tools and innovative concepts for gas turbine cooling applications*. Phd thesis, University of Florence, 2015.

[11] S.C. Cheah, D.C. Jackson H. Ji B.E. Launder H. Iacovides. “Lda investigation of the flow development through rotating u-ducts.” *ASME Journal of Turbomachinery, Vol. 118, No. 3*, pages 590–595.

[12] J.C. han, K. Kalkuehler Y.M. Zhang. “Uneven wall temperature effect on local heat transfer in a rotating two-pass square channel with smooth walls.” *ASME Journal of Heat Transfer, Vol. 114, No. 4*, pages 850–858.

[13] Denga, H., Gua, Z., Zhub, J., and Tao, Z. “Experiments on impingement heat transfer with film extraction flow on the leading edge of rotating blades.” *International Journal of Heat and Mass Transfer*, 55:5425–5435, 2012.

[14] E.Y. Jung, D.H. Lee J.S. Park S. Park H.H. Cho C.U. Park. “Effect of rotation on heat transfer of a concave surface with array impingement jet.” *Proceedings of ASME Turbo Expo 2013: Turbine Technical Conference and Exposition (GT2013), San Antonio, Texas, USA, June 3-7*, 2013.

[15] Menter, F.R. *Best Practice: Scale-Resolving Simulations in ANSYS CFD, version 1.02*. ANSYS Germany GmbH, 2012.

[16] DeLuca, D. P. and Annis, C. “Fatigue in single crystal nickel superalloys.” *Office of Naval Research*, FR21999-23, 1994.

[17] Arakere, N. J. “High-temperature fatigue properties of single crystal superalloys in air and hydrogen.” *ASME Paper*, 2001-GT-0585, 2001.

[18] Naik, R. A., DeLuca, D. P., and Shah, D. M. “Critical plane fatigue modeling and characterization of single crystal nickel superalloys.”

ASME Journal of Engineering for Gas Turbines and Power, 126: 391–400, 2004.

[19] Maclachlan, D. W. and Knowles, D. M. “The effect of material on the analysis of single crystal turbine blades: Part I - Material Model.” *Fatigue and Fracture Engineering Material Science*, 25: 385–398, 2002.

[20] Maclachlan, D. W. and Knowles, D. M. “The effect of material on the analysis of single crystal turbine blades: Part II - Component Analysis.” *Fatigue and Fracture Engineering Material Science*, 25: 399–409, 2002.

[21] D. Metzger, P. Kuenstler D. Takeuchi. “Effectiveness and heat transfer with full-coverage film cooling.” *ASME Journal of Engineering for Power*, 95: 180–184, 1973.

[22] D. Kercher, W. Tabakoff. “Heat transfer by a square array of round air jets impinging perpendicular to flat surface including the effect of spent air.” *ASME Journal of Engineering for Power*, 92: 73–82, 1970.

[23] Martin, H. “Heat and mass transfer between impinging gas jets and solid surfaces.” *Advances in Heat Transfer*, 13:1–60, 1977.

[24] Behbahani, A. and Goldstein, R. “Local heat transfer to staggered arrays of impinging circular air jets.” *ASME J Eng Gas Turb Power*, 105:354–360, 1983.

[25] L. Florschuetz, D. Metzger C. Truman. “Streamwise flow and heat transfer distributions for jet array impingement with crossflow.” *ASME Journal of Heat Transfer*, 103: 337–342, 1981.

[26] Florschuetz, L., Metzger, D., Su, C., Isoda, Y., and Tseng, H. “Heat transfer characteristics for jet arrays impingement with initial crossflow.” *ASME, Journal of Heat Transfer*, 106:34–41, 1984.

[27] B.R. Hollworth, L. Dagan. “Arrays of impingement jetswith spent fluid removal through vent holes on the target surface. part i: Average heat transfer.” *Journal of Engineering for Power*, 102: 994–999, 1980.

[28] S.V. Ekkad, J.C. Han Y. Huang. “Impingement heat transfer on a target plate with film holes.” *AIAA Journal of Thermophysics and Heat Transfer*, 13(4): 522–528, 1999.

[29] Chupp, R., Helms, H., McFadden, P., and Brown, T. “Evaluation of internal heat transfer coefficients for impingement cooled turbine blades.” *Journal of Aircraft*, 6:203–208, 1969.

[30] D.E., Metzger, T.T., Yamashita, and C.W., Jenkins. “Impingement cooling of concave surfaces with lines of circular air jets.” *ASME J Eng Gas Turb Power*, 91(3):149–155, 1969.

[31] Metzger, D.E., Takeuchi, D.I., and Kuenstler, P.A. “Effectiveness and heat transfer with full-coverage film cooling.” *ASME J Eng Gas Turb Power*, 95(3):180–184, 1973.

[32] Hrycak, P. “Heat transfer from a row of impinging jets to concave cylindrical surfaces.” *International Journal of Heat and Mass Transfer*, 24:407–419, 1981.

[33] D. Metzger, R. Bunker. “Local heat transfer in internally cooled turbine airfoil leading edge regions: Part i - impingement cooling without film coolant extraction.” *Journal of Turbomachinery*, 112: 451–458, 1990.

[34] D. Metzger, R. Bunker. “Local heat transfer in internally cooled turbine airfoil leading edge regions: Part ii - impingement cooling with film coolant extraction.” *Journal of Turbomachinery*, 112: 459–466, 1990.

[35] Polat, S., Mujmdar, A.S., and Douglas, W.J.M. “Heat transfer distribution under a turbulent impinging jet - a numerical study.” *Drying Technology, Vol.3, No.1*, pages 15–38.

[36] Frost, S.A. and Jambunathan, K. "Numerical prediction of semi-confined jet impingement and comparison with experimental data." *International Journal for Numerical Methods in Fluids, 23*, pages 295–306.

[37] Coussirat, M., Beeck, J. Van, Mestres, M., Egusquiza, E., Buchlin, J.M., and Valero, C. "Computational fluid dynamics modeling of impinging gas-jet systems: II. application to an industrial cooling system device." *ASME Journal of Fluids Engineering, 127*, pages 704–713.

[38] Morris, G.K., Garimella, S.V., and Fitzgerald, J.A. "Flow-field prediction in submerged and confined jet impingement using the reynolds stress model." *ASME Journal of Electronic Packaging, 121*, pages 255–262.

[39] Souris, N., Liakos, H., and Founti, M. "Impinging jet cooling on concave surfaces." *AIChE Journal, 50(8)*, pages 1672–1683.

[40] B. V. N. Rama Kumar, B. V. S. S. S. Prasad. "Computational flow and heat transfer of a row of circular jets impinging on a concave surface." *Heat Mass Transfer, 44*, pages 667–678, 2008.

[41] M. Ashok Kumar, B. V. S. S. S. Prasad. "Computational investigations of flow and heat transfer on an effused concave surface with a single row of impinging jets for different exit configurations." *Engineering Applications of Computational Fluid Mechanics, 3:4*, pages 530–542.

[42] M. E. Taslim, S. D. Spring Y. Pan. "An experimental study of impingement on roughened airfoil leading-edge walls with film holes." *Journal of Turbomachinery*, 123: 766–773, 2001.

[43] Taslim, M., Bakhtari, K., and Liu, H. "Experimental and numerical investigation of impingement on a rib-roughened leading-edge wall." *ASME, Turbo Expo 2003*, GT2003-38118, 2003.

[44] Taslim, M. and Bethka, D. “Experimental and numerical impingement heat transfer in an airfoil leading-edge cooling channel with crossflow.” *ASME, Turbo Expo 2007*, GT2007-28212, 2007.

[45] Elebiary, K. and Taslim, M. “Experimental/numerical crossover jet impingement in an airfoil leading-edge cooling channel.” *ASME, Turbo Expo 2011*, GT2011-46004, 2011.

[46] F. Maiuolo, L. Tarchi N. Ohlendorf B. Facchini. “Experimental investigation on the heat transfer in a turbine airfoil leading edge region: Effects of the wedge angle and jet impingement geometries.” *10th European Turbomachinery Conference, (ETC130-2013)*, 2013.

[47] F. Maiuolo, L. Tarchi N. Ohlendorf B. Facchini. “Experimental investigation on the heat transfer of a leading edge cooling system: Effects of jet-to-jet spacing and showerhead extraction.” *ASME paper, (GT2013-94759)*, 2013.

[48] A.H. Epstein, J.J. Koo U.Z. Preiser J.L. Kerrebrock. “Rotating effects on impingement cooling.” *GTL Report No. 184, MIT*, 1985.

[49] Ch. Mattern, D.K. Hennecke. “The influence of rotation on impingement cooling.” *ASME Paper (96-GT-161)*, 1996.

[50] H. Iacovides, D. Kounadis. “Experimental study of the flow and thermal development of a row of cooling jets impinging on a rotating concave surface.” *Journal of Turbomachinery, 127*, pages 222–229.

[51] Craft, T.J., Iacovides, H., and Mostafa, N.A. “Modelling of three-dimensional jet array impingement and heat transfer on a concave surface.” *International Journal of Heat and Fluid Flow*, 29:687–702, 2008.

[52] Craft, T.J., Iacovides, H., and Mostafa, N.A. “Numerical modelling of flow and heat transfer from an array of jets impinging onto a concave surface under stationary and rotating conditions.” *ASME, Turbo Expo 2008*, GT2008-50624:2435–2444, 2008.

[53] S.K. Hong, H.H. Cho D.H. Lee. "Heat/mass transfer measurement on concave surface in rotating jet impingement." *Journal of Mechanical Science and Technology, 22 (10)*, pages 1952–1958.

[54] Cho, H.H., Hong, S.K., and Lee, D.H. "Effect of jet direction on heat/mass transfer of rotating impingement jet." *Applied Thermal Engineering*, 29(14-15):2914–2920, 2009.

[55] Cho, H.H., Hong, S.K., and Lee, D.H. "Heat/mass transfer in rotating impingement/effusion cooling with rib turbulators." *International Journal of Heat and Mass Transfer*, 52(13-14):2914–2920, 2009.

[56] Andrei, L., Carcasci, C., Da Soghe, R., Facchini, B., Maiuolo, F., Tarchi, L., and Zecchi, S. "Heat transfer measurements in a leading edge geometry with racetrack holes and film cooling extraction." *ASME J Turbomach*, 135(3).

[57] Maiuolo, F. *Experimental Analysis of Gas Turbine Airfoil Leading Edge Cooling Systems.* Phd thesis, University of Florence, 2012.

[58] Cocchi, L. Impingement cooling investigation on a novel rotating test rig. Bachelor thesis, University of Florence, 2014.

[59] Han, J. C., Dutta, S., and Ekkad, S. *Gas Turbine Heat Transfer and Cooling Technology.* Taylor & Francis, 2000.

[60] VanFossen, J. G. "Heat-transfer coefficients for staggered arrays of short pin fins." *ASME Journal of Engineering and Power*, 104: 268–274, 1982.

[61] Metzger, D., Shepard, W., and Haley, S. "Row resolved heat transfer variations in pin-fin arrays including effects of non-uniform arrays and flow convergence." *ASME Paper*, 86-GT-132, 1986.

[62] Faulkner, E. F. *Analytical Investigation of Chord Size and Cooling Methods on Turbine Blade Cooling Requirements.* NASA CR-120883, 1971.

[63] Armstrong, J. and Winstanley, D. “Review of staggered array pin fin heat transfer for turbine cooling applications.” *ASME Journal of Turbomachinery*, 110:94–103, 1988.

[64] Ligrani, P. “Heat transfer augmentation technologies for internal cooling of turbine components of gas turbine engines.” *International Journal of Rotating Machinery, Review article*, ID 275653, 2013.

[65] Ligrani, P., Oliveira, M. M., and Blaskovich, T. “Comparison of heat transfer augmentation techniques.” *AIAA Journal*, 41(3):337–362, 2003.

[66] Han, J. C., Dutta, S., and Ekkad, S. *Gas Turbine Heat Transfer and Cooling Technology.* Taylor & Francis, first edition, 2000.

[67] Surace, M. *Investigation of impingement systems for gas turbine combustor cooling.* Phd thesis, University of Florence, University of Florence, 2004.

[68] Carmine, E. Di. Studio numerico del raffreddamento per impingement nelle turbomacchine: simulazione di geometrie reali. Master thesis, University of Florence, 2004.

[69] Bogard, D. *The Gas Turbine Handbook - Airfoil Film Cooling.* NETL.

[70] Bonini, A. *A Decoupled Conjugate Heat Transfer Procedure Involving Flow Network Approach: application to GT blade cooling.* PhD thesis, Università degli Studi di Firenze, Dipartimento di Energetica Sergio Stecco, 2011.

[71] Bunker, R. S. “A review of shaped hole turbine film-cooling technology.” *ASME Journal of Heat Transfer*, 127:441–453, 2005.

[72] 7-7-7 shaped hole description, 2015. URL `http://www.mne.psu.edu/psuturbine/PublicShapedHole.html`.

[73] L'Ecuyer, M. R. and Soechting, F. O. "A model for correlating flat plate film-cooling effectiveness for rows of round holes." *AGARD Paper*, CP-390, 1985.

[74] Baldauf, S., Scheurlen, M., Schulz, A., and Wittig, S. "Correlation of film-cooling effectiveness from thermographic measurements at enginelike conditions." *ASME Journal of Turbomachinery*, 124: 686–698, 2002.

[75] Goldstein, R. J. "Film cooling." *Advances in Heat Transfer*, 7: 321–379, 1971.

[76] Colban, W. F., Thole, K. A., and Bogard, D. "A film-cooling correlation for shaped holes on a flat-plate surface." *ASME Journal of Turbomachinery*, 133(1):011002/01–011002/11, 2011.

[77] Seller, J. P. "Gaseous film cooling with multiple injection stations." *AIAA Journal*, 1:2154–2156, 1963.

[78] Harrington, M., McWaters, M., Lemmon, C. A., and Thole, K. A. "Full-coverage film cooling with short normal injection holes." *ASME Journal of Turbomachinery*, (123):798–805, 2001.

[79] Ceccherini, A., Facchini, B., Tarchi, L., and Toni, L. "Combined effect of slot injection, effusion array and dilution hole on the cooling performance of a real combustor liner." *ASME Paper*, GT2009-60047, 2009.

[80] Kirollos, B. and Povey, T. "An energy-based method for predicting the additive effect of multiple film cooling rows." *ASME Paper*, GT2013-94934, 2013.

[81] Sweeney, P. C. and Rhodes, J. F. "An infrared technique for evaluating turbine airfoil cooling designs." *Journal of Turbomachinery*, 122:171–177, 2000.

[82] Bunker, R. S. "Gas turbine heat transfer: 10 remaining hot gas path challenges." *ASME Paper*, GT2006-90002, 2006.

[83] Annerfeldt, M. O., Persson, J. L., and Torisson, T. “Experimental investigation of impingement cooling with turbulators or surface enlarging elements.” *ASME Paper*, 2001-GT-0149, 2001.

[84] Liu, Y., Song, S., and Lo, Y. “Jet impingement heat transfer on target surfaces with longitudinal and transverse grooves.” *International Journal of Heat and Mass Transfer*, 58:292–299, 2013.

[85] Mhetras, S., Han, J. C., and Huth, M. “Impingement heat transfer from jet arrays on turbulated target walls at large reynolds numbers.” *Journal of Thermal Science and Engineering Applications*, 6: 021003/1–021003/10, 2014.

[86] Kanokjaruvijit, K. and Martinez-Botas, R. F. “Heat transfer and pressure investigation of dimple impingement.” *ASME Paper*, GT2005-68823, 2005.

[87] Lutade, P. V., Khanwalkar, P. M., and Kore, S. S. “Heat transfer enhancement by jet impingement on dimpled surface with different cavities.” *International Journal of Engineering and Innovative Technology*, 4(5):152–155, 2014.

[88] Rao, Y., Wan, C., Xu, Y., and Zang, S. “Local heat transfer characteristics in channels with pin fin and pin fin-dimple arrays.” *ASME Paper*, GT2011-45449, 2011.

[89] Rao, Y., Wan, C., Xu, Y., and Zang, S. “An experimental and numerical study of flow and heat transfer in channels with pin fin-dimple combined arrays of different configurations.” *Journal of Heat Transfer*, 134(12):12190/1–12190/11, 2012.

[90] Simpson, T. W. “AM need MEs.” *ASME Mechanical Engineering*, 137:30–35, 2015.

[91] Snyder, J. C., Stimpson, C. K., Thole, K. A., and Mongillo, D. “Build direction effects on additively manufactured channels.” *ASME Paper*, GT2015-43935, 2015.

[92] Stimpson, C. K., Snyder, J. C., Thole, K. A., and Mongillo, D. "Roughness effects on flow and heat transfer for additively manufactured channels." *ASME Paper*, GT2015-43940, 2015.

[93] L. Bonanni, B. Facchini L. Tarchi C. Carcasci. "Experimental survey on heat transfer in a trailing edge cooling system: effects of rotation in internal cooling ducts." *ASME Paper (GT2012-69638)*, 2012.

[94] Comandi, F. Progettazione di un banco prova rotante per misure di scambio termico su leading edge di una pala di turbina a gas. Bachelor thesis, University of Florence, 2013.

[95] Sage, I. "Thermochromic liquid crystals." *Liquid Crystals*, 38: 1551–1561, 2011.

[96] Tarchi, L. Sviluppo di correlazioni per sistemi di raffreddamento per trailing edge di pale di turbina a gas. Master thesis, University of Florence, 2002.

[97] Incropera, F. P., DeWitt, D. P., Bergman, T., and Lavine, A. *Fundamentals of heat and mass transfer*. Wiley, sixth edition, 2006.

[98] T.L. Chan, K. Jambunathan S. Ashford-Frost. "Calibrating for viewing angle effect during heat transfer measurements on a curved surface." *Journal of Heat and Mass Transfer, 44*, pages 2209–2223.

[99] Furlani, L., Armellini, A., and Casarsa, L. Aerodynamic behaviour under rotation of an advanced leading edge impingement cooling channel. In *Proceedings of the 12th International Symposium on Experimental Computational Aerothermodynamics of Internal Flows*. 13—16 July 2015, Genova, Italy, .

[100] Willert, Christian. "Stereoscopic digital particle image velocimetry for application in wind tunnel flows." *Measurement science and technology*, 8(12):1465, 1997.

[101] Furlani, L, Armellini, A, and Casarsa, L. Buoyancy effects at high rotation number on the flow field inside a triangular shaped rib roughened channel. In *European Turbomachinery Conference*. Madrid, Spain, 23-27 March 2015, .

[102] Armellini, A, Mucignat, C, Casarsa, L, and Giannattasio, P. "Flow field investigations in rotating facilities by means of stationary piv systems." *Measurement Science and Technology*, 23(2):025302, 2012.

[103] ASME. "Measurement uncertainty in instrument and apparatus." *vol. ANSI/ASME PTC 19.1-1985 of Performance Test Code, ASME*, (19), 1985.

[104] Kline, S. J. and McClintock, F. A. "Describing uncertainties in single sample experiments." *Mechanical Engineering*, 75(1), 1953.

[105] Armellini, A, Casarsa, L, and Giannattasio, P. "Separated flow structures around a cylindrical obstacle in a narrow channel." *Experimental Thermal and Fluid Science*, 33(4):604–619, 2009.

[106] Cengel, Y. *Introduction to thermodynamics and heat transfer*. 1997.

[107] Wilks, Graham. "External natural convection about two-dimensional bodies with constant heat flux." *International Journal of Heat and Mass Transfer*, 15(2):351–354, 1972.

[108] H.K. Versteeg, W. Malalasekera. *An introduction to computational fluid dynamics - The finite volume method*. Longman Scientific & Technical, first edition, 1995.

[109] Mangani, L. *Development and validation of an Object Oriented CFD Solver for Heat Transfer and Combustion Modeling in Turbomachinery Applications*. Phd thesis, University of Florence, 2012.

[110] Fondelli, T. Analisi cfd di un sistema di combustione per motori aeronautici a basse emissioni inquinanti. Master thesis, University of Florence, 2012.

[111] Pope, S.B. *Turbulent Flows.* Cambridge University Press, UK, 2000.

[112] Menter, F.R. “Improved two-equation k-omega turbulence models for aerodynamic flows.” *AIAA-Journal, 32(8)*, pages 1598–1605.

[113] *ANSYS® CFX 14.0 Theory guide.* 2011.

[114] A. Andreini, L. Mazzei F. Turrini B. Facchini. “Impact of swirl flow on combustor liner heat transfer and cooling - a numerical investigation with hybrid rans-les models.” *ASME Paper (GT2015-42403)*, 2015.

[115] F. R. Menter, Y. Egorov. “A scale-adaptive simulation model using two-equation models.” *AIAA paper 2005-1095, Reno/NV*, 2005.

[116] F. R. Menter, Y. Egorov. “Development and application of sst-sas turbulence model in the desider project.” *Second Symposium on Hybrid RANS-LES Methods, Corfu, Greece*, 2007.

[117] F. R. Menter, Y. Egorov. “Re-visiting the turbulent scale equation.” *Proc. IUTAM Symposium; One hundred years of boundary layer research, Gattingen*, 2004.

[118] Davidson, L. “Evaluation of the sst-sas model: channel flow, asymmetric diffuser and axi-symmetric hill.” *European Conference on Computational Fluid Dynamics - ECCOMAS CFD*, 2006.

[119] A. Andreini, M. Insinna L. Mazzei S. Salvadori B. Facchini. “Numerical investigation of combustor-turbine interaction with hybrid rans-les models.” *ASME Paper (GT2015-42402)*, 2015.

[120] *ANSYS® CFX-Solver Modeling Guide.* 2011.

[121] P.R. Spalart, M. Strelets S.R. Allmaras W.-H. Jou. “Comments on the feasibility of les for wings, and on a hybrid rans/les approach.” *1st AFOSR Int. Conf. On DNS/LES, Aug.4-8, 1997, Ruston, LA. In Advances in DNS/LES, C. Liu & Z. Liu Eds., Greyden Press, Colombus, OH.*, .

[122] F. R. Menter, R. Langtry M. Kuntz. “Ten years of industrial experience with the sst turbulence model.” *Turbulence, Heat and Mass Transfer, 4*, 2003.

[123] P.R. Spalart, M.L. Shur K.D. Squires S.Deck. “A new version of detached-eddy simulation, resistant to ambiguous grid densities.” *Theoretical and Computational Fluid Dynamics, 20*, pages 181–195, .

[124] J. von Wolfersdorf, B. Weigand. “Internal cooling in turbomachinery, in *Turbine Blade Internal Cooling-Selected Experimental Approaches*, journal = Lecture Series 2010-05. von Karman Institute for Fluid Dynamics, year = 2010.”

[125] *ANSYS® CFX-Pre User Guide.* 2011.

[126] Pope, S.B. “Ten questions concerning the large-eddy simulation of turbulent flows.” *New Journal of Physics, 35*, 2004.

[127] Facchini, B., Burberi, E., Carcasci, C., Cocchi, L., Massini, D., Armellini, A., Casarsa, L., and Furlani, L. “Effect of rotation on a gas turbine blade internal cooling system: experimental investigation.” *Proceedings of ASME Turbo Expo*, (GT2016-57594), 2016.

[128] Burberi, E., Massini, D., Cocchi, L., Mazzei, L., Andreini, A., and Facchini, B. “Effect of rotation on a gas turbine blade internal cooling system: Numerical investigation.” *J. Turbomach*, 139(3): 031005, 2016. doi: 10.1115/1.4034799.

[129] L. Mangani, A. Andreini B. Facchini C. Bianchini. “Development and validation of a c++ object oriented cfd code for heat transfer analysis.” *ASME paper (AJ-1266)*, 2007.

[130] Iacovides, Hector, Kounadis, Diamantis, Launder, Brian E, Li, Jiankang, and Xu, Zeyuan. “Experimental study of the flow and thermal development of a row of cooling jets impinging on a rotating concave surface.” *Journal of turbomachinery*, 127(1):222–229, 2005.

[131] Craft, TJ, Iacovides, H, and Mostafa, NA. “Modelling of three-dimensional jet array impingement and heat transfer on a concave surface.” *International Journal of Heat and Fluid Flow*, 29(3): 687–702, 2008.

[132] Craft, Tim J, Iacovides, Hector, and Mostafa, Nor A. Numerical modelling of flow and heat transfer from an array of jets impinging onto a concave surface under stationary and rotating conditions. In *ASME Turbo Expo 2008: Power for Land, Sea, and Air*, pages 2435–2444. American Society of Mechanical Engineers, 2008.

[133] Hong, Sung Kook, Lee, Dong Hyun, and Cho, Hyung Hee. “Heat/-mass transfer measurement on concave surface in rotating jet impingement.” *Journal of mechanical science and technology*, 22(10): 1952–1958, 2008.

[134] Hong, Sung Kook, Lee, Dong Hyun, and Cho, Hyung Hee. “Effect of jet direction on heat/mass transfer of rotating impingement jet.” *Applied Thermal Engineering*, 29(14):2914–2920, 2009.

[135] Hong, Sung Kook, Lee, Dong Hyun, and Cho, Hyung Hee. “Heat/-mass transfer in rotating impingement/effusion cooling with rib turbulators.” *International Journal of Heat and Mass Transfer*, 52 (13):3109–3117, 2009.

[136] Deng, Hongwu, Gu, Zhenpeng, Zhu, Jianqin, and Tao, Zhi. “Experiments on impingement heat transfer with film extraction flow on the leading edge of rotating blades.” *International Journal of Heat and Mass Transfer*, 55(21):5425–5435, 2012.

[137] Byerley, A. R. *Heat trasnfer near the entrance to a film cooling hole in a gas turbine blade.* PhD thesis, University of Oxford, 1989.